

ANALYSIS OF SLOT COUPLED PATCH ANTENNAS  
USING CLOSED FORM GREEN'S FUNCTIONS

A THESIS SUBMITTED TO  
THE GRADUATE SCHOOL OF NATURAL AND APPLIED SCIENCES  
OF  
MIDDLE EAST TECHNICAL UNIVERSITY

BY

MESUT GÖKSU

IN PARTIAL FULFILLMENT OF THE REQUIREMENTS  
FOR  
THE DEGREE OF MASTER OF SCIENCE  
IN  
ELECTRICAL AND ELECTRONICS ENGINEERING

AUGUST 2009

Approval of the thesis:

**ANALYSIS OF SLOT COUPLED PATCH ANTENNAS USING CLOSED  
FORM GREEN'S FUNCTIONS**

submitted by **MESUT GÖKSU** in partial fulfillment of the requirements for the degree of **Master of Science in Electrical and Electronics Engineering Department, Middle East Technical University** by,

Prof. Dr. Canan Özgen \_\_\_\_\_  
Dean, Graduate School of **Natural and Applied Sciences**

Prof. Dr. İsmet Erkmen \_\_\_\_\_  
Head of Department, **Electrical and Electronics Engineering**

Prof. Dr. Gülbin Dural \_\_\_\_\_  
Supervisor, **Electrical and Electronics Engineering Dept., METU**

**Examining Committee Members:**

Prof. Dr. Gülbin Dural \_\_\_\_\_  
Electrical and Electronics Engineering Dept., METU

Prof. Dr. Nilgün Günalp \_\_\_\_\_  
Electrical and Electronics Engineering Dept., METU

Assoc. Prof. Dr. Özlem Aydın Çivi \_\_\_\_\_  
Electrical and Electronics Engineering Dept., METU

Assist. Prof. Dr. Lale Alatan \_\_\_\_\_  
Electrical and Electronics Engineering Dept., METU

M.Sc Tuncay Erdöl \_\_\_\_\_  
ASELSAN

**Date:** 28.08.2009

**I hereby declare that all information in this document has been obtained and presented in accordance with academic rules and ethical conduct. I also declare that, as required by these rules and conduct, I have fully cited and referenced all material and results that are not original to this work.**

Name, Last name : Mesut Göksu

Signature :

# ABSTRACT

## ANALYSIS OF SLOT COUPLED PATCH ANTENNAS USING CLOSED FORM GREEN'S FUNCTIONS

Göksu, Mesut

M.S., Department of Electrical and Electronics Engineering

Supervisor: Prof. Dr. Gülbin Dural

August 2009, 145 pages

In this thesis, an analysis technique for the slot coupled patch antennas using MoM in conjunction with the closed form Green's functions is presented. Slot coupled patch antennas are fed by a microstrip open stub which is coupled to the patch through an electrically small slot. Current distributions over the microstrip line, slot line and the patch are represented by rooftop basis functions. First, a relatively simple structure, microstrip coupled slot line is investigated using the proposed technique. Then the method is extended to the slot coupled patch antenna geometry. By using the method, current distributions on the feedline and the patch are calculated for a generic slot coupled patch antenna. Then by using the distributions, return scattering parameters of the antenna is approximated with complex exponentials using Prony's method. A parametric study is carried out to observe the effect of each antenna component on the antenna performance. Current distributions and return loss calculations are repeated for modified antennas to observe and demonstrate the performance differences. All simulations are verified using HFSS<sup>®</sup> software and the results available in the literature.

Keywords: Aperture Coupled Patch Antennas, Slot Coupled Patch Antennas, Method of Moments, Green's Functions, Microstrip Lines.

# ÖZ

## YARIK KUPLAJLI YAMA ANTENLERİN KAPALI FORMDA GREEN FONKSİYONLARI KULLANILARAK İNCELENMESİ

GÖKSU, Mesut

Yüksek Lisans, Elektrik ve Elektronik Mühendisliği Bölümü

Tez Yöneticisi: Prof. Dr. Gülbin DURAL

Ağustos 2009, 145 sayfa

Bu tez çalışmasında, kapalı formda Green fonksiyonları moment metoduyla birlikte kullanılarak yarık kuplajlı yama antenlerin incelenmesi için bir yöntem sunulmuştur. Yarık kuplajlı yama antenler açık uçlu mikroşeritler ile beslenmekte bunlar ise yama antene küçük bir yarık ile kuplajlanmaktadır. Mikroşerit hatlar, yarık ve yama üzerindeki akım dağılımı, çatı taban fonksiyonları ile ifade edilmiştir. İlk olarak, göreceli basit bir yapı olan yarık anten önerilen yöntemle incelenmiş, yöntem daha sonra, yarık kuplajlı yama antenler için uyarlanmıştır. Yöntem kullanılarak, genel bir yarık kuplajlı yama antenin mikroşerit hat ve yama üzerindeki akım dağılımları bulunup, daha sonra, bu akım dağılımları ile Prony yöntemi kullanılarak antenin saçılım parametreleri hesaplanmıştır. Parametrik bir çalışma yardımı ile değişik anten bileşenlerinin anten performansı üzerindeki etkileri incelenmiştir. Anten performansı üzerindeki değişiklikleri gözlemlemek ve gösterebilmek için akım dağılımı ve geri dönüş kaybı hesapları fiziksel olarak değiştirilmiş anten yapıları için tekrar edilmiştir. Tüm benzetim ve hesaplamalar HFSS<sup>®</sup> yazılımı kullanılarak ve literatürdeki benzer çalışmaların sonuçlarıyla doğrulanmıştır.

Anahtar Kelimeler: Yarık Kuplajlı Yama Antenler, Moment Metodu, Green Fonksiyonları, Mikroşerit Hatlar.

To Africa, for her beauty and virtue.

## ACKNOWLEDGMENTS

In the first place I would like to record my gratitude to Prof. Dr. Gülbin Dural for her supervision, advice, and guidance from the very early stage of this study. I am grateful to Prof. Dr. Lale Alatan and Tuncay Erdöl for their valuable advices in the last phase of this study.

I am grateful to Aselsan A.Ş, who has provided the support and equipment I have needed to complete my thesis and to Tubitak, who has funded two year of my studies.

My friends İsmail Serdar Dönmez, Hüseyin Gökhan Akçay, Sacit Yılmaz and Bülent Ay helped me whenever I stucked with their warm welcome.

It is a pleasure to thank Harry Kewell, Gandalf Greyhame, Merry Brandybuck, Peregrin Took, Cahit Zarifoğlu, Sezai Karakoç, Fred and George Weasley and Noir Desir who made this thesis easier.

It may not be enough to present thanks to Keziban Akkaya, for her endless and unique contributions

Last but not least, I am grateful in my very heart to my merciful mother, decent father, unique sister and supporting brother for being always with me throughout my life.

# TABLE OF CONTENTS

ABSTRACT .....	iv
ÖZ .....	v
ACKNOWLEDGMENTS.....	vii
TABLE OF CONTENTS.....	viii
LIST OF FIGURES .....	xi
LIST OF ABBREVIATIONS .....	ii
CHAPTERS	
1. INTRODUCTION .....	3
2. METHOD OF MOMENTS IN MULTILAYER STRUCTURES USING CLOSED FORM GREEN’S FUNCTIONS.....	9
2.1 Choice of the Basis and Testing Functions .....	13
2.1.1 Choice of the Basis Functions.....	13
2.1.1.1 Entire Domain Basis Functions .....	13
2.1.1.2 Sub-Domain Basis Functions .....	13
2.1.2 Choice of the Testing Functions.....	15
2.1.2.1 Point Matching or Collocation Method .....	15
2.1.2.2 Sub-sectional Collocation Method .....	16
2.1.2.3 Galerkin’s Method.....	17
2.1.2.4 Method of Least Squares.....	17
2.2 Analysis of Planar Printed Structures Using MoM.....	18
2.2.1 Green’s Function .....	18
2.2.2 Spatial Domain MoM Formulation .....	20
2.2.3 Spectral Domain MoM Formulation .....	26
2.3 Closed-form Green’s Functions .....	27
3. MoM ANALYSIS OF THE MICROSTRIP FED SLOT ANTENNA.....	35
3.1 Definition of the Structure.....	35
3.2 Formulation.....	37
3.2 Current Distribution Results.....	43

4. MoM ANALYSIS OF THE MICROSTRIPLINE FED-SLOT COUPLED PATCH ANTENNA.....	50
4.1 Definition of the Structure.....	50
4.2 Establishment of the Problem.....	52
4.3 Boundary Conditions.....	54
4.3.1 Feedline Boundary Conditions.....	55
4.3.2 Aperture Boundary Conditions.....	58
4.3.3 Patch Boundary Conditions.....	62
4.3.3.1 Y-directed Patch Surface Field Equations.....	62
4.3.3.2 X-directed Patch Surface Field Equations.....	64
4.4 Test and Basis Functions.....	65
4.5 MoM Matrices and the Number of Unknowns.....	66
4-6 Results.....	67
5. PARAMETRIC ANALYSIS OF THE MICROSTRIP FED-SLOT COUPLED PATCH ANTENNA.....	77
5.1 Analysis of a Base Structure.....	78
5.2 Analysis of Slot Length Effects to the Antenna Performance.....	84
5.2.1 Slot Length is 1.2 cm.....	84
5.2.2 Slot Length is 1 cm.....	88
5.3 Analysis of Stub Length Effects to the Antenna.....	94
5.3.1 Stub Length is 2 cm.....	94
5.3.2 Stub Length is 1.6 cm.....	99
5.3.3 Stub Length is 0.6 cm.....	103
5.3.4 Stub Length is 0.4 cm.....	108
6.CONCLUSION.....	114
6.1 Summary.....	114
6.2 Future Work.....	116
REFERENCES.....	117
APPENDICES	
A. CALCULATION OF THE CONVOLUTION INTEGRAL OVER BASIS AND TESTING FUNCTIONS.....	121

B. PRONY'S METHOD .....	140
C. SINGULARITY EXTRACTION .....	144

# LIST OF FIGURES

## FIGURES

Figure 1.1 Sideview and topview of a patch antenna slot coupled to a microstripline [1].....	4
Figure 2.1 Domain Representation of Entire Domain Basis Function .....	14
Figure 2.2 Domain Representation of Sub-Domain Basis Function .....	14
Figure 2.3 Dirac(Kronecker) Delta Function .....	16
Figure 2.4 Sub-Domains Weighting Function .....	16
Figure 2.5 The radiation of a source in a volume V [28].....	20
Figure 2.6 A General Microstrip Structure [10].....	21
Figure 2.7 A Typical Layered Medium with Embedded Sources in Layer-i .....	28
Figure 2.8 Definitions of the Sommerfeld Integration Path and Integration Path for One Level Approximation [40]. .....	30
Figure 2.9 The Paths and Used in Two-Level Approximation [40].....	31
Figure 3.1 General strip coupled slot antenna structure.....	36
Figure 3.2 Strip to slot structure (dimensions) .....	36
Figure 3.3 Strip coupled slot structure (sideview).....	38
Figure 3.4 Surface electric current distribution on the microstrip feed at 1.3 GHz. ..	43
Figure 3.5 Surface magnetic current distribution on the slotline at 1.3 GHz.....	45
Figure 3.6 Surface electric current distribution on the microstrip feed at 1.5 GHz. .	46
Figure 3.7 Surface electric current distribution on the microstrip feed at 2.5 GHz. .	47
Figure 3.8 Surface electric current distribution on the microstrip feed at 3.0 GHz. .	48
Figure 3.9 S11 characteristic of strip coupled slot antenna between 1.3-4.5GHz.....	49
Figure 4.1 Slot Coupled Patch Antenna.....	51
Figure 4.2 Slot Coupled Patch Antenna (side view).....	51
Figure 4.3 Schematic of Electric current on the feed and the antenna .....	53
Figure 4.4 General scheme of the boundary electrical and magnetic currents.....	54
Figure 4.5 Rooftop Basis and Testing Functions [3].....	66

Figure 4.6 Parametric geometry of the microstrip fed-slot coupled patch antenna....	68
Figure 4.7 Parametric geometry of the microstrip fed-slot coupled patch antenna(sideview).....	68
Figure 4.8 Electric current distribution along the feedline .....	70
Figure 4.9 Comparative demonstration of input impedance from MoM and Pozar's results .....	72
Figure 4.10 Y-directed electric current distribution along the patch y-direction at X=-0.75 cm.....	73
Figure 4.11 Y-directed electric current distribution along the patch y-direction at X=0 cm.....	73
Figure 4.12 Electric current distribution along the feedline at 2.5 GHz.....	74
Figure 4.13 Y-directed electric current distribution along the patch y-direction at X=-0.75 cm.....	75
Figure 4.14 Y-directed electric current distribution along the patch y-direction at X=0 cm.....	75
Figure 5.1 Parametric geometry of a microstrip fed-slot coupled patch antenna.....	78
Figure 5.2 Surface electric current distribution on the microstrip feedline at 2.17 GHz.....	79
Figure 5.3 Surface electric current distribution on the microstrip feedline at 2.16 GHz.....	80
Figure 5.4 Surface electric current distribution on the microstrip feedline at 2.18 GHz.....	80
Figure 5.5 Comparative demonstration of input impedance from MoM and Schaubert's results .....	82
Figure 5.6 Surface electric current distribution on the microstrip patch at 2.2 GHz at x=-0.75 cm .....	83
Figure 5.7 Surface electric current distribution on the microstrip patch at 2.2 GHz at x=0 cm.....	83
Figure 5.8 Surface electric current distribution on the microstrip feedline at 2.21 GHz.....	85

Figure 5.9 Surface electric current distribution on the microstrip feedline at 2.2 GHz. .....	86
Figure 5.10 Surface electric current distribution on the microstrip feedline at 2.22 GHz. .....	86
Figure 5.11 Comparative demonstration of input impedance from MoM and Schaubert's results .....	87
Figure 5.12 Surface electric current distribution on the microstrip patch at 2.21 GHz at $x=0$ cm. .....	88
Figure 5.14 Surface electric current distribution on the microstrip feedline at 2.25 GHz. .....	89
Figure 5.15 Surface electric current distribution on the microstrip feedline at 2.2 GHz. .....	90
Figure 5.16 Surface electric current distribution on the microstrip feedline at 2.3 GHz. .....	91
Figure 5.17 Comparative demonstration of input impedance from MoM and Schaubert's results[5]. .....	92
Figure 5.18 Surface electric current distribution on the microstrip patch at 2.25 GHz, $x=-1.5$ cm .....	93
Figure 5.19 Surface electric current distribution on the microstrip patch at 2.25 GHz, $x=0$ cm. .....	93
Figure 5.20 Surface electric current distribution on the microstrip feedline at 2.2 GHz. .....	95
Figure 5.21 Surface electric current distribution on the microstrip feedline at 2.175 GHz. .....	95
Figure 5.22 Surface electric current distribution on the microstrip feedline at 2.225 GHz. .....	96
Figure 5.23 Comparative demonstration of input impedance of MoM and Schaubert's results[5]. .....	97
Figure 5.24 Surface electric current distribution on the microstrip patch at 2.2 GHz, $x=0$ cm. .....	98

Figure 5.25 Surface electric current distribution on the microstrip patch at 2.2 GHz, x=0.75 cm.....	98
Figure 5.26 Surface electric current distribution on the microstrip feedline at 2.2 GHz. ....	100
Figure 5.27 Surface electric current distribution on the microstrip feedline at 2.175 GHz. ....	100
Figure 5.28 Surface electric current distribution on the microstrip feedline at 2.225 GHz. ....	101
Figure 5.29 Comparative demonstration of input impedance of MoM and Schaubert's results[5].....	102
Figure 5.30 Surface electric current distribution on the microstrip patch at 2.2 GHz, x=0 cm.....	103
Figure 5.31 Surface electric current distribution on the microstrip feedline at 2.2 GHz. ....	104
Figure 5.32 Surface electric current distribution on the microstrip feedline at 2.175 GHz. ....	105
Figure 5.33 Surface electric current distribution on the microstrip feedline at 2.225 GHz. ....	105
Figure 5.34 Comparative demonstration of input impedance of MoM and Schaubert's results[5].....	106
Figure 5.35 Surface electric current distribution on the microstrip patch at 2.2 GHz, x=0 cm.....	107
Figure 5.35 Surface electric current distribution on the microstrip patch at 2.2 GHz, x=0.75 cm.....	107
Figure 5.37 Surface electric current distribution on the microstrip feedline at 2.2 GHz. ....	109
Figure 5.38 Surface electric current distribution on the microstrip feedline at 2.175 GHz. ....	109
Figure 5.39 Surface electric current distribution on the microstrip feedline at 2.225 GHz. ....	110

Figure 5.40 Comparative demonstration of input impedance of MoM and Schaubert's results[5].....	111
Figure 5.40 Surface electric current distribution on the microstrip patch at 2.2 GHz, x=0 cm.....	112

## **LIST OF ABBREVIATIONS**

FDTD : Finite Difference Time Domain

FEM : Finite Element Method

MoM : Method of Moments

PEC : Perfect Electric Conductor

PMC : Perfect Magnetic Conductor

VSWR : Voltage Standing Wave Ratio

# CHAPTER 1

## INTRODUCTION

The rapid increase in the interest to the microstrip antenna technology began in the late 1970s. In the beginning of 1980s, basic microstrip antenna elements and arrays were almost as good as possible in the sense of design and modeling. Hence, scientists changed their attentions to improving antenna performance features (e.g., bandwidth)

Because of space and bandwidth problems, Pozar and his colleagues searched for a method which included the use of a variety of two or more layered substrates. One obvious possibility was to use two back-to-back substrates with feed through pins. This would allow plenty of surface area, and had the critical advantage of allowing the use of GaAs (or similar) material for one substrate, with a low dielectric constant for the antenna elements. However that would yield a problem of fabrication because of large number of via holes. Hence, Pozar and his friends looked for the possibility of using a two sided-substrate with printed slot antennas fed with microstrip lines [3]. However at this time bi-directionality of the antenna element was unacceptable. As a result they concluded with the solution by combining these two approaches by using aperture to couple the microstrip feed line to the resonant microstrip patch antenna. Most importantly, the required coupling aperture was small enough so that the back radiation from the coupling aperture was much smaller than the forward radiation level [2].

Microstrip fed-slot-coupled patch antenna structure has been introduced in 1985 [1]. Then, it attracted great deal of attention in variety of applications. Versatility and adaptability of the proposed design inspired many scientists all around the world to utilize it in several works. Broad bandwidth, independent material selection freedom

for radiating and feedline layers, isolated radiating part from the matching circuit, extensive variety of patch, aperture and feed shape types, are the main features of these structures [2]. As an example, slot coupled patch antenna structure of Pozar's work is shown in Figure 1.1.

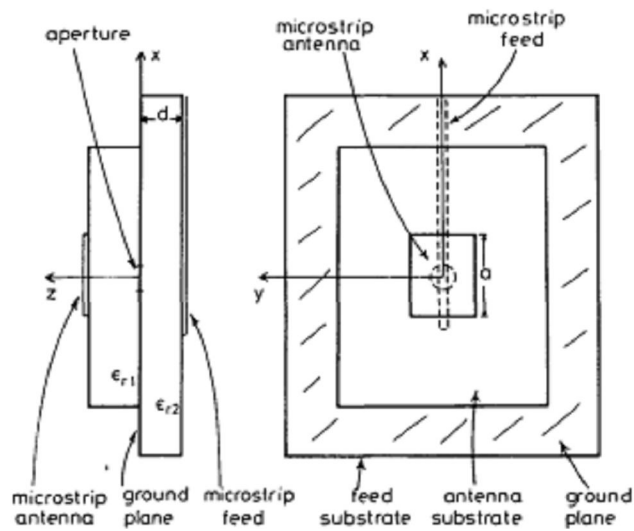


**Figure 1.1 Sideview and topview of a patch antenna slot coupled to a microstripline [1]**

The feed consists of an open-ended microstripline that is located on a dielectric layer below the ground plane. The microstrip patch antenna is located on another dielectric layer above the ground plane and these two microstrips are electromagnetically coupled through an electrically small aperture in the ground plane between them. Besides, some advantages of this technique are presented in [1]. Most important two advantages are as following. First of all, no radiation from the feed microstrip can interfere with the main radiation pattern from the patch, since a ground plane separates the two mechanisms. Secondly, since no direct electrical connection to the antenna elements exists, large probe self reactance or wide microstripline problems which, are avoided [2].

Aperture-coupled patch antenna elements can provide significantly wider bandwidth than conventional printed antennas, while carrying desirable features such as low cost, good reproducibility, and physical robustness. Additionally, they are very suitable for the integration of active elements since the radiating part because of the ground plane. Similarly a complementary study was done about arbitrarily-shaped aperture antennas with the same kind of feed by Chen et al [4].

In [5], slot coupled microstripline antenna is analyzed in terms of its input impedance. Theoretic basis for the analysis is given and design data is produced according to this analysis and verified experimentally. Also in [5] another very important advantage of this technique is explained. This new design technique is highly advantageous when applied to millimeter wave monolithic phased arrays, by forming associated active elements such as phase shifters and amplifiers on a high dielectric substrate. On the other hand, it is preferable to mount the antenna elements on a low dielectric substrate in order to increase the bandwidth [6].

There are two main methods to analyze microstrip structures as quasi-static and full wave analysis. Former assumes the dominant mode propagation as pure transverse electromagnetic (TEM) wave [44]. Hence, microstrip characteristics are calculated from the electrostatic capacitance of the structure, this method is not accurate at higher frequencies. On the other hand, the latter one makes the analysis by considering the other modes of propagation. However, full wave analysis requires more complex and robust calculations.

So far, moment method techniques based on the spectral domain approach [5, 6] have been commonly utilized to solve the problem. Even though these methods generate precise results, the huge amount of computational burden required makes them uneasy to handle in an actual design environment. In [7], a mixed potential integral equation (MPIE) method is developed to analyze the aperture coupled microstrip patch antenna. The method is basically an extension of [8] to aperture coupled geometry. Instead of using the electric field integral equations in [5], the

problem is held as three coupled integral equations in the spatial domain. In order to get rid of enormous numerical task of evaluating the Sommerfeld integrals, closed-form Green's functions [7, 9] are used. Method yields great increase in overall computational speed without sacrificing from the completeness of the problem. In [7–10], the closed-form Green's functions for the potentials of a horizontal electric dipole (HED) are employed.

Since, using closed-form Green's functions in the analysis of microstrip geometry in conjunction with MoM improves computational efficiency; this type of method is used in order to find the current distributions on the microstrip antenna elements in this work. By using surface current distributions, the required parameters are calculated such as input reflection coefficient, and the input impedance, with suitable approximation methods. Besides, the conventional spatial domain Green's functions and spectral domain Green's functions include slowly convergent integrals making them rather disadvantageous than closed-form Green's function [30].

Similar to microstrip line-fed slot coupled antenna, stripline-fed slot coupled patch antenna is analyzed and moment method solutions are developed in [11]. In this work a new computing algorithm is established which combines finite element method and moment method. In [12] a new dual-polarized slot-coupled microstrip patch antenna is presented. This structure can achieve high-isolation, low cross-polarization levels, a wide bandwidth, and low backward radiation levels. The theoretical analysis is based on the finite-difference time-domain (FDTD) method.

In [13] two examples of circularly-polarized slot and slot-coupled patch antennas fed by a microstrip line are designed at 4.8 GHz. In this paper, the MPIE has been successfully applied to analyze the behavior of the arbitrarily shaped slot and slot-coupled patch antennas with a microstrip line feed.

In [14], the analysis of slot-coupled stripline-fed patch antennas with vias is presented. A moment-method scattering formulation is utilized to include the effect of vias on the impedance characteristics of the antenna.

Similar to our study, [14] also divides the entire problem into two coupling problems:

- 1) Coupling between the slot and the stripline feed in the presence of vias.
- 2) Coupling between the slot and the patch.

Method of moments (MoM) with Galerkin's procedure is applied in the spectral domain.

In [15] the problem of an aperture-coupled patch antenna is studied using the spectral domain approach. Elements are determined using integral transform techniques. Several design parameters such as; slot dimensions and inclination with the feedline or the patch, on the resonance frequency and on the input impedance are studied.

In [16] a similar method of our approach is utilized. Mixed-potential integral equation (MPIE) is formulated for the electric and magnetic currents on the aperture-coupled patch antenna. The method of moments (MOM) is used in solving the integral equations using subsectional basis functions. The input impedance and radiation efficiency of various aperture-coupled elements are calculated using the proposed technique. The integral equations are solved via the method of moments (MOM) employing sub-sectional rooftop-shaped basis functions on the patch, aperture, and feed line. The Green's functions are calculated using specialized numerical techniques discussed in [17].

This study deals with the analysis of the aperture coupled patch antenna structures using MoM in conjunction with closed-form Green's functions. In chapter 2, moments method and closed form Green's functions are described and formulized. Next, derivation and calculation of MoM matrix elements are carried out for a multi-layered planar medium. In chapter 3 microstrip coupled-slot antenna structure is

analyzed and the method is verified. Then, aperture-coupled patch antenna geometry is described and an antenna structure, which is proposed in [1], is solved using a MoM code in chapter 4. MoM code is used to calculate current distributions on the microstrip patch and feedline. Feedline, current distributions is used to calculate reflection coefficient parameter of the antenna. Both current distribution and reflection coefficient parameter results are compared to HFSS® outputs. Finally, parametric analysis of the aperture-coupled patch antenna is done in chapter 5. Parametric analysis is carried out by taking some physical dimensions of the antenna as variables, such as slot length, slot position, and stub length. This parametric analysis is carried out by comparing results with HFSS® outputs and the results available in literature.

## CHAPTER 2

### METHOD OF MOMENTS IN MULTILAYER STRUCTURES USING CLOSED FORM GREEN'S FUNCTIONS

MoM is a numerical technique which was first used in electromagnetic theory by R. F. Harrington in 1967 [18]. Generally, most electromagnetic problems can be stated in terms of an inhomogeneous equation as (2-1)

$$Lf(x) = g(x) \quad (2-1)$$

where,  $L$  is a linear operator, which may be differential, integral or integro-differential,  $g(x)$  is the known source function or excitation of the system, and  $f(x)$  is the unknown function to be determined as a result of the moment method process. In this work  $L$  will mostly be an integral operator.

Method of Moments (MoM) is a general procedure for solving (2-1). The method inherits its name from the process of taking moment by multiplying with appropriate weighting functions and integrating. The name 'method of moments' has its roots in Russian Literature [19, 20]. In western literature, the first use of the name is usually referenced to Harrington. The foundation and development of the moment method are completely documented by Harrington [21, 22].

The use of MoM in electromagnetic has become widespread since the work of Richmond in 1965 [23] and Harrington in 1967 [24]. Then the method has been greatly utilized in very large range of EM problems of practical interest such as

microstrips and lossy structures, propagation over an inhomogeneous earth, and antenna beam pattern. An updated review of the method is found in a paper by Ney [25].

MOM is applied to arbitrary integral equations by following the steps:

- (1) Derivation of the appropriate integral equation (IE),
- (2) Conversion of the integral equation into a matrix equation using basis and testing functions.
- (3) Evaluation of the matrix elements,
- (4) Solving the matrix equation and calculating the parameters of interest.

In order to solve (2-1), the unknown function  $f(x)$  is approximated by a linear combination of a set of known functions ( $f_1, f_2, f_3, \dots$ ) which are called as basis functions as shown in (2-2).

$$f(x) = \sum_{n=1}^N \alpha_n f_n(x) \quad (2-2)$$

where  $\alpha$ 's are the unknown coefficients to be determined,  $f_n$ 's are the basis functions and  $N$  is the number of basis functions. By substituting (2-2) into (2-1), the equation (2-3) is obtained.

$$L \left[ \sum_{n=1}^N \alpha_n f_n(x) \right] = g(x) \quad (2-3)$$

Since  $L$  is a linear operator, (2-3) can be transformed into:

$$\sum_{n=1}^N \alpha_n L f_n(x) = g(x) \quad (2-4)$$

Then, the residual or error function is defined as;

$$R(x) = \left[ \sum_{n=1}^N \alpha_n Lf_n(x) \right] - g(x) \quad (2-5)$$

Here, the aim is to make  $R(x)$  arbitrarily small [26]. In order to do that, another set of functions  $(w_1, w_2, w_3, \dots)$  is used. These functions are named as testing functions. Testing functions are utilized to make residual error arbitrarily small in every testing point. By equating the inner product of  $R(x)$  with each  $w_m$  to zero, the expression (2-6) is reached.

$$\sum_{n=1}^N \alpha_n \langle w_m, Lf_n(x) \rangle = \langle w_m, g(x) \rangle \text{ for } m=1,2,3,\dots,N. \quad (2-6)$$

In (2-6) the inner product function is used. This function can be defined as:

$$\langle u, v \rangle = \int_{\Omega} uv^* d\Omega \quad (2-7)$$

Here \* denotes the complex conjugate. Above integration is performed over the entire domain  $\Omega$ . The inner product operation satisfies the following conditions [46]:

$$\begin{aligned} \langle u, v \rangle &= \langle v, u \rangle \\ \langle \alpha u + \beta v, h \rangle &= \alpha \langle u, h \rangle + \beta \langle v, h \rangle \quad \alpha \text{ and } \beta \text{ are constants.} \\ \langle f^*, f \rangle &> 0 \text{ for } f \neq 0 \\ \langle f^*, f \rangle &> 0 \text{ for } f = 0 \end{aligned} \quad (2-8)$$

The set of equations (2-6) can be written in matrix form as shown in (2-9) [46].

$$[I_{mn}][\alpha_n] = [g_m] \quad (2-9)$$

where,

$$[I] = \begin{bmatrix} \langle w_1, Lf_1 \rangle & \langle w_1, Lf_2 \rangle & \dots & \langle w_1, Lf_n \rangle \\ \langle w_2, Lf_1 \rangle & \langle w_2, Lf_2 \rangle & \dots & \langle w_2, Lf_n \rangle \\ \dots & \dots & \dots & \dots \\ \langle w_m, Lf_1 \rangle & \langle w_m, Lf_2 \rangle & \dots & \langle w_m, Lf_n \rangle \end{bmatrix} \quad (2-10)$$

$$\alpha = \begin{bmatrix} \alpha_1 \\ \alpha_2 \\ \vdots \\ \alpha_n \end{bmatrix} \quad \text{and} \quad [g] = \begin{bmatrix} \langle w_1, g \rangle \\ \langle w_2, g \rangle \\ \vdots \\ \langle w_m, g \rangle \end{bmatrix} \quad (2-11)$$

$I$  matrix is called ‘the MoM matrix’ and  $g$  matrix is called the ‘excitation matrix’. In order to find the unknown coefficients matrix, the inverse of the MoM matrix is needed. Inverse of the MoM matrix exist only if it is nonsingular. Then, the unknown coefficients vector equals to the expression:

$$[\alpha_n] = [I_{mn}]^{-1} [g_m] \quad (2-12)$$

For applying MoM, firstly the physical problem is defined by a suitable complete equation. Secondly, the suitable basis and testing functions are selected. By using these basis and testing functions, the unknown function is approximated. Then, the matrix elements are calculated [27]. In the end unknown coefficients,  $\alpha$ ’s, are found by taking the inverse matrix and multiplying the inverse matrix by the excitation vector.

In a MoM application, choosing basis and testing functions is a important step of the problem solution. There are many criteria for basis and testing functions choice.

These functions are selected according to the geometry of the problem, the physical characteristics of the fields, integral equation characteristics, the accuracy needed and the available basis and weighting functions. A discussion on the choice of test and basis functions is provided by [32].

## **2.1 Choice of the Basis and Testing Functions**

### **2.1.1 Choice of the Basis Functions**

There are two types of basis functions: '*Entire Domain Basis Functions*' and '*Sub-Domain Basis Functions*'. According to advantages and disadvantages of each in solution and the accuracy of the problem, one of these methods is chosen.

#### **2.1.1.1 Entire Domain Basis Functions**

If each basis function is defined over the entire calculation domain  $x \in [a, b]$ , then they are called as '*Entire Domain Basis Functions*'. Sine, cosine functions and Chebyshev polynomials are '*Entire Domain Basis Functions*' [47].

#### **2.1.1.2 Sub-Domain Basis Functions**

In order to do calculations easier, entire calculation domain may be dissected into several sub-domains. Definitions of the basis functions may change according to the sub-domains. Basis function can be zero over all of the-sub domains except from interested sub-domain. These kinds of basis functions are called '*Sub-domain Basis Functions*'. For example, if the region  $[a, b]$  is divided into N sub-domains as shown in Figure 2.2, basis function can be represented as (2-13).

$$f(x) = \sum_{n=1}^N \alpha_n f_n(x) = \begin{cases} \alpha_1 f_1(x) & x \in \Delta x_1 \\ \alpha_2 f_2(x) & x \in \Delta x_2 \\ \vdots & \vdots \\ \alpha_N f_N(x) & x \in \Delta x_N \end{cases} \quad (2-13)$$

In many MoM applications, ‘*Sub-domain Basis Functions*’ are used. In this way the integration range becomes smaller when compared to ‘*Entire Domain Basis Functions*’. Besides, calculations are easier. On the other hand, very well chosen ‘*Entire Domain Basis Functions*’ yield much more accurate results. Also choosing suitable ‘*Entire Domain Basis Functions*’, require smaller matrix size compared to sub-domain solutions.



**Figure 2.1 Domain Representation of Entire Domain Basis Function**

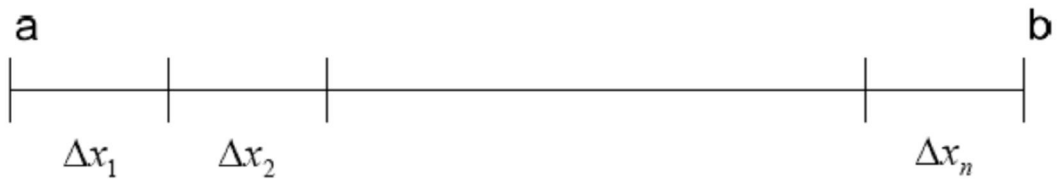


**Figure 2.2 Domain Representation of Sub-Domain Basis Function**

Pulse or piecewise constant functions, piecewise linear or triangular functions, piecewise sinusoidal functions are some other types of the ‘*Sub-domain Basis Functions*’.

## 2.1.2 Choice of the Testing Functions

For different problems, different testing functions may be used in order to make calculation less cumbersome and results more accurate. Some of them are mentioned in the following section.

### 2.1.2.1 Point Matching or Collocation Method

Testing functions are chosen to be Dirac (Kronecker) delta functions in point matching as shown in Figure 2.3. Suppose,  $[a, b]$  represents the spatial domain over which the unknown function is defined,

$$w_m(x) = \delta(x - x_m) \quad \text{for } m=1,2,3,\dots,N \quad (2-14)$$

where,  $w_m$  's are the chosen points in region  $[a, b]$ . Then,

$$\langle w_m, R \rangle = \int_a^b R(x) \delta(x - x_m) dx = 0 \quad (2-15)$$

As it is seen in (2-15), the error function is forced to be zero for the N testing points chosen in the domain. This method is the simplest one. However, the chosen points may not be suitable points and the results may not be accurate enough. On the other hand this kind of choice is not able to represent rapidly changing solution vectors for finite collocation points.

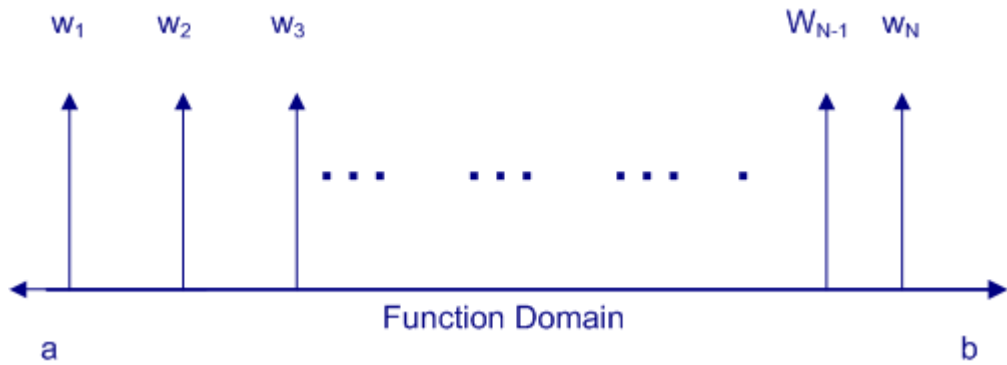


Figure 2.3 Dirac(Kronecker) Delta Function

### 2.1.2.2 Sub-sectional Collocation Method

In this method domain is sectioned into  $N$  sub-domains. Every testing function is defined independently. That is to say, every testing function is defined over a sub-domain, and has no effective contribution on other sub-domains. This method is a conservative version of point matching. In this method following testing function in (2-16) is used [46].

$$w_m(x) = \begin{cases} 1 & x \in \Omega_m \\ 0 & \text{otherwise} \end{cases} \quad \text{and} \quad \int_{\Omega_m} R(x) dx = 0 \quad m = 1, 2, 3, \dots, N \quad (2-16)$$

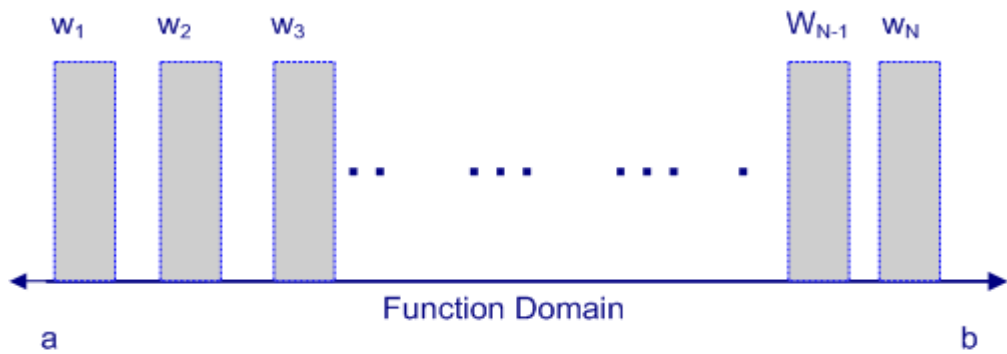


Figure 2.4 Sub-Domains Weighting Function

As it is presented in (2-16), error function is forced to be zero over different sub-domains  $\Omega_m$  of  $\Omega$ . Since the error function is forced at variety points of the domain, results can be more accurate than point matching. However, since the method include one-dimensional integration it is complicated than point matching or collocation method.

### 2.1.2.3 Galerkin's Method

In this method, the testing functions are chosen to be same as the basis functions:

$$w_m = f_m \quad m=1,2,\dots,N \quad (2-17)$$

By using Galerkin's approach, symmetric matrix is at the hand. Regarding the computation time, this method is very advantageous, because finding one row or column is sufficient to set the MoM matrix. However, since the integration over the convolution of basis and testing function is needed, method is more complicated and cumbersome, comparing to point matching or sub-sectional collocation method.

### 2.1.2.4 Method of Least Squares

In this method, testing function is chosen as in (2-18).

$$w_m = Lf_m \quad (2-18)$$

Then, the resulting equation becomes:

$$\sum_{n=1}^N \alpha_n \langle Lf_m(x), Lf_n(x) \rangle = \langle Lf_m(x), g(x) \rangle \quad \text{for } m = 1, 2, 3, \dots, N \quad (2-19)$$

This method yields much more accurate results than the other methods. However, this is the most complicated and bulky one.

## **2.2 Analysis of Planar Printed Structures Using MoM**

In this section, the method used in this work is explained. Firstly, Green's functions are introduced. Secondly, conventional spatial domain MoM formulation and spectral domain MoM formulation are described. Finally, spatial domain closed-form Green's function is given in detail.

### **2.2.1 Green's Function**

Systematic way of obtaining an integral equation from partial differential equation is setting kernel function as the Green's function. The Green's function of a wave equation is the solution of the wave equation for a point source. Because a general source is a linear superposition of point source and wave equation is linear, as the solution of the wave equation for a point source is known, the solution for a general source can also be found using linear superposition [28].

To obtain the field caused by a distributed source by the Green's function technique, we find the effects of each elementary portion of source and add them up. If  $G(r, r')$  is the field at the observation point  $r$  caused by a unit point source at the source point  $r'$ , then the field at  $r$  by a source distribution  $g(r')$  is the integral of  $g(r')G(r, r')$  over the range of  $r'$  occupied by the source. The function  $G$  is the Green's function.

As an example, a scalar wave equation (2-20) in volume  $V$ , represented in Figure 2.5, is taken [46].

$$(\nabla^2 + k^2)\varphi(\vec{r}) = s(\vec{r}) \quad (2-20)$$

Where,  $k$  is the wave number of the medium,  $\varphi(\vec{r})$  is the unknown wave function, and  $s(\vec{r})$  is the vector source function.

First of all, if the Green's function in the same  $V$  is at hand, the problem becomes clearer. The Green's function is the solution of the equation (2-21).

$$(\nabla^2 + k^2)g(\vec{r}, \vec{r}') = -\delta(\vec{r} - \vec{r}') \quad (2-21)$$

Because the general source can be obtained as integration of all sources inside the domain as in (2-22),

$$s(\vec{r}) = \int d\vec{r}' s(\vec{r}') \delta(\vec{r} - \vec{r}') \quad (2-22)$$

Then, by using the principle of linear superposition, the solution of the scalar wave equation (2-20) can be found as:

$$\varphi(\vec{r}) = -\int d\vec{r}' g(\vec{r}, \vec{r}') s(\vec{r}') \quad (2-23)$$

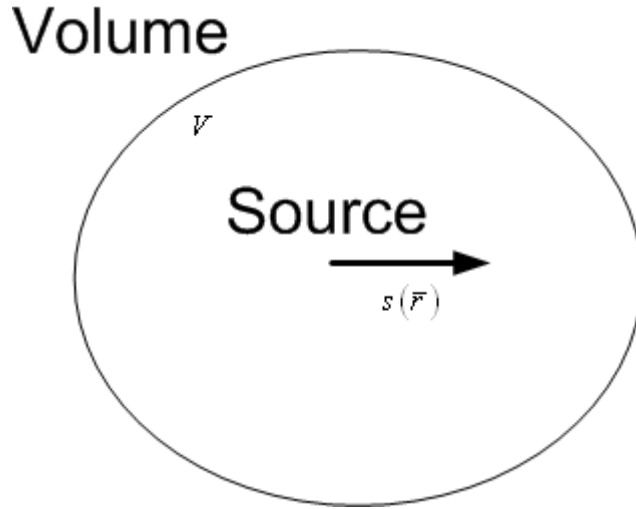


Figure 2.5 The radiation of a source in a volume V [28]

In general, Green's function for the unbounded medium can be stated as shown in (2-24).

$$g(\bar{r}, \bar{r}') = \frac{e^{-jk|\bar{r}-\bar{r}'|}}{4\pi|\bar{r}-\bar{r}'|} \quad (2-24)$$

Hence, the solution of (2-20) is obtained by using (2-24) as [46]:

$$\varphi(\bar{r}) = -\int_V \frac{e^{-jk|\bar{r}-\bar{r}'|}}{4\pi|\bar{r}-\bar{r}'|} s(\bar{r}') \quad (2-25)$$

### 2.2.2 Spatial Domain MoM Formulation

Spatial Domain MPIE MoM formulation employs the spatial domain Green's functions for the vector and scalar potentials which are represented by Sommerfeld integrals. In Figure 2.6, a general microstrip structure is shown. In mixed potential integral equation solution of this structure, substrate layer is assumed to extend to infinity into  $x$  and  $y$  directions. In Figure 2.6,  $d$  denotes the thickness of the substrate

and  $\epsilon_r$  denotes the permittivity of the substrate. Formulation of Green's function presented in this work is for a single layered structure. However, it is valid for all multilayered structures [22]. Furthermore, in this work, the electric type currents are used to solve the geometry, but changing the current type to magnetic currents and analyzing same kind of currents is also possible [29].

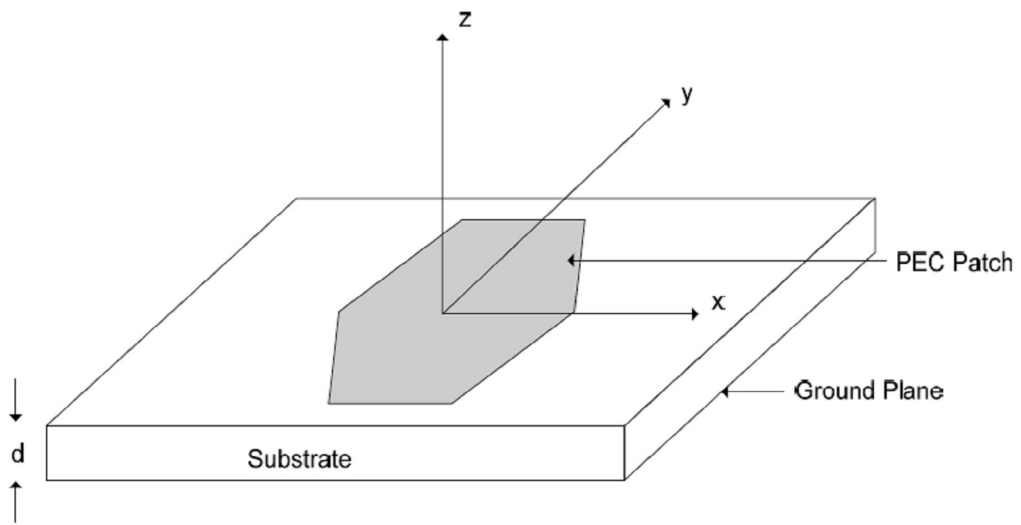


**Figure 2.6 A General Microstrip Structure [10].**

In using MPIE method; integral equation in terms of the induced currents on the conducting surfaces should be obtained [46]. In order to do that electric field is written in terms of vector and scalar potentials,  $\bar{A}$  and  $\phi$ , respectively [30].

$$\bar{E} = -j\omega\bar{A} - \bar{\nabla}\phi \quad (2-26)$$

The vector and scalar potentials can be written in terms of induced surface current density as shown in (2-27) and (2-28) respectively.

$$\bar{A} = \bar{\bar{G}}^A * \bar{J} \quad (2-27)$$

$$\phi = G_q * \left( -\frac{1}{j\omega} \nabla \cdot \bar{J} \right) \quad (2-28)$$

$\bar{\bar{G}}^A$  is the dyadic Green's function of the vector potential, and  $G_q$  is the Green's function of the scalar potential,  $\bar{J}$  is the surface current density and  $*$  denotes the convolution integral [30]. By substituting (2-27) and (2-28) into (2-26) and satisfying the boundary condition at the PEC surfaces, boundary condition integral equation is obtained. The boundary condition at the PEC surfaces is that, the tangential electric field on the perfect electric conductors (PEC) at ( $z = 0$ ) should be zero. On the PEC surface orthogonal components of the electric field can be written down in terms of the surface current as:

$$E_x = -j\omega G_{xx}^A * J_x + \frac{1}{j\omega} \frac{\partial}{\partial x} [G_q * \nabla \cdot \bar{J}] \quad (2-29)$$

$$E_y = -j\omega G_{yy}^A * J_y + \frac{1}{j\omega} \frac{\partial}{\partial y} [G_q * \nabla \cdot \bar{J}] \quad (2-30)$$

where  $E_x$  and  $E_y$  are the  $x, y$  components of the electric field due to source current  $\bar{J}_s$ , respectively[12].

In a MoM application, firstly the current density is expanded as a linear combination of basis functions as in (2-31) and (2-32), where  $N$  is the number of basis functions,  $A_n$  and  $B_n$  are the unknown coefficients of the basis functions,  $J_{xn}$  and  $J_{yn}$ .

$$J_x = \sum_{n=1}^N A_n J_{xn}(x, y) \quad (2-31)$$

$$J_y = \sum_{n=1}^N B_n J_{yn}(x, y) \quad (2-32)$$

In order to insert basis functions and their unknown coefficients to the equations, (2-31) and (2-32) are substituted into (2-29) and (2-30), respectively. Then these field expressions are tested at the observation points with the testing functions  $T_{xm}$  and  $T_{ym}$ .

$$\begin{aligned} & \sum_n A_n \left\{ \left\langle T_{xm}, G_{xx}^A * J_{xn} \right\rangle + \frac{1}{\omega^2} \left\langle T_{xm}, \frac{\partial}{\partial x} \left[ G_q * \frac{\partial}{\partial x} J_{xn} \right] \right\rangle \right\} \\ & + \sum_n B_n \left\{ \frac{1}{\omega^2} \left\langle T_{xm}, \frac{\partial}{\partial x} \left[ G_q * \frac{\partial}{\partial x} J_{yn} \right] \right\rangle \right\} = 0 \end{aligned} \quad (2-33)$$

$$\begin{aligned} & \sum_n B_n \left\{ \left\langle T_{ym}, G_{yy}^A * J_{yn} \right\rangle + \frac{1}{\omega^2} \left\langle T_{ym}, \frac{\partial}{\partial y} \left[ G_q * \frac{\partial}{\partial y} J_{yn} \right] \right\rangle \right\} \\ & + \sum_n A_n \left\{ \frac{1}{\omega^2} \left\langle T_{ym}, \frac{\partial}{\partial y} \left[ G_q * \frac{\partial}{\partial y} J_{xn} \right] \right\rangle \right\} = 0 \end{aligned} \quad (2-34)$$

The inner product terms in (2-33) and (2-34) are five dimensional integral equations. The definition of the inner product already yields two integrations. Furthermore, convolution operation also consists of two more integration. The last integration comes from the Green's function over an infinite domain [46]. For example, one of the integral equations is shown as:

$$\left\langle T_{ym}, G_{yy}^A * J_{yn} \right\rangle = \iint_{D(T)} dx dy T_{ym}(x, y) \iint_{D(B)} dx' dy' G_{yy}^A(x-x', y-y') J_{yn}(x, y) \quad (2-35)$$

Where,  $D(T)$  and  $D(B)$  are the domain of the testing and basis functions, respectively. In this study Green's functions theoretically are:

$$G_{yy}^A(\rho) = \frac{1}{4\pi} \int_{-\infty}^{\infty} dk_p k_p H_0^{(2)}(k_p \rho) \tilde{G}_{yy}^A(\rho) \quad (2-36)$$

where,  $k_p^2 = k_x^2 + k_y^2$ ,  $\rho$  is the variable in cylindrical coordinate system,  $G$  and  $\tilde{G}$  are the Green's functions in the spatial and spectral domains, respectively and  $H_0^{(2)}$  is the Hankel function of the second kind [46]. Spectral domain Green's functions are transformed into spatial domain functions which will be discussed in Closed Form Green's Functions section (Section 2.3) later [37].

In the formulations (2-33) and (2-34), there are some analytical problems regarding singularity issues. Since as  $r \rightarrow 0$ , where  $r$  is distance between source and observation point,  $\bar{G}^A \rightarrow \infty$  and  $G_q \rightarrow \infty$  [46]. This problem must be overcome in calculation phase of MoM matrix. In order to overcome this problem, test and basis functions have to be selected carefully. In doing this the convergence analysis is applied as described in [30]. Hence, a set of piecewise differentiable functions are chosen. Choosing these suitable test and basis functions makes the Green's functions converge. In [31] and [32] proper analysis of the inner product terms as a result of a convolution analysis of the inner product terms are given in detail.

The inner product terms in (2-33) and (2-34) can be transformed into much simpler equations by using (2-37) [30]. Here integration by parts is used. So the inner product term is transformed into an equation which can be calculated analytically. This can be represented as:

$$\left\langle T_{xm}, \frac{\partial}{\partial x} \left[ G_q * \frac{\partial}{\partial x} J_{xn} \right] \right\rangle = - \left\langle \frac{\partial}{\partial x} T_{xm}, G_q * \frac{\partial}{\partial x} J_{xn} \right\rangle \quad (2-37)$$

On the other hand by change of variables the order of the integrals can also be changed.

$$\left\langle T_{xm}, \frac{\partial}{\partial x} \left[ G_q * \frac{\partial}{\partial x} J_{xn} \right] \right\rangle = - \iint dx dy G_q(x, y) \iint dx' dy' \frac{\partial}{\partial x'} T_{xm}(x', y') \frac{\partial}{\partial x'} B_{xm}(x-x', y-y') \quad (2-38)$$

In these equations, inner double integral terms are correlation functions, and could be calculated analytically [30]. In the end, equations (2-33) and (2-34) are converted into the equations which can be evaluated analytically. Calculation methods of these terms are provided in Appendix A. This simplification makes us rid of the inner double integral terms and left only outer double integral term. Then, resulting equation is a two-dimensional integral over a finite domain.

Resulting two dimensional integrals consist of the spatial domain Green's functions which can be obtained by the integration of the spectral domain Green's functions as shown in (2-36). As is it obvious, Bessel function of the first kind is transformed into spectral domain Green's function. Inside the integral there is an oscillatory and slow-converging function. Therefore the calculation of the spatial domain Green's function is difficult in the sense of computational aspects. In order to overcome this problem, closed-form Green's functions method can be utilized [46]. This method will be mentioned in Section 2.3.

At that point, the spectral domain MoM formulation could be analyzed to clarify it is advantageous and disadvantageous over the spatial domain MoM formulation.

### 2.2.3 Spectral Domain MoM Formulation

MoM matrix equation involves convolution integral in the spatial domain. However it is represented by a multiplication in the spectral domain. Hence, (2-39) and (2-40) can be expressed as:

$$\tilde{E}_x(k_x, k_y) = \tilde{Z}_{xx}(k_x, k_y)\tilde{J}_x(k_x, k_y) + \tilde{Z}_{xy}(k_x, k_y)\tilde{J}_y(k_x, k_y) \quad (2-39)$$

$$\tilde{E}_y(k_x, k_y) = \tilde{Z}_{yy}(k_x, k_y)\tilde{J}_y(k_x, k_y) + \tilde{Z}_{yx}(k_x, k_y)\tilde{J}_x(k_x, k_y) \quad (2-40)$$

where,  $\sim$  implies spectral domain representations. The electric field Green's functions,  $Z_{ij}$ , in the spectral domain can somehow be written down in closed-form equations [33]. To apply MoM, spectral domain transformations of the summation of the current distribution functions, (2-31) and (2-32), are substituted into (2-39) and (2-40), firstly. Then, testing with the spectral transformations of the testing functions is applied. Resulting equations are as follows:

$$\sum_n A_n \langle \tilde{T}_{xm}, \tilde{Z}_{xx}\tilde{J}_{xn} \rangle + \sum_n B_n \langle \tilde{T}_{xm}, \tilde{Z}_{xy}\tilde{J}_{yn} \rangle = 0 \quad (2-41)$$

$$\sum_n A_n \langle \tilde{T}_{ym}, \tilde{Z}_{yx}\tilde{J}_{xn} \rangle + \sum_n B_n \langle \tilde{T}_{ym}, \tilde{Z}_{yy}\tilde{J}_{yn} \rangle = 0 \quad (2-42)$$

In (2-41) and (2-42) inner products are defined over the infinite domain as in (2-43).

$$\langle \tilde{T}_{ym}, \tilde{Z}_{yx}\tilde{J}_{xn} \rangle = \iint dk_x dk_y \tilde{T}_{ym}^*(k_x, k_y) \tilde{Z}_{yx}(k_x, k_y) \tilde{J}_{xn}(k_x, k_y) \quad (2-43)$$

As it is presented, the integral dimension is reduced to two, which is a advantage of spectral domain MoM application over the spatial domain approach. However, since spectral domain formulation contains oscillatory and slow converging parts, it needs to be applied with an acceleration technique. Acceleration techniques are in use by subtracting the asymptotic part of the Green's function, calculating the asymptotic part either analytically or in a numerically efficient manner and adding it to the result [34]. Even the acceleration techniques are utilized; the computational burden can be still huge because of the oscillatory nature of the Green's function, especially for the terms for which the observation node coincides with the source node. For all this reasons, the spatial domain MoM formulation in conjunction with the closed-form Green's functions is established as a more efficient method.

### **2.3 Closed-form Green's Functions**

Spectral domain MoM application can be time consuming since it requires infinite domain inner product operation and results an integral equation consists of double integrals. One way to evaluate MoM in the spatial domain is numerical evaluation of the Sommerfeld integral (2-44) which requires repeated calculations and is very time consuming. Hence, instead of the spectral domain MoM employment or the numerical evaluation of the Sommerfeld integral, MoM with the closed-form Green's functions can be applied. That results in two-dimensional integral equations in finite domains. This approach was first introduced in [35] for a one-layer planar medium for a horizontal electric dipole (HED) over a thick substrate on a ground plane. In this method, spectral domain Green's functions are approximated as closed-form expressions by using an approximation method. Next, using Prony's method and least-square Prony's method, this study is improved in [36] for a two-layer planar medium. This method is developed and made all applicable for different kind of sources as horizontal electric, magnetic, and vertical electric, magnetic dipoles embedded in general, multilayer, planar media in [37]. In this study, the general closed-form Green's functions of the vector and scalar potentials of sources located in an arbitrary layer of a planar-layered medium will be utilized.

A typical multi-layer medium is shown in Figure 2.7. The sources and the observation point can be located in any layer. The electric and magnetic properties  $(\epsilon_r, \mu_r)$  and the thicknesses of each layer are arbitrary either [46]. The layers extend to infinity in both  $x$  and  $y$  directions.

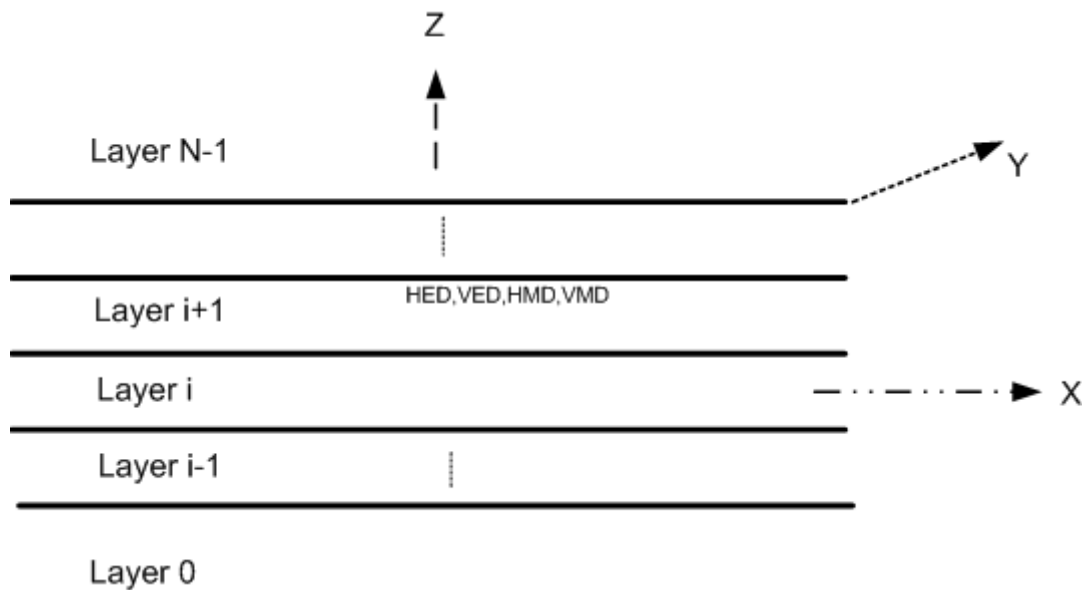


**Figure 2.7 A Typical Layered Medium with Embedded Sources in Layer-i.**

The general algorithm for calculating the general closed-form Green's functions is outlined as below [37]:

- i) Green's functions in the spectral domain are derived;
  - a.) Green's functions are derived in the source layer,
  - b.) Green's functions in the observation layer are derived using an iterative algorithm applied to TE-TM components of the Green's functions in the source layer,
- ii) Spatial domain, closed-form Green's functions are derived;
  - a) In this method the surface wave poles and the direct terms are extracted first. Then the spectral Domain Green's functions are

approximated in terms of complex exponentials, which are gathered from the approximation scheme, generalized pencil of function (GPOF) [38].

b) Closed-form Green's functions are obtained using the Sommerfeld integrals property for each complex exponential.

Spectral domain Green's functions are derived for the scalar and vector potentials in detail in [37] using the similar methods described in [28]. The spatial domain Green's functions are expressed by using the spectral domain Green's functions as in (2-44) [7]:

$$G_{yy}^A(\rho) = \frac{1}{4\pi} \int_{-\infty}^{\infty} dk_p k_p H_0^{(2)}(k_p \rho) \tilde{G}_{yy}^A(\rho) \quad (2-44)$$

These types of integrals are called as Sommerfeld integrals. These Sommerfeld integrals can not be evaluated analytically. In order to make analytical evaluation possible in (2-44), the spectral domain Green's function is approximated by exponentials. Then the spatial domain Green's functions can be evaluated analytically using the well-known Sommerfeld identity [7]:

$$\frac{e^{-jk_s r}}{r} = -\frac{1}{2} \int_{SIP} dk_p k_p H_0^{(2)}(k_p \rho) \frac{e^{-jk_z |z|}}{z} \quad (2-45)$$

where, SIP is the Sommerfeld integration path [39].

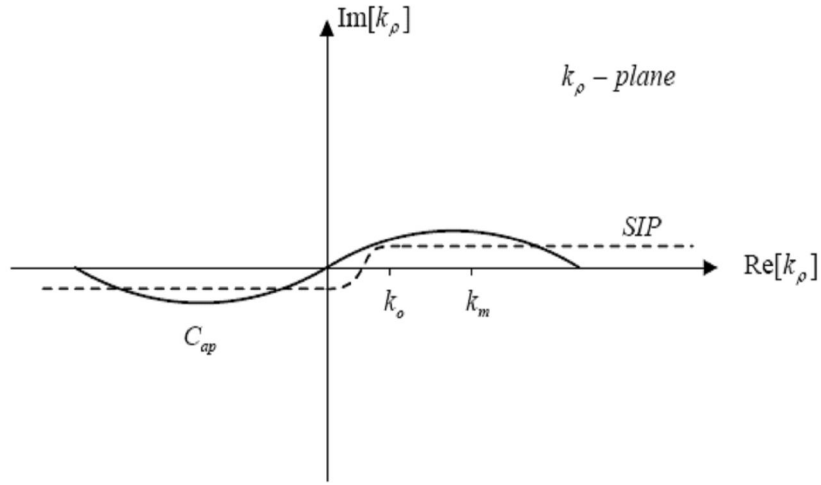


**Figure 2.8 Definitions of the Sommerfeld Integration Path and Integration Path for One Level Approximation [40].**

In [37], the spatial domain Green's functions are derived by using an approximation method which is the generalized pencil of function (GPOF) method, for approximation of the spectral domain Green's functions with the complex exponentials. Analogous to the other two methods, Prony and least-square Prony, the generalized pencil of function (GPOF) method requires uniform sampling of a complex valued-function versus a real variable. Sampling along any variable would yield exponentials in terms of the same variable. Hence any sampling along the variable  $k_\rho$  would give exponential terms of  $k_\rho$ . On the other hand, to use the Sommerfeld identity, the exponentials should be in terms of  $k_z$ . In order to gather exponentials in terms of  $k_z$ , a deformed path on  $k_z$  plane must be defined. This is defined as a mapping of a real variable  $t$  onto the complex plane  $k_z$  as [46]:

$$k_z = k \left[ -jt + \left( 1 - \frac{t}{T_0} \right) \right], \quad 0 \leq t \leq T_0 \quad (2-46)$$

where,  $k_z$  and  $k$  are defined in the source layer [37]. The integration path is shown in Figure 2.8. The Green's functions are uniformly sampled uniformly on  $t \in [0, T_0]$ . By this way Green's function is mapped onto the  $C_{ap}$ , with  $k_{\rho \max} = k \left[ 1 + T_0^2 \right]^{\frac{1}{2}}$ . This function is approximated in terms of exponentials of  $t$  which can easily be transformed into a form of exponentials of  $k_z$ . The approximation which uses this method is called the one-level approximation because the complex function to be approximated is sampled between zero and  $T_0$  and it is negligible from then on [38].

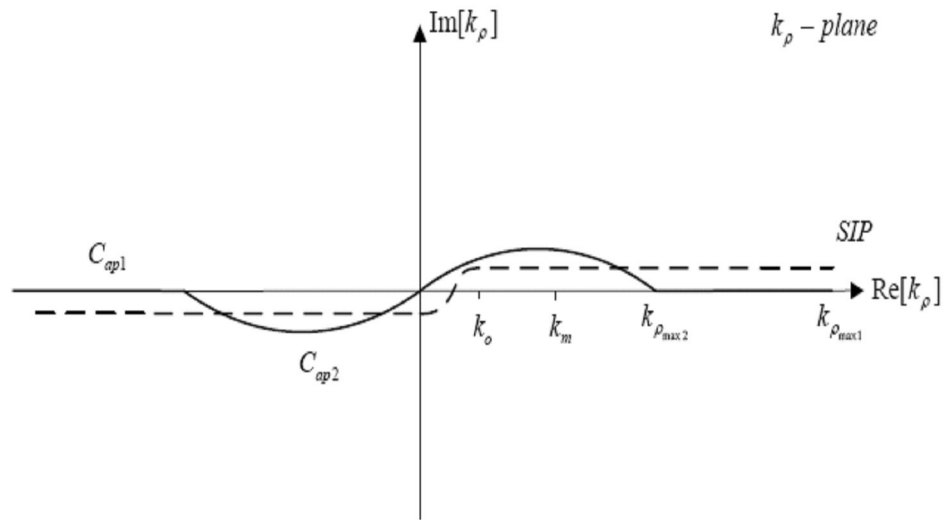


**Figure 2.9 The Paths and Used in Two-Level Approximation [40].**

There is a trade-off in choosing the approximation parameters. The number of samples should be large enough to follow the rapid changes for small values of  $k_\rho$ . On the other hand  $T_0$  should be chosen large enough to fit the asymptotic behavior of the Green's function. However, this would result an over-sampling at large values of

$k_\rho$ . Since for large values of  $k_\rho$ , Green's function is generally slowly varied [30], oversampling at large values of  $k_\rho$  is redundant. In order to overcome this problem, in [40] it is suggested that, GPOF method should be applied in two level approximations. Using this approach, the first part of the approximation is performed along the path  $C_{ap1}$  while the second part is done along the path  $C_{ap2}$  as shown in Figure 2.9. In the first approximation, the asymptotic behavior of the function is extracted and then in the second phase, the details and high frequency features of the second function are approximated by using small number of sampling points. Two different functions are used to map the real variable  $t$  onto the complex variable  $k_z$  along the paths  $C_{ap1}$  and  $C_{ap2}$ , as it is given in [30]. These two functions can be represented as:

$$C_{ap1} : k_z = -jk_s [T_{02} + t], \quad 0 \leq t \leq T_{01} \quad (2-47)$$

$$C_{ap2} : k_z = k_s \left[ jt + \left( 1 - \frac{t}{T_{02}} \right) \right], \quad 0 \leq t \leq T_{02} \quad (2-48)$$

As a result of the two-level approximation, the spectral domain scalar Green's functions can be written as:

$$\tilde{G} \cong \frac{1}{j2\varepsilon_i k_{zi}} \left[ e^{-jk_{zi}|z|} + \sum_{n=1}^{N_1} a_{1n} e^{-\alpha_{1n} k_{zi}} + \sum_{n=1}^{N_2} a_{2n} e^{-\alpha_{2n} k_{zi}} \right] \quad (2-49)$$

Where,  $a_{1n}$  and  $\alpha_{1n}$  are the coefficients gathered from the first part,  $a_{2n}$  and  $\alpha_{2n}$  are from the second part of the two-level approximation. Next, by substituting spectral domain representation into the Sommerfeld identity (2-45), the following closed-form spatial domain Green's function is written down.

$$G \cong \frac{1}{4\pi\varepsilon_i} \left[ \frac{e^{-jk_i r}}{r} + \sum_{n=1}^{N_1} a_{1n} \frac{e^{-jk_i r_{1n}}}{r_{1n}} + \sum_{n=1}^{N_2} a_{2n} \frac{e^{-jk_i r_{2n}}}{r_{2n}} \right] \quad (2-50)$$

where,  $r_{1n} = \sqrt{x^2 + y^2 - \alpha_{1n}^2}$  and  $r_{2n} = \sqrt{x^2 + y^2 - \alpha_{2n}^2}$  are the complex distances calculated using the real distance and coefficients obtained,  $k_i$  is the wave number in the source layer. (2-48) and (2-49) are obtained by direct sampling of spectral domain Green's functions [41]. As a result, (2-49) and (2-50) turns into:

$$\tilde{G} \cong \frac{1}{j2\varepsilon_i k_{zi}} \left[ \sum_{n=1}^{N_1} a_{1n} e^{-\alpha_{1n} k_{zi}} + \sum_{n=1}^{N_2} a_{2n} e^{-\alpha_{2n} k_{zi}} \right] \quad (2-51)$$

$$G \cong \frac{1}{4\pi\varepsilon_i} \left[ \sum_{n=1}^{N_1} a_{1n} \frac{e^{-jk_i r_{1n}}}{r_{1n}} + \sum_{n=1}^{N_2} a_{2n} \frac{e^{-jk_i r_{2n}}}{r_{2n}} \right] \quad (2-52)$$

The representation (2-52) can be simplified as:

$$G \cong \sum_{m=1}^{N_2} a_m \frac{e^{-jk_i r_m}}{r_m} \quad (2-53)$$

where  $r_m = \sqrt{\rho^2 - b_m^2}$  is the general form of the complex distance and  $k_i$  is the wave number of the source medium. According to the formulation given in [37], the coefficients for any layered medium with located sources are calculated by a computer program. In different geometry and medium solutions of this study, outcomes of this program are used.

Choosing, the correct approximation parameters in two-level approximation scheme one could get the approximated Green's functions successfully. As the level count of the approximation scheme increases, number of samples per level also increases.

Hence using, two-level approximation is better than using single-level approximation scheme. On the other hand, two-level approximation scheme can also be used to improve to multi-level approximation scheme.

One time calculation of closed form Green's function coefficients for a layered structure is sufficient for all. Then, these values can always be used, in the analysis of many similar-layered microstrip geometries. This is the major advantage of the using closed-form Green's functions.

In this chapter, first, a brief description of MoM formulation is introduced. Next, the Green's functions are presented. The spatial domain and spectral domain MoM formulation in conjunction with the Green's functions are detailed and the two approaches are compared for their advantages and disadvantages. Finally, the closed-form Green's function in spatial domain is discussed. In the next chapters, by using the closed-form Green's functions, analysis of microstrip fed-slot antenna and slot coupled patch antenna structures will be formulized, electrical and magnetic current distributions will be evaluated in necessary locations. Finally, using the current distributions, some antenna parameters will be calculated.

## CHAPTER 3

### MoM ANALYSIS OF THE MICROSTRIP FED SLOT ANTENNA

In this chapter, a microstrip fed-slot antenna is analyzed. This is a preparation chapter for the microstrip fed-slot coupled patch antenna analysis. Firstly, the method will be applied to a relatively simpler structure which is also a building component of the slot coupled patch antenna structure. Then, in chapter 4, formulation and analysis of slot coupled patch antenna is given.

The current distribution on the microstrip feed line and the slot are calculated using closed-form Green's function in the spatial domain in conjunction with Galerkin's method of moment. Firstly, a microstrip fed-slot coupled patch antenna structure is set. According the structure, microstrip to slot and slot to microstrip coupling equations are derived as explained in chapter 4. Then the current distribution on the microstrip line is calculated using MoM code written in Matlab®. By getting current distribution on the microstripline, antenna reflection coefficient is calculated using Prony's method [42]. Frequency versus S11 characteristic of the slot structure yields the resonance frequency. In this work, Alexopoulos' microstrip to slot scheme [45] is used in order to verify MoM computer code.

#### **3.1 Definition of the Structure**

Microstrip fed-slot coupled structure contains one-layer dielectric. This scheme of antenna does not require an electrical connection between the slot and microstripline. Figure 3.1 and Figure 3.2 demonstrates the antenna structure proposed in [45].

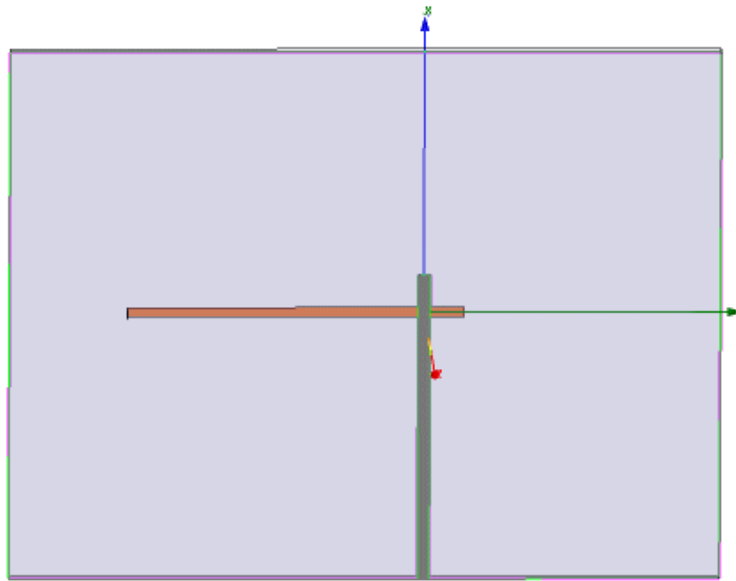


**Figure 3.1 General strip coupled slot antenna structure.**

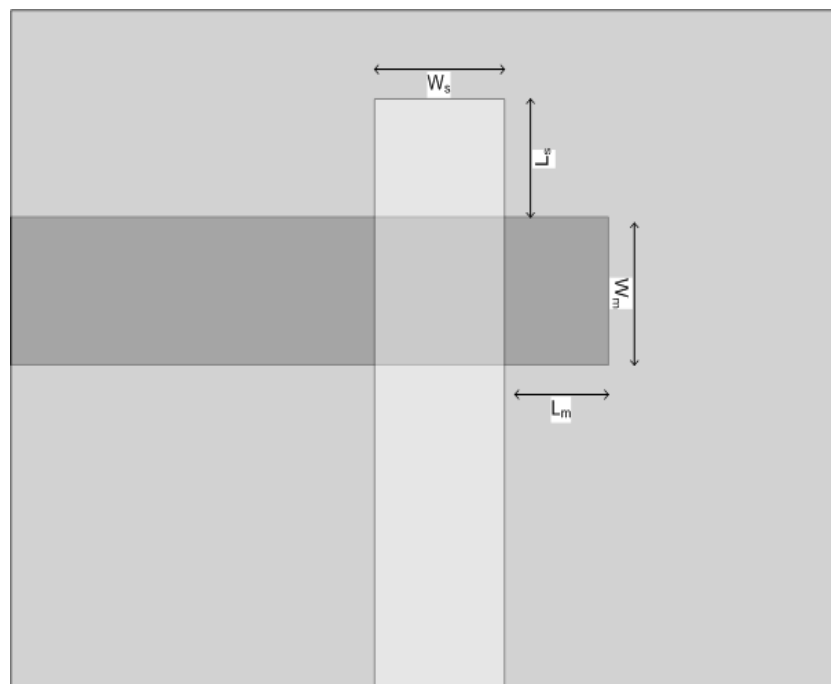


**Figure 3.2 Strip to slot structure (dimensions).**

The parameters of the structure given in Figure 3.2 are:

$L_m = \text{length}$  of the microstrip stub

$L_s = \text{length}$  of the slot

$W_m = \text{width}$  of the microstrip stub

$W_s = \text{width}$  of the slot

On the other hand, since the structure is based on the Alexopoulos' work, for comparison purposes, other parameters are taken from there such as relative dielectric constant ( $\epsilon_r = 20$ ) and substrate thickness ( $d_s = 0.3175$  cm).

### **3.2 Formulation**

By using the equivalence principle we can separate the slot problem into two different regions by closing the aperture with a PEC. In order to maintain the original field in both regions, surface currents must exist in the both faces of the aperture. These currents are written down according to the related boundary conditions.

$$\overline{J} = \overline{nxH} \quad (3-1)$$

$$\overline{M} = \overline{Exn} \quad (3-2)$$

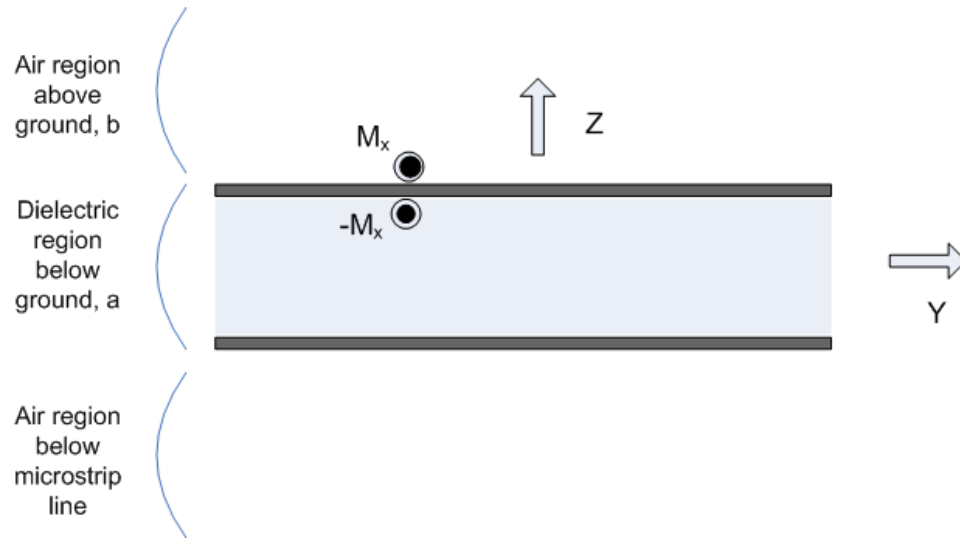


Figure 3.3 Strip coupled slot structure (sideview).

According to our model, only magnetic currents exist on both surfaces of the aperture. Then the related boundary conditions are derived. First, boundary condition on the aperture is considered. The tangential magnetic field is continuous across the aperture. This happens to be our first boundary condition. Since, aperture is assumed to be very narrow, only  $x$ -directed magnetic currents are considered. On the aperture's both sides,  $x$ -directed magnetic fields must be equal.

$$H_x^a(J) + H_x^a(-M_x) = H_x^b(M_x) \quad (3-3)$$

By using magnetic vector potential and magnetic scalar potential we can write magnetic field:

$$\bar{H} = -j\omega\epsilon\bar{F} - \nabla\Phi^m \quad (3-4)$$

Scalar magnetic potential and vector magnetic potential are formulated using magnetic Green's functions:

$$\Phi^m = G^{q_m} * \left( -\frac{1}{j\omega} \nabla \cdot \overline{M} \right) \quad (3-5)$$

$$\overline{F} = \overline{\overline{G^F}} * \overline{M} \quad (3-6)$$

Dyadic Green's function is used in finding vector magnetic potential based on the magnetic current:

$$\overline{\overline{G^F}} = \hat{x}\hat{x}G_{xx} + \hat{y}\hat{y}G_{yy} + \hat{z}\hat{z}G_{zz} \quad (3-7)$$

By using scalar and vector potential and the magnetic current, general magnetic field expression is written as:

$$\overline{H} = -j\omega\epsilon\overline{\overline{G^F}} * \overline{M} - \nabla \left[ G^{q_m} * \left( -\frac{1}{j\omega} \nabla \cdot \overline{M} \right) \right] \quad (3-8)$$

Since we are interested only in  $x$ -directed magnetic field, we can reduce the equation to only  $x$ -directed components. The magnetic field due to magnetic current above the aperture, in the air region, is formulated as:

$$H_x^b(M_x) = -j\omega\epsilon G_{xx_b}^F * M_x + \frac{1}{j\omega} \frac{\partial}{\partial x} \left( G_{X_b}^{q_m} * \frac{\partial}{\partial x} M_x \right) \quad (3-9)$$

Besides, the magnetic field due to magnetic current below the aperture, in the dielectric region, is formulated as:

$$H_x^a(M_x) = -j\omega\epsilon G_{xx_a}^F * (-M_x) + \frac{1}{j\omega} \frac{\partial}{\partial x} \left( G_{X_a}^{q_m} * \frac{\partial}{\partial x} (-M_x) \right) \quad (3-10)$$

In order to complete the slot boundary region equations, we need one more component. In the dielectric region there must exist another magnetic field component due to electric current on the microstrip line.

By using vector electric potential, magnetic field below the aperture is formulated.

$$\overline{H} = \frac{1}{\mu} \nabla \times \overline{A} \quad (3-11)$$

Since we are only interested in  $x$ -directed magnetic field, vector electric potential is reduced such a way that its curl yields only  $x$ -directed components.

$$\overline{H}_x = \frac{1}{\mu} \nabla \times (\overline{A}_y + \overline{A}_z) \quad (3-12)$$

As a result  $x$ -directed magnetic field is written using  $y$  and  $z$ -directed vector potentials.

$$\overline{H}_x = \frac{1}{\mu} \left( -\frac{\partial}{\partial z} A_y + \frac{\partial}{\partial y} A_z \right) \quad (3-13)$$

The  $y$  and  $z$  directed electrical vector potentials are written by using  $y$ -directed electric currents and suitable dyadic Green's functions are used.

$$A_y = G_{yy}^A * J_y \quad (3-14)$$

$$A_z = G_{zy}^A * J_y \quad (3-15)$$

Then  $x$ -directed magnetic field in the dielectric region is found as:

$$\overline{H_x^a}(\overline{J}) = \frac{1}{\mu} \left( -\frac{\partial}{\partial z} G_{yy}^A * J_y + \frac{\partial}{\partial y} G_{zy}^A * J_y \right) \quad (3-16)$$

As a result, first boundary condition is set upon  $x$ -directed magnetic field across the aperture.

$$\begin{aligned} -j\omega(G_{xx_a}^F + G_{xx_b}^F) * M_x + \frac{1}{j\omega} \frac{\partial}{\partial x} \left[ (G_{x_a}^{q_m} + G_{x_b}^{q_m}) * \frac{\partial}{\partial x} M_x \right] \\ - \frac{1}{\mu} \left( \frac{\partial}{\partial y} G_{zy_a}^A * J_y - \frac{\partial}{\partial z} G_{yy_a}^A * J_y \right) = 0 \end{aligned} \quad (3-17)$$

Next, other boundary condition equation related to microstrip line must be derived. Since there is no magnetic current on the microstrip line and it is assumed to be a very narrow PEC, the tangential electric field on the microstrip line surface must vanish. That is to say, on the microstrip surface  $y$ -directed tangential electric field must equal to zero. There is three components creating the  $y$ -directed field on the microstrip.

$$E_y^a(\overline{J}) + E_y^a(\overline{M_x}) + E_y^{inc} = 0 \quad (3-18)$$

In order to find  $y$ -directed electric field due to magnetic current, vector magnetic potential is used.

$$E_y^a(\overline{M_x}) = \frac{1}{\varepsilon} (\nabla_x \overline{F}) \quad (3-19)$$

Then the equation is reduced only to  $y$ -directed electric field yielding components as:

$$E_y^a(\overline{M_x}) = \frac{1}{\varepsilon} \left( \frac{\partial}{\partial z} F_x - \frac{\partial}{\partial x} F_z \right) \quad (3-20)$$

Vector magnetic potentials in  $x$  and  $z$  directions are found by using magnetic currents and suitable Green's functions such as:

$$F_x = G_{xx_a}^F * M_x \text{ and } F_z = G_{zx_a}^F * M_x \quad (3-21)$$

As a result,  $y$ -directed electric field on the microstrip line surface is written as:

$$E_y^a(\overline{M}_x) = \frac{1}{\varepsilon} \left( \frac{\partial}{\partial z} (G_{xx_a}^F * M_x) - \frac{\partial}{\partial x} (G_{zx_a}^F * M_x) \right) \quad (3-22)$$

Secondly, we find  $y$ -directed electric field due to electric current, which exists on the microstrip line surface. Electric field is written using vector and scalar electrical functions.

$$E^a(\overline{J}_y) = -j\omega \overline{A} - \nabla \phi \quad (3-23)$$

Potential functions are written down as convolutions of dyadic Green's function and the electric current.

$$E^a(\overline{J}_y) = -j\omega (G_{yy_a}^A * J_y) - \nabla (G_{y_a}^q * \left( -\frac{1}{j\omega} \nabla \cdot J_y \right)) \quad (3-24)$$

Then, the equation is reduced to  $y$ -directed components only.

$$E_y^a(\overline{J}_y) = -j\omega (G_{yy_a}^A * J_y) + \frac{1}{j\omega} \frac{\partial}{\partial y} \left( G_{y_a}^q * \frac{\partial}{\partial y} J_y \right) \quad (3-25)$$

As a result, the second boundary condition is established as:

$$\begin{aligned}
& -j\omega(G_{yy}^A * J_y) + \frac{1}{j\omega} \frac{\partial}{\partial y} \left( G_{yy}^q * \frac{\partial}{\partial y} J_y \right) + \frac{1}{\varepsilon} \left( \frac{\partial}{\partial z} (G_{xx}^F * M_x) \right) \\
& - \frac{1}{\varepsilon} \left( \frac{\partial}{\partial x} (G_{zx}^F * M_x) \right) + E_0 = 0
\end{aligned} \tag{3-26}$$

### 3.2 Current Distribution Results

Strip coupled slot geometry can be solved using method of moments in conjunction with the closed form Green's functions with the parameters which are given in Figure 3.2 as:  $L_m = 0.69$  cm,  $L_s = 0.69$  cm,  $W_m = 0.16$  cm,  $W_s = 0.2$  cm. Since the geometry has a wide-band antenna characteristics, simulations are done in wide range of frequencies. Some of these simulation results are depicted below.

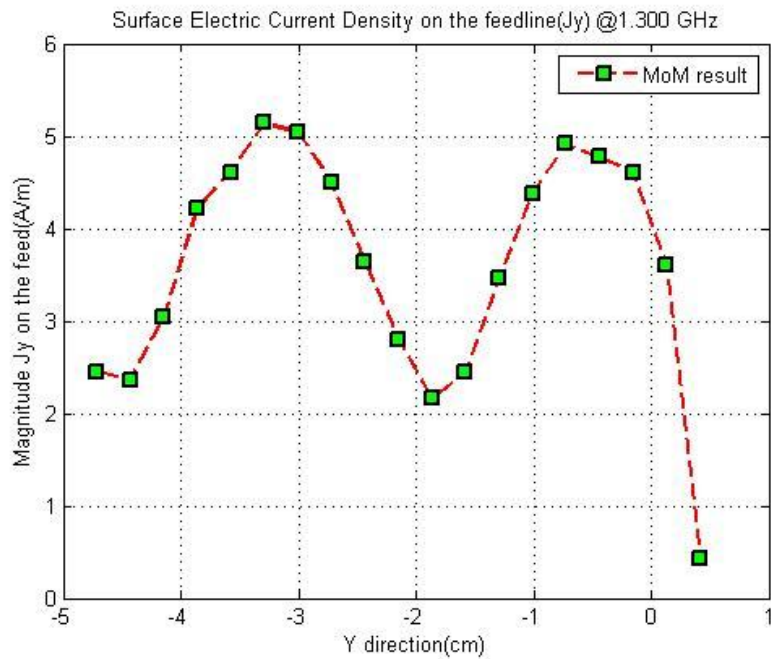


Figure 3.4 Surface electric current distribution on the microstrip feed at 1.3 GHz.

Having completed the current distribution calculations, current distribution function could be approximated using Prony analysis [42] which is explained in Appendix B. As a result of this analysis, parameters of the current distribution function given in (3-27) are obtained.

$$I(x) \cong c_1 e^{-\beta_1 x} + c_2 e^{\beta_2 x} \quad (3-27)$$

According to (3-27) incoming and reflecting wave coefficients can be used to evaluate reflection coefficient.

$$c_1 = 1.5449 - 3.5007i$$

$$c_2 = -1.7077 - 0.9905i$$

$$\beta_1 = -3.3329 - 84.7337i$$

$$\beta_2 = -18.1541 + 86.5575i$$

These parameters can be used to evaluate reflection coefficient ( $\Gamma = \frac{c_2}{c_1}$ ).

In the same frequency magnetic current distribution for  $\lambda/2$  slot length on either side of the aperture are also evaluated as in Figure 3.5.

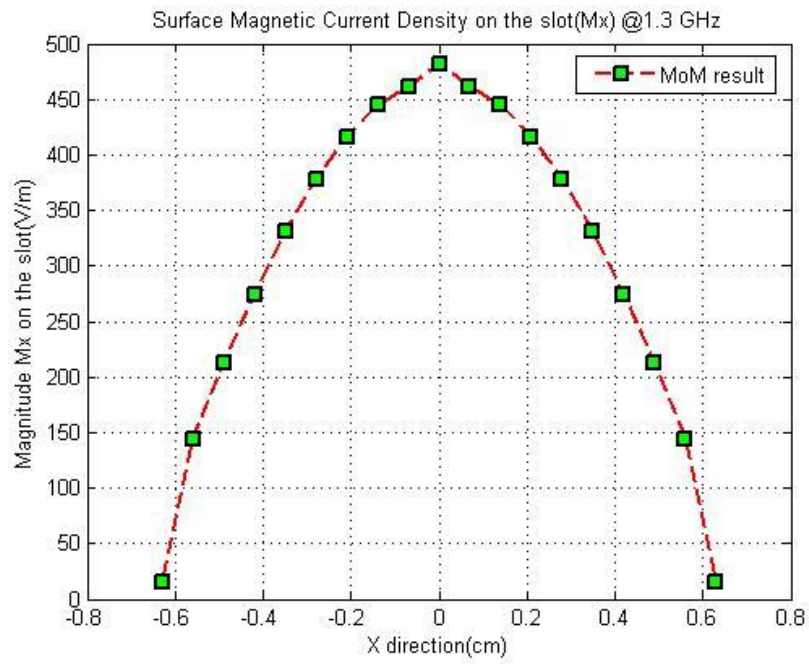


**Figure 3.5 Surface magnetic current distribution on the slotline at 1.3 GHz.**

In Figure 3.6 feedline current distribution for  $1.2\lambda$  strip at 1.5 GHz is shown.

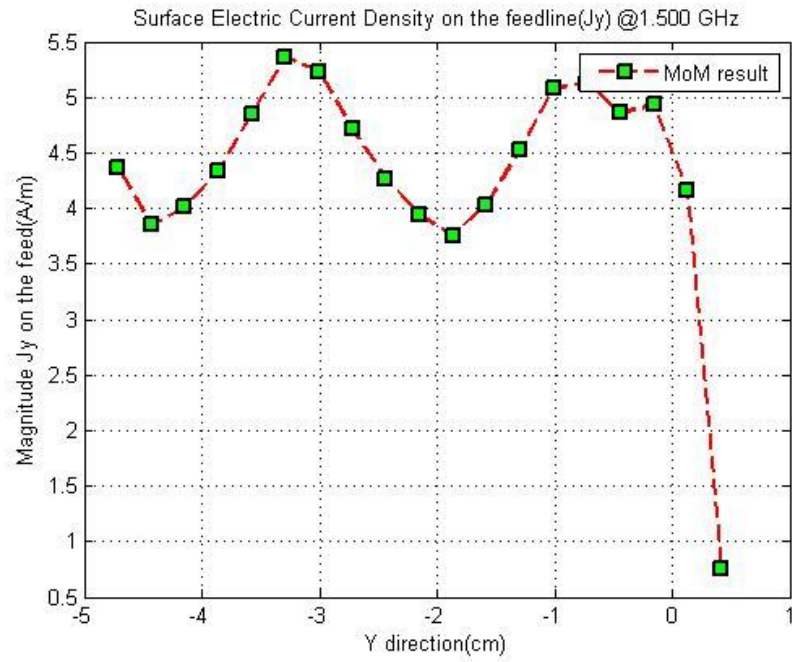


**Figure 3.6** Surface electric current distribution on the microstrip feed at 1.5 GHz.

Then, the current distribution function could be approximated using Prony analysis. As a result of this analysis, current distribution function parameters of (3-27) are evaluated as:

$$c_1 = 2.6817 + 3.6911i$$

$$c_2 = 0.3484 - 0.4795i$$

$$\beta_1 = -0.0230 - 93.31i$$

$$\beta_2 = 0.1664 + 94.38i$$

Next, in Figure 3.7 feedline current distribution for  $2\lambda$  strip at 2.5 GHz is given.

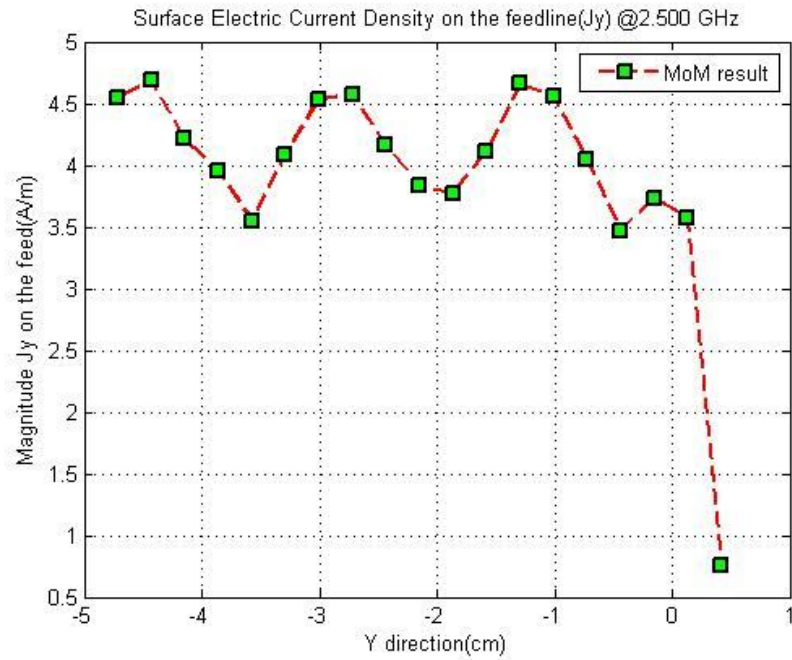


**Figure 3.7 Surface electric current distribution on the microstrip feed at 2.5 GHz.**

As a result of the Prony analysis, current distribution function parameters of (3-27) are obtained.

$$c_1 = -3.6408 - 2.0614i$$

$$c_2 = 0.5030 - 0.0828i$$

$$\beta_1 = -0.0078 - 158.20i$$

$$\beta_2 = -0.0482 + 163.48i$$

Next, in Figure 3.8 feedline current distribution  $2.4\lambda$  strip at 3.0 GHz is shown.

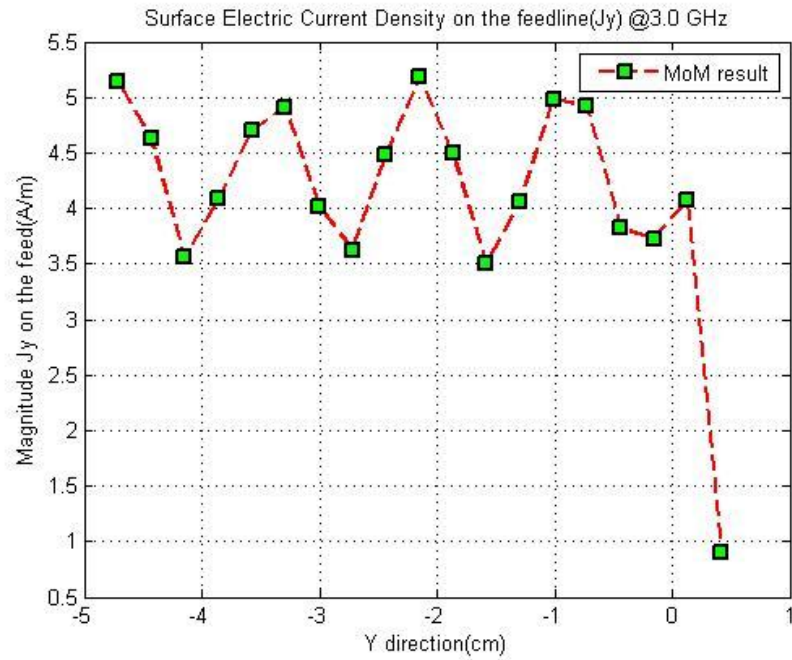


**Figure 3.8 Surface electric current distribution on the microstrip feed at 3.0 GHz.**

As a result of the Prony analysis, current distribution function parameters of (3-27) are obtained.

$$c_1 = -0.4644 - 4.3655i$$

$$c_2 = 0.6638 - 0.6029i$$

$$\beta_1 = -0.0111 - 202.00i$$

$$\beta_2 = -0.1241 + 204.66i$$

As a result of the evaluated current distribution functions, and reflection coefficients, S11 variance throughout 1.3-4 GHz frequency band is obtained. This S11 data of strip coupled slot structure is shown in Figure 3.9 in comparison with Alexopoulos' results [45].

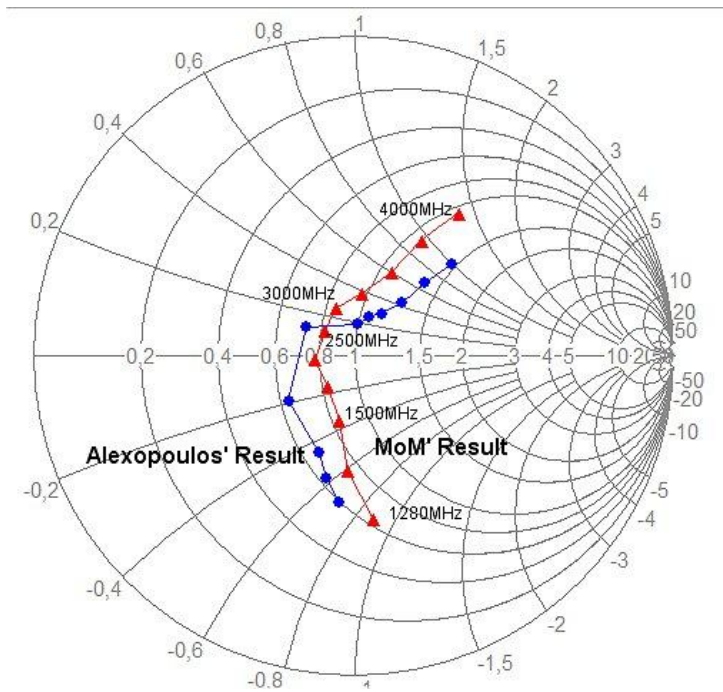


**Figure 3.9 S11 characteristic of strip coupled slot antenna between 1.3-4.5GHz.**

According to the analysis of the strip coupled-slot structure with the closed form Green's functions, these results are obtained. According to the comparative analysis shown in Figure 3.9, results are much more similar to the Alexopoulos' results in the true resonant frequency than other frequencies. However, other than resonance, frequency sweep analysis yields reasonably similar results.

Having overviewed the strip coupled slot interaction, microstrip fed-slot coupled patch antenna formulation and analysis is held as the main focus of this study in the next chapters.

## CHAPTER 4

### MoM ANALYSIS OF THE MICROSTRIPLINE FED-SLOT COUPLED PATCH ANTENNA

In this chapter, a microstrip fed-slot coupled patch antenna is analyzed. The current distribution on the microstrip feed line and the patch are calculated using closed-form Green's function in the spatial domain in conjunction with Galerkin's method of moment. Firstly, a microstrip fed slot coupled patch antenna structure is set. According the structure, microstrip to slot and slot to patch coupling equations are derived. Then the current distribution on the microstrip line is calculated using MoM code written in Matlab®. By getting current distribution on the microstrip line, reflection coefficient value is calculated using Prony's method [42]. Frequency versus S11 characteristic of the patch antenna yields the resonance frequency of the antenna. At this resonance frequency two-dimensional current distribution is calculated and demonstrated with plots. In this work, Pozar's microstrip fed-slot coupled patch antenna scheme [1] is used as a start-up structure in order to verify MoM computer code. Finally, other parameters and structural changes are analyzed and the results are demonstrated.

#### ***4.1 Definition of the Structure***

Microstrip fed-slot coupled patch is an antenna structure which contains two-layer of dielectrics. This scheme of antenna does not require an electrical connection between the radiating part and feed line. The structure involves two substrates separated by a ground plane. One substrate contains the radiating patch, while the other substrate contains the feed. Figure 4.1 and Figure 4.2 demonstrates the antenna structure proposed in [1].

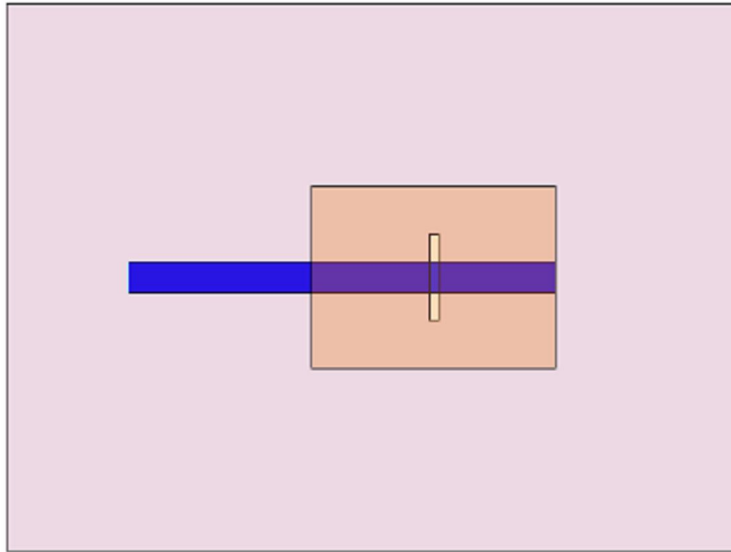


**Figure 4.1 Slot Coupled Patch Antenna.**

There is a small aperture in the ground plane, also known as slot, which allows coupling between microstrip feed and microstrip patch. The feed is generally in the form of open circuited stub [1].

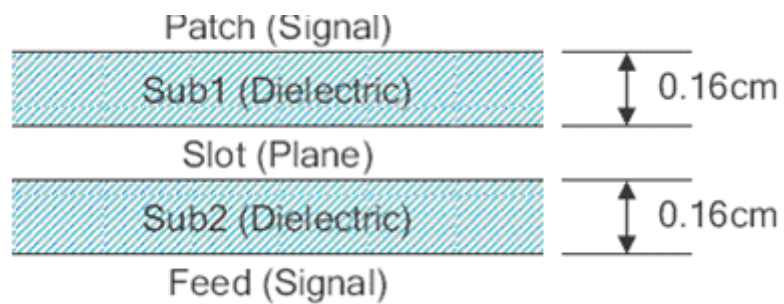


**Figure 4.2 Slot Coupled Patch Antenna (side view).**

## 4.2 Establishment of the Problem

In previous chapter it is stated that, the electric field can be expressed in terms of scalar and vector potentials. Besides, the scalar and the vector potentials can be written in terms of induced surface current densities. Similarly, magnetic field can also be expressed in terms of scalar and vector potentials as in (4-1).

$$\bar{H} = -j\omega\bar{F} - \bar{\nabla}\phi^m \quad (4-1)$$

Magnetic vector and scalar potential functions can be formulated using magnetic Green's functions and magnetic current densities as shown in (4-2) and (4-3).

$$\phi^m = G^m * \left(-\frac{1}{j\omega}\nabla\cdot\bar{M}\right) \quad (4-2)$$

$$\bar{F} = \bar{G}^F * \bar{M} \quad (4-3)$$

In order to bring all equations together, electric field in terms of scalar and vector potentials are indicated in (4-4).

$$\bar{E} = -j\omega\bar{A} - \nabla\phi \quad (4-4)$$

In (4-5) and (4-6) scalar and the vector potentials are written in terms of induced surface current densities.

$$\bar{A} = \bar{G}^A * \bar{J} \quad (4-5)$$

$$\phi = G_q * \left( -\frac{1}{j\omega} \nabla \cdot \bar{J} \right) \quad (4-6)$$

Reciprocally, electric field and magnetic field can be stated in terms of magnetic vector potential and electrical vector potential as shown in (4-7) and (4-8).

$$\bar{E}(\bar{M}) = \frac{1}{\epsilon} \nabla \times \bar{F} \quad (4-7)$$

$$\bar{H}(\bar{J}) = \frac{1}{\mu} \nabla \times \bar{A} \quad (4-8)$$

A general schematic view of the feed and the antenna is shown in Figure 4.3. The ground plane and the dielectric substrates extend to infinity in both  $x$  and  $y$  directions.

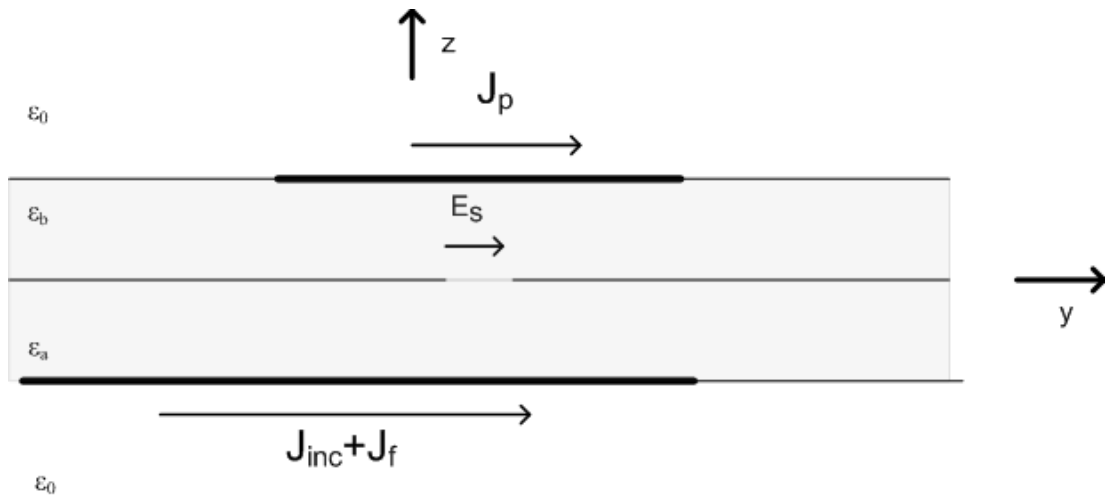


Figure 4.3 Schematic of Electric current on the feed and the antenna

### 4.3 Boundary Conditions

In Figure 4.4, it is shown that, the electric surface currents on the feedline are assumed to be y-directed. On the other hand magnetic surface currents on aperture's both sides are assumed to be x-directed. This is because, both strip and slot widths are very small as compared to the wavelength. Hence, the x-directed current density is assumed to be uniform for feedline and the y-directed current densities is assumed to be uniform for the aperture. However, microstrip patch structure has respectable widths in both sides, which makes x and y-directed current densities change along the structure. In this work, x and y-directed current densities are considered in derivations of the patch.

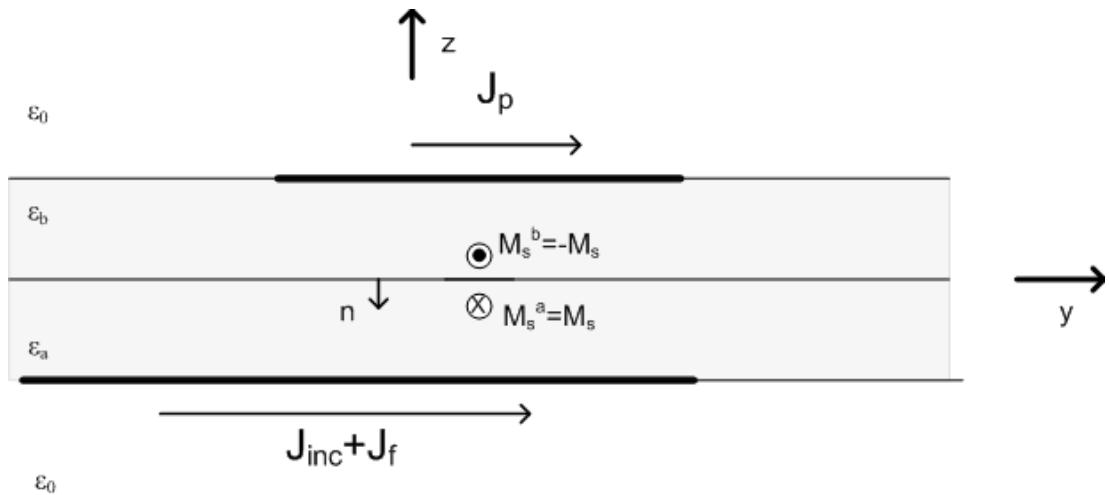


Figure 4.4 General scheme of the boundary electrical and magnetic currents

Firstly, in order to solve the structure and the derive equations, boundary conditions for 3 boundaries are defined. In microstrip fed-slot coupled patch antenna structure, there are 3 boundaries. For these 3 boundaries, 4 boundary equations can be written as;

- I. The y-directed electric field is zero along the microstrip line.
- II. The tangential magnetic field is continuous across the aperture.
- III. The x-directed electric field is zero along the patch.

IV. The y-directed electric field is zero along the patch.

Next, these boundary conditions are written down as equations and all effective current density contributions are considered in the establishment of the boundary condition equations.

### 4.3.1 Feedline Boundary Conditions

On a perfect electric conductor, tangential electric field must vanish along the surface of the material. Since  $x$ -directed electric field is assumed to be uniform along the feedline, only the  $y$ -directed electric field condition on the feedline boundary is regarded. The  $y$ -directed electric field is zero along the microstrip feedline. In (4-9) all effective components of this boundary condition are stated.

$$E_y^{inc} + E_y^a(J_y^f) + E_y^a(M_x) = 0 \quad (4-9)$$

where,  $E_y^{inc}$  is excitation of the feedline,  $E_y^a(J_y^f)$  is the electric field in the region  $a$  due to  $y$ -directed electric current on the feedline, and  $E_y^a(M_x)$  is the electric field contribution in region  $a$  due to  $x$ -directed magnetic current on the aperture. Using (4-4), (4-5) and (4-6),  $E_y^a(J_y^f)$  can be written down as in (4-10).

$$E_y^a(J_y^f) = -j\omega G_{yya}^A * J_y^f + \frac{1}{j\omega} \frac{\partial}{\partial y} \left[ G_q^a * \frac{\partial}{\partial y} J_y \right] \quad (4-10)$$

Similarly, according to (4-9), magnetic currents below the aperture contribute to the electric field as shown in (4-11).

$$E_y^a(M_x) = \frac{1}{\varepsilon} \nabla \times \bar{F} = \frac{1}{\varepsilon} \left( \frac{\partial}{\partial x} F_x - \frac{\partial}{\partial x} F_y \right) \quad (4-11)$$

Since, we are considering only  $x$ -directed currents; our testing functions will be  $x$ -directed either. Hence,  $\frac{\partial}{\partial x} F_y$  contribution brings '0' because it is tested with  $x$ -directed testing function. Then, this leaves us with (4-12).

$$E_y^a(M_x) = \frac{1}{\varepsilon} \left( \frac{\partial}{\partial z} (G_{xx}^F * M_x) \right) \quad (4-12)$$

As a result, if all these contributions are gathered down, total boundary condition equation on the microstrip line is written as in (4-13).

$$E_y^{inc} - j\omega G_{yya}^A * J_y^f + \frac{1}{j\omega} \frac{\partial}{\partial y} \left[ G_q^a * \frac{\partial}{\partial y} J_y^f \right] + \frac{1}{\varepsilon} \left( \frac{\partial}{\partial x} (G_{xxa}^F * M_x) \right) = 0 \quad (4-13)$$

In (4-13) electric and magnetic current functions are the unknowns. Hence,  $J_y^f$  and  $M_x$  can be approximated using a series of known basis functions as shown in (4-14) and (4-15).

$$J_y^f(x, y) = \sum_{n=1}^N I_n J_{yn}^f(x, y) \quad (4-14)$$

where,  $I_n$  's are the unknown coefficients of the basis functions and  $J_{yn}^f(x, y)$  is the basis function for the feedline [43].

Similarly,

$$M_x(x, y) = \sum_{n=1}^N A_n M_x(x, y) \quad (4-15)$$

where,  $A_n$ 's are the unknown coefficients of the basis functions and  $M_x(x, y)$  is the basis function for the aperture magnetic currents. Additionally, on the feedline  $y$ -directed testing functions can be stated as in (4-16).

$$T_y(x, y) = \sum_{n=1}^N T_{ym}(x, y) \quad (4-16)$$

If resulting equation (4-13) is tested with (4-16), boundary condition equation becomes as shown in (4-17) for an arbitrary testing point.

$$\begin{aligned} & E_y^{inc} - j\omega \left\langle T_{ym}, G_{yya}^A * \left( \sum_{n=1}^N I_n J_{yn}^f(x, y) \right) \right\rangle \\ & + \frac{1}{j\omega} \left\langle T_{ym}, \frac{\partial}{\partial y} \left[ G_q^a * \frac{\partial}{\partial y} \left( \sum_{n=1}^N I_n J_{yn}^f(x, y) \right) \right] \right\rangle \\ & + \frac{1}{\varepsilon} \left\langle T_{ym}, \frac{\partial}{\partial x} \left[ G_{xxa}^F * \sum_{n=1}^N A_n M_x(x, y) \right] \right\rangle = 0 \end{aligned} \quad (4-17)$$

Since convolution is a linear operation, (4-17) can be manipulated to (4-18);

$$\begin{aligned} & E_y^{inc} + \sum_{n=1}^N I_n \left\{ -j\omega \left\langle T_{ym}, G_{yya}^A * J_{yn}^f(x, y) \right\rangle \right. \\ & \left. + \frac{1}{j\omega} \left\langle T_{ym}, \frac{\partial}{\partial y} \left[ G_q^a * J_{yn}^f(x, y) \right] \right\rangle \right\} \\ & + \sum_{n=1}^N A_n \left\{ \frac{1}{\varepsilon} \left\langle T_{ym}, \frac{\partial}{\partial z} \left[ G_{xxa}^F * M_x(x, y) \right] \right\rangle \right\} \end{aligned} \quad (4-18)$$

Because, the basis functions in this study are chosen as rooftops which are piecewise differentiable functions, it is possible to use the integration by parts as described in [30] to change order of the integrals. Then (4-18) can be rewritten as:

$$\begin{aligned} & \sum_{n=1}^N I_n \left\{ -j\omega \langle G_{yya}^A, T_{ym} * J_{yn}^f(x, y) \rangle - \frac{1}{j\omega} \left\langle G_q^a, \left[ \frac{\partial}{\partial y} T_{ym} * \frac{\partial}{\partial y} J_{yn}^f(x, y) \right] \right\rangle \right\} \\ & + \sum_{n=1}^N A_n \left\{ \frac{1}{\varepsilon} \left\langle \frac{\partial}{\partial z} G_{xxa}^F, [T_{ym} * M_x(x, y)] \right\rangle \right\} = -E_y^{inc} \end{aligned} \quad (4-19)$$

One of the inner product terms of (4-19) is written in open form as:

$$\langle G_{yya}^A, T_{ym} * J_{yn}^f(x, y) \rangle = \iint dudv G_{yya}^A(u, v) \iint dxdy T_{ym}(x-u, y-v) J_{yn}^f(x, y) \quad (4-20)$$

The double integration of basis and testing functions shown in the above equation represents the convolution of the basis and testing functions which can be carried out analytically. The details of the calculations of these convolution integrals are described in Appendix A. Then, (4-20) can be solved just by double integration. In this study, since Galerkin's Method of Moments is used, the basis functions and testing functions are chosen to be the same.

### 4.3.2 Aperture Boundary Conditions

Across the slot tangential magnetic field is continuous, that is to say, the tangential magnetic field in the aperture's lower side is equal to the tangential magnetic field in the upper side. Since, it is assumed that only x-directed magnetic current exists across the aperture, boundary condition equation can be stated as in (4-21).

$$H_x^a(J_y^f) + H_x^a(M_x) = H_x^b(-M_x) + H_x^b(J_y^p) + H_x^b(J_x^f) \quad (4-21)$$

Where,  $H_x^a(J_y^f)$  is the magnetic field due to electric currents on the feedline,  $H_x^a(M_x)$  is the magnetic field due to magnetic currents in the lower side of the slot.

These two components make the total tangential magnetic field below the slot. Above the slot,  $H_x^b(-M_x)$  is the magnetic field due to the magnetic current,  $H_x^b(J_y^p)$  is the magnetic field due to  $y$ -directed currents on the patch and  $H_x^b(J_x^f)$  is the magnetic field contribution due to the  $x$ -directed currents on the patch.

Next, all components of the slot boundary condition equality are written down. By using (4-8)  $H_x^a(J_y^f)$  can be defined as in (4-22).

$$H_x^a(J_y^f) = \frac{1}{\mu} (\bar{\nabla} \times \bar{A}) \quad (4-22)$$

If electrical vector potential is located into (4-22) and necessary calculations are carried out, equation turns to (4-23) .

$$H_x^a = \frac{1}{\mu} \left( a_x \frac{\partial}{\partial y} A_z - a_x \frac{\partial}{\partial z} A_y \right) \quad (4-23)$$

Next,  $A_z$  and  $A_y$  are replaced with the Green's function definitions by using (4-24) and (4-25).

$$A_z = G_{zya}^A * J_y^f \quad (4-24)$$

$$A_y = G_{yya}^A * J_y^f \quad (4-25)$$

Then, (4-25) is transformed into (4-26).

$$H_x^a(J_y^f) = \frac{1}{\mu} \left( \frac{\partial}{\partial y} (G_{zya}^A * J_y^f) - \frac{\partial}{\partial z} (G_{yya}^A * J_y^f) \right) \quad (4-26)$$

Because, this study is dealing with x directed currents on the slot, only x-directed testing functions are used. As a result first term in (4-26) vanishes. Considering that (4-26) can be rewritten as:

$$H_x^a(J_y^f) = \frac{1}{\mu} \left( -\frac{\partial}{\partial z} (G_{yya}^A * J_y^f) \right) \quad (4-27)$$

Having completed feedline contribution to the total magnetic field, magnetic currents which are located on the slot boundaries contribution to the magnetic field can be formulized. By using (4-1), (4-2) and (4-3),  $H_x^a(M_x)$  can be written as in (4-28).

$$H_x^a(M_x) = -j\omega \bar{F} - \nabla \left( G^{qm} * \frac{-1}{j\omega} \nabla \cdot M_x \right) \quad (4-28)$$

However, (4-28) can be rewritten, using magnetic vector and scalar potential functions.

$$H_x^a(M_x) = -j\omega G_{xxa}^F * M_x + \left( \frac{1}{j\omega} \frac{\partial}{\partial x} \left( G_q^a * \frac{\partial}{\partial x} M_x \right) \right) \quad (4-29)$$

Similarly, for the upper side of the slot magnetic current contribution to the magnetic field can be written as in (4-30).

$$H_x^b(M_x) = j\omega G_{xxb}^F * M_x - \left( \frac{1}{j\omega} \frac{\partial}{\partial x} \left( G_q^b * \frac{\partial}{\partial x} M_x \right) \right) \quad (4-30)$$

In upper side of the slot, there is also a magnetic field contribution from the induced currents on the patch. Firstly, the y-directed electric currents on the patch creates magnetic field component  $H_x^b(J_y^p)$  of (4-21) just like (4-27).

$$H_x^b(J_y^p) = \frac{1}{\mu} \left( -\frac{\partial}{\partial z} (G_{yyb}^A * J_y^p) \right) \quad (4-31)$$

Finally, x-directed currents are considered as contributors of the magnetic field in the upper side of the slot. However, since x-directed electric currents cannot create x-directed magnetic field, this contribution come out to be null. All derived quantities are gathered, and final boundary condition equation is written down:

$$\begin{aligned} & -\frac{1}{\mu} \frac{\partial}{\partial z} G_{yya}^A * J_y^f - j\omega G_{yya}^F * M_x + \frac{1}{j\omega} \frac{\partial}{\partial x} \left( G_q^a * \frac{\partial}{\partial x} M_x \right) \\ & = j\omega G_{xxb}^F * M_x - \frac{1}{j\omega} \frac{\partial}{\partial x} \left( G_q^b * \frac{\partial}{\partial x} M_x \right) - \frac{1}{\mu} \frac{\partial}{\partial z} G_{yyb}^A * J_y^p \end{aligned} \quad (4-32)$$

Then vector Green's functions and the scalar Green's functions are brought either sides of the equation.

$$\begin{aligned} & j\omega (G_{xxb}^F + G_{xxa}^F) * M_x - \frac{1}{j\omega} \frac{\partial}{\partial x} (G_q^a + G_q^b) * \frac{\partial}{\partial x} M_x \\ & - \frac{1}{\mu} \frac{\partial}{\partial z} G_{yyb}^A * J_y^p + \frac{1}{\mu} \frac{\partial}{\partial z} G_{yya}^A * J_y^f = 0 \end{aligned} \quad (4-33)$$

After that, the electric and magnetic current functions are replaced by the basis functions. Also they are tested with the testing function which yields the equation shown in (4-34). At the same step, change of order of the integrals is done using the same rules applied in (4-19).

$$\begin{aligned}
& \sum_{n=1}^N A_{xn} \left\{ j\omega \left\langle G_{xxb}^F + G_{xxa}^F, T_{xm} * M_x(x, y) \right\rangle + \frac{1}{j\omega} \left\langle G_q^a + G_q^b, \frac{\partial}{\partial x} T_{xm} * \frac{\partial}{\partial x} M_x \right\rangle \right\} \\
& \sum_{n=1}^N I_{xn}^p \left\{ -\frac{1}{\mu} \left\langle \frac{\partial}{\partial z} G_{yyb}^A, T_x * J_y^p \right\rangle \right\} + \sum_{n=1}^N I_{xn} \left\{ \frac{1}{\mu} \left\langle \frac{\partial}{\partial z} G_{yya}^A, T_x * J_y^f \right\rangle \right\} = 0
\end{aligned} \tag{4-34}$$

### 4.3.3 Patch Boundary Conditions

Patch is the radiating element of the microstrip fed-slot coupled patch antenna and is made of perfect electric conductor. Hence, the tangential electric field is zero on the patch surface. Being different from the feedline and the slot it has two dimensional electric surface currents in both sides. Since it has respectable width parameter for both x and y dimensions, surface currents of neither x-directed nor y-directed can be neglected. Because of that, boundary conditions can be separated and analyzed in set of two equations.

#### 4.3.3.1 Y-directed Patch Surface Field Equations

Along the patch, the y-directed electric field is zero (4-35). In the structure, there are 2 known induced current sources that are known to create y-directed electric field. They are, x-directed magnetic current elements on the upper side of the patch, and y-directed electric current elements on the patch itself (4-36).

$$E_y^p = 0 \tag{4-35}$$

$$E_y^p = E_y(J_y^p) - E_y(M_x) \tag{4-36}$$

In (4-36), the term  $E_y(J_y^p)$ , is the y-directed electric field component due to electric currents induced on the patch. It can be written in terms of vector and scalar dyadic Green's functions using (4-4), (4-5) and (4-6).

$$E_y(J_y^p) = -j\omega\bar{A} - \nabla \left( G^q * \frac{-1}{j\omega} \nabla \cdot J^p \right) \quad (4-37)$$

$$E_y(J_y^p) = -j\omega G_{yyb}^A * J_y^p + \frac{1}{j\omega} \nabla \left( G_b^q * \nabla \cdot J^p \right) \quad (4-38)$$

If the term  $J^p$  is replaced with the surface current vector, the field equations become as shown in (4-39):

$$E_y(J_y^p) = -j\omega G_{yyb}^A * J_y^p + \frac{1}{j\omega} \frac{\partial}{\partial y} \left( G_b^q * \frac{\partial}{\partial x} J_x^p + G_b^q * \frac{\partial}{\partial y} J_y^p \right) \quad (4-39)$$

The term,  $E_y(M_x)$  in (4-35) is the y-directed electric field component due to magnetic currents induced on the upper side of the slot. It can be written in terms of vector and scalar dyadic Green's functions in (4-40) just as the same as (4-12).

$$E_y(M_x) = \frac{1}{\varepsilon} \left( \frac{\partial}{\partial z} (G_{xxb}^F \times M_x) \right) \quad (4-40)$$

In order to enhance (4-36), (4-39) and (4-40) are inserted into their locations in the equation yielding:

$$\begin{aligned} & -j\omega(G_{yyb}^A * J_y^p) + \frac{1}{j\omega} \frac{\partial}{\partial y} \left( G_b^q * \frac{\partial}{\partial y} J_y^p \right) + \frac{1}{j\omega} \frac{\partial}{\partial y} \left( G_b^q * \frac{\partial}{\partial x} J_x^p \right) \\ & - \frac{1}{\varepsilon} \left( \frac{\partial}{\partial z} (G_{xxa}^F * M_x) \right) = 0 \end{aligned} \quad (4-41)$$

Then, electric and magnetic current functions are replaced by the basis functions. Resulting function is tested with the testing functions which yield the equation

shown in (4-42). At the same step, change of order of the integrals is done using the same rules applied in (4-19).

$$\begin{aligned} & \sum_{n=1}^N I_{yn}^p \left\{ -j\omega \left\langle G_{yjb}^A, T_{ym} * J_y^p(x, y) \right\rangle - \frac{1}{j\omega} \left\langle G_b^q, \frac{\partial}{\partial y} T_{ym} * \frac{\partial}{\partial y} J_y^p(x, y) \right\rangle \right. \\ & \left. - \frac{1}{j\omega} \left\langle G_b^q, \frac{\partial}{\partial y} T_{ym} * \frac{\partial}{\partial x} J_x^p(x, y) \right\rangle \right\} + \sum_{n=1}^N A_{zn} \left\{ -\frac{1}{\varepsilon} \left\langle \frac{\partial}{\partial z} G_{xzb}^F, T_{ym} * M_x(x, y) \right\rangle \right\} = 0 \end{aligned} \quad (4-42)$$

### 4.3.3.2 X-directed Patch Surface Field Equations

Along the patch, the x-directed electric field equals to zero (4-43). In the structure, there is only one known induced current source that is known to create x-directed electric field. This is the x- electric current elements on the patch itself (4-44).

$$E_x^p = 0 \quad (4-43)$$

$$E_x^p = E_x(J^p) \quad (4-44)$$

In (4-44), the term  $E_x(J^p)$  is the x-directed electric field component due to electric currents induced on the patch. It can be written in terms of vector and scalar dyadic Green's functions using (4-4), (4-5) and (4-6).

$$E_x(J^p) = -j\omega \bar{A} - \nabla \left( G^q * \frac{-1}{j\omega} \nabla \cdot J^p \right) \quad (4-45)$$

$$E_x(J^p) = -j\omega G_{xzb}^A * J_x^p + \frac{1}{j\omega} \nabla \left( G_b^q * \nabla \cdot J^p \right) \quad (4-46)$$

If the term  $J^p$  is replaced with the surface current vector, the field equations return to (4-47).

$$E_x(J^p) = -j\omega G_{xxb}^A * J_y^p + \frac{1}{j\omega} \frac{\partial}{\partial x} \left( G_b^q * \frac{\partial}{\partial x} J_x^p + G_b^q * \frac{\partial}{\partial y} J_y^p \right) \quad (4-47)$$

Then, electric and magnetic current functions are replaced by the basis functions. Resulting equation is tested with the testing function which yields the equation shown in (4-48). At the same step, change of the order of the integrals is done using the same rules applied in (4-19).

$$\sum_{n=1}^N I_{xn}^p \left\{ -j\omega \left\langle G_{xxb}^A, T_{xm} * J_y^p(x,y) \right\rangle - \frac{1}{j\omega} \left\langle G_b^q, \frac{\partial}{\partial x} T_{xm} * \frac{\partial}{\partial x} J_x^p(x,y) \right\rangle - \frac{1}{j\omega} \left\langle G_b^q, \frac{\partial}{\partial x} T_{xm} * \frac{\partial}{\partial y} J_y^p(x,y) \right\rangle \right\} = 0 \quad (4-48)$$

In this study, Galerkin's Method of Moments is used. Hence the basis and testing functions are chosen to be same. In the following sections of this chapter, the exact representations of the basis functions and testing functions will be detailed.

#### **4.4 Test and Basis Functions**

Basis and testing functions are chosen to be identical and as rooftops. These functions are triangular in longitudinal direction and uniform in transverse direction. The rooftop basis functions are shown in Figure 4.5. As an example, the mathematical representation of the feedline rooftop basis functions is given in (2-49) [4]:

$$J_{xn}(x, y) = \left\{ \begin{array}{ll} \frac{1}{\omega h_x} [(1-n)h_x + x] & (n-1)h_x \leq x \leq nh_x, |y| \leq \frac{W}{2} \\ \frac{1}{\omega h_x} [(1+n)h_x - x] & nh_x \leq x \leq (n+1)h_x, |y| \leq \frac{W}{2} \\ 0 & \text{otherwise} \end{array} \right\} \quad (4-49)$$

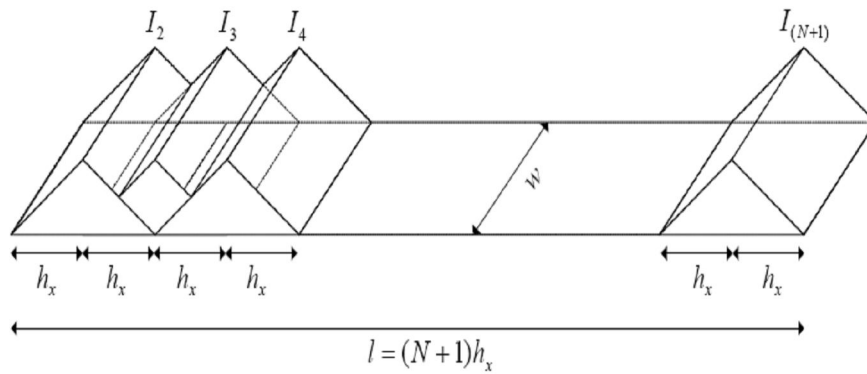


Figure 4.5 Rooftop Basis and Testing Functions [3]

#### 4.5 MoM Matrices and the Number of Unknowns

In applying moments method, selecting the number of unknowns is an important step. Discretization of the calculation domain determines the number of unknowns. In this study, microstrip feedline and slot are assumed to have current distributions varying only in one dimension. For that reason, they are both discretized along only one dimension. On the other hand, microstrip path have two-dimensionally varying current distribution. For most of the simulations of this study, 19 point discretization of the domain is applied. Hence, patch is dissected into 19x19 sub-domains. Hence, for a microstrip fed-slot coupled patch antenna, total number of sub-domains becomes 361. There are 4 equations for 4 groups of unknowns:

y-directed electric current coefficients on the feed = 19;

$x$ -directed magnetic current coefficients on the aperture = 19;

$y$ -directed electric current coefficients on the patch = 361;

$x$ -directed electric current coefficients on the patch = 361;

Total number of unknown coefficients=760;

This discretization of the domain with a general type MoM equation,  $Ax = b$  results;

Size of the A matrix=760x760;

Size of the unknown vector  $x$ =760x1;

Size of the unknown vector  $b$ =760x1;

## **4-6 Results**

In this section, results of the MoM analysis of the microstrip fed-slot coupled patch antenna will be presented in comparison with the calculations and measurements of [2]. Electric current distribution along the feedline and the patch will be calculated. Then reflection coefficient parameter of the antenna in analyzed frequencies will be presented.

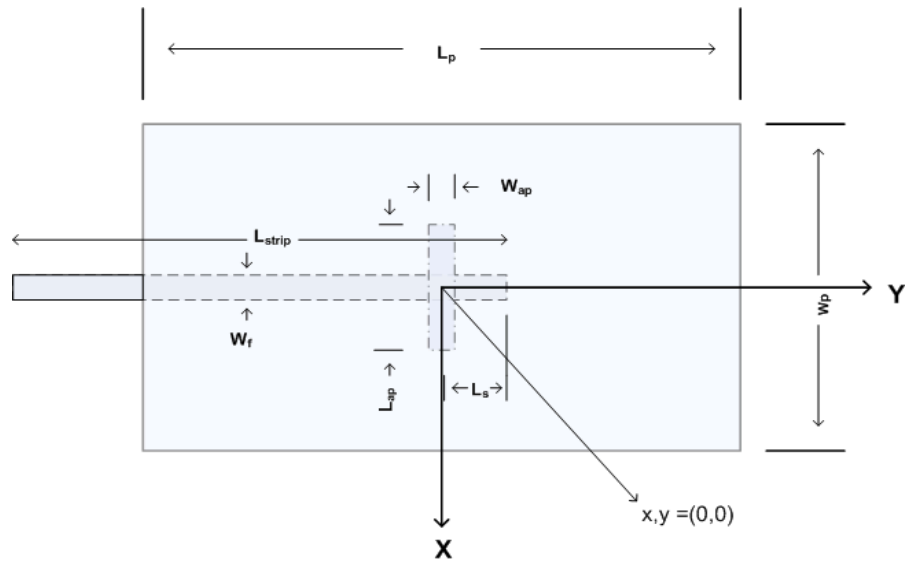


Figure 4.6 Parametric geometry of the microstrip fed-slot coupled patch antenna

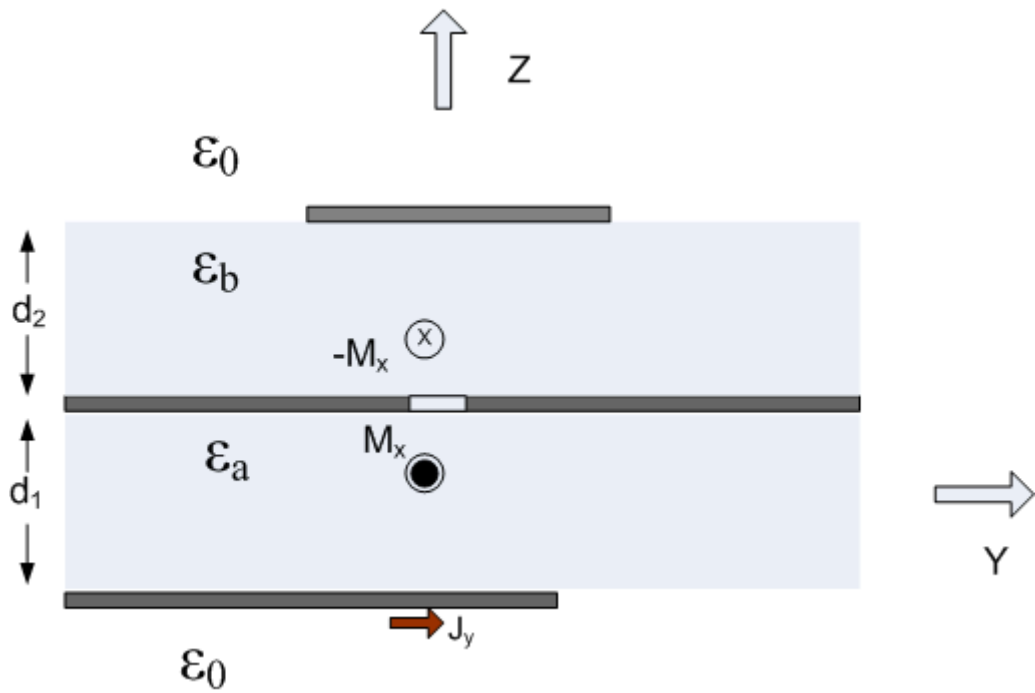


Figure 4.7 Parametric geometry of the microstrip fed-slot coupled patch antenna (sideview)

In Figure 4.7,  $\epsilon_a$  is relative permittivity constant below the aperture,  $\epsilon_b$  is relative permittivity constant above the aperture,  $d_1$  is the thickness of the substrate below the aperture and  $d_2$  is the thickness of the substrate above the aperture.

The design parameters for the given design based on Figure 4.6 and Figure 4.7 are given as:

$$f = 2.12 \text{ GHz}$$

$$\epsilon_a = 2.55$$

$$\epsilon_b = 2.55$$

$$L_p = 4 \text{ cm}$$

$$w_p = 3 \text{ cm}$$

$$L_{strip} = 7 \text{ cm}$$

$$W_f = 0.47 \text{ cm}$$

$$W_{ap} = 0.155 \text{ cm}$$

$$L_{ap} = 1.4 \text{ cm}$$

$$L_s = 1.2 \text{ cm}$$

$$d_a = 0.16 \text{ cm}$$

$$d_b = 0.16 \text{ cm}$$

where,  $d_a$  is the thickness of the substrate below the aperture and  $d_b$  is the thickness of the substrate above the aperture.

These are the parameters which Pozar suggested in his work [1] and repeated here for comparison purposes. By using these parameters, it is assured that slot is at the center of the patch, which enables the maximum coupling from feedline to the patch through the aperture.

As a result of MoM simulation, electric current distribution is calculated. In Figure 4.8 electric surface current on the feedline is shown as a result of our MoM code and HFSS<sup>®</sup> together. Both results are extracted from simulations done at 2.14GHz.

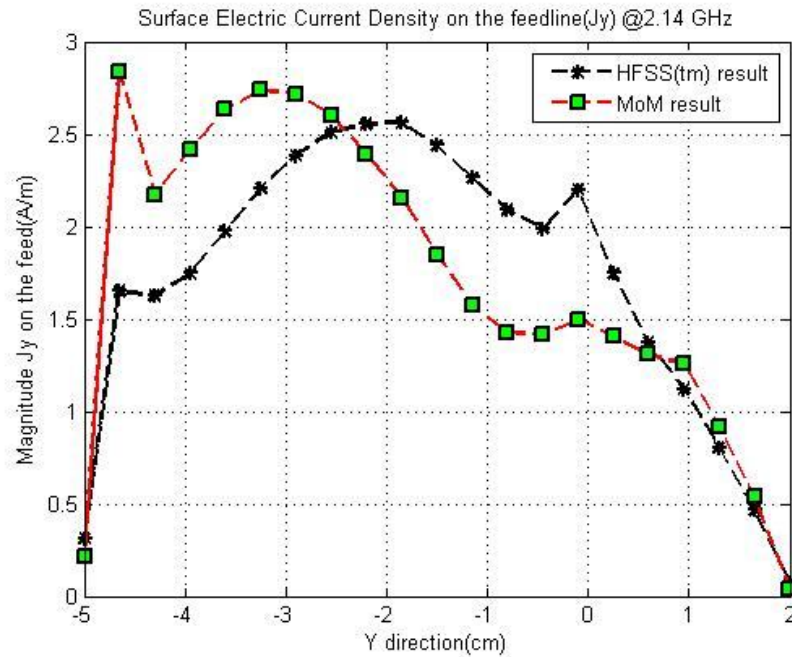


**Figure 4.8 Electric current distribution along the feedline**

According to the current distribution result, it can be said that reflection coefficients of the two analyses resemble in magnitudes. However, their phases have some differences. This is because HFSS<sup>®</sup> , uses exact model boundaries creating reflections, which is the reason of phase changes. However, in our study all layers are assumed to extend to infinity in transverse directions.

Then using Prony’s method [42] which is explained in Appendix B, reflection coefficient parameter is found. The current distribution function on the feedline is represented as in (4-50).

$$I(x) \cong c_1 e^{-\beta_1 x} + c_2 e^{\beta_2 x} \quad (4-50)$$

The related parameters are found as a result of Prony analysis are:

$$c_1 = -1.9993 + 0.8014j$$

$$c_2 = 0.5217 - 0.1033j$$

$$\beta_1 = -1.2435 - 64.5529j$$

$$\beta_2 = -4.8460 + 68.5593i$$

Reflection coefficient parameter can be calculated using these constants ( $\Gamma = \frac{c_2}{c_1}$ ).

The ratio  $\frac{c_2}{c_1}$  gives S11 which is depicted in Figure 4.9 for different frequencies. On the other hand Pozar's results are also shown for the same frequencies.

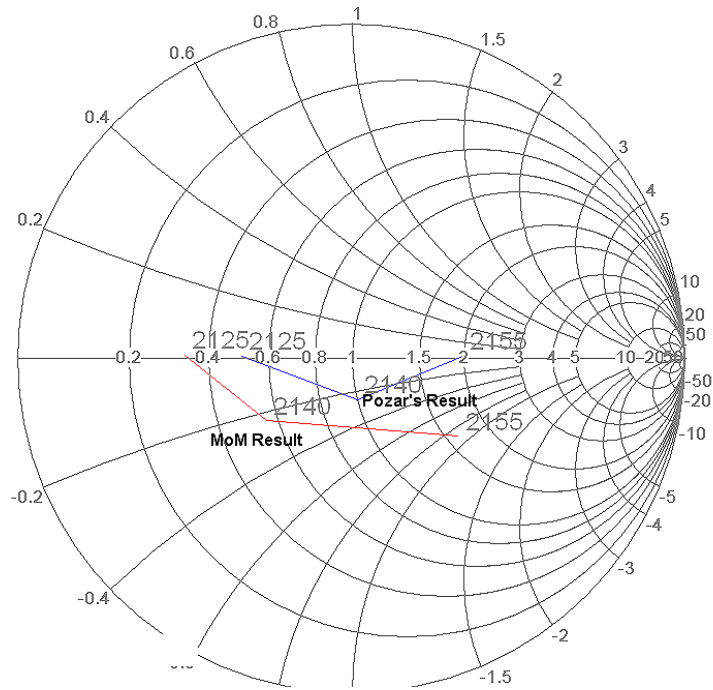


**Figure 4.9** Comparative demonstration of input impedance from MoM and Pozar's results

Through the aperture, electromagnetic energy coupled to the microstrip patch. Induced y-directed electric surface current distributions for different x-locations are given in Figure 4.10 and Figure 4.11.

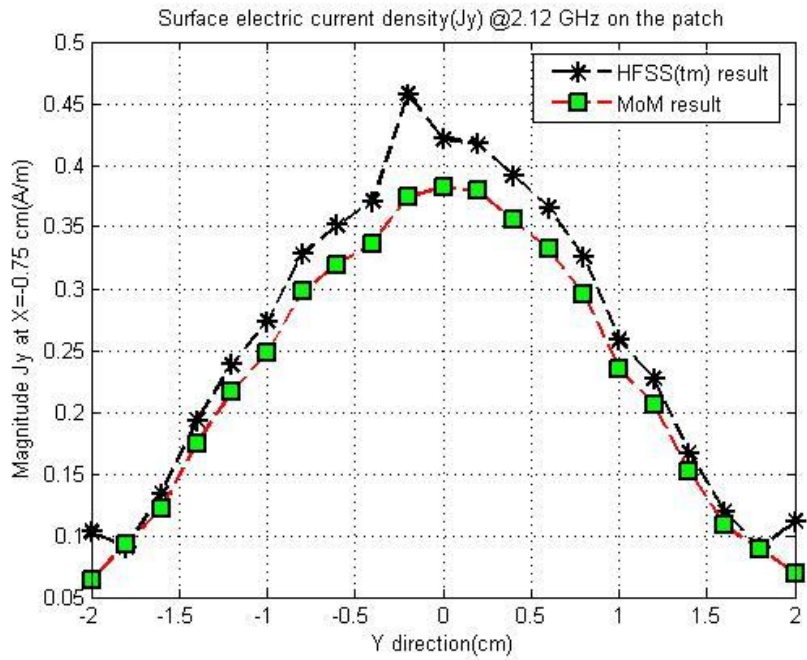


Figure 4.10 Y-directed electric current distribution along the patch y-direction at X=-0.75 cm

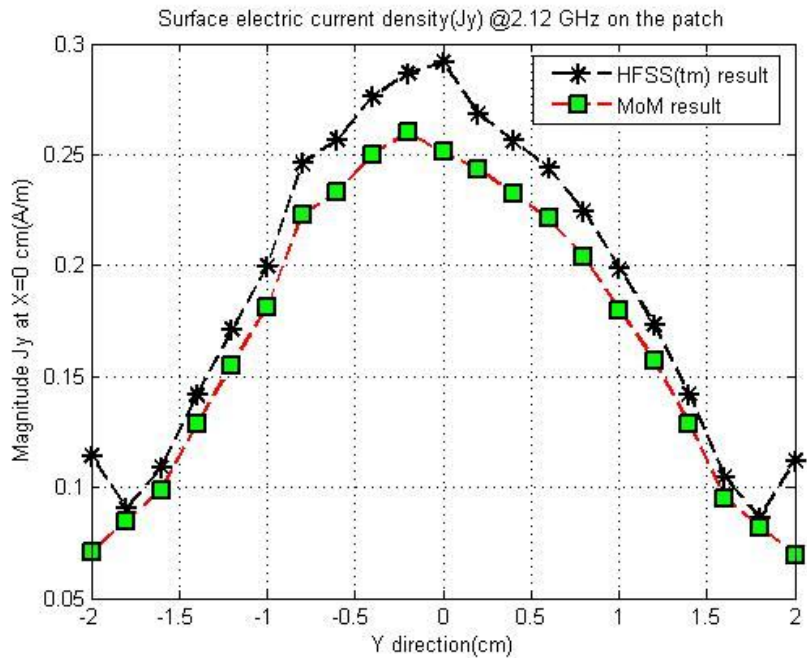
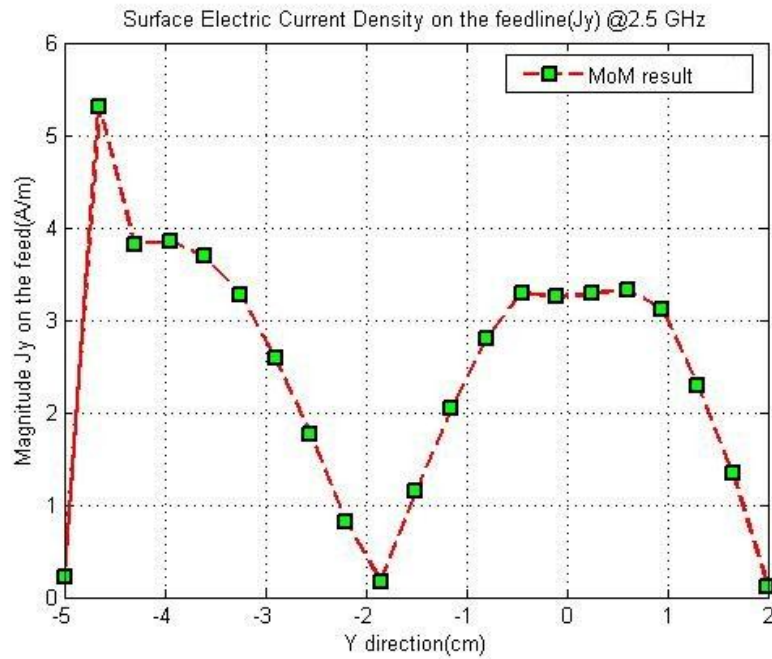


Figure 4.11 Y-directed electric current distribution along the patch y-direction at X=0 cm

Slot coupled patch structure has a resonant frequency very close to 2.14 GHz. For the sake of getting other frequency solutions, MoM code is run with 2.5 GHz parameters. By looking at the initial solutions, it is expected that S11 would be very close to 0 dB at 2.5 GHz. Feedline current distribution solutions are shown in Figure 4.12.



**Figure 4.12 Electric current distribution along the feedline at 2.5 GHz**

By using the electric current distribution on the feedline and Prony’s method we get coefficients of incident and reflected currents,  $c_1$  and  $c_2$  as depicted in (4-50). These incident and reflected wave coefficients yield a S11 value very close to 0.

For the sake of completion and the comparison with the resonance frequency, patch current distribution characteristics are given for 2.5 GHz.

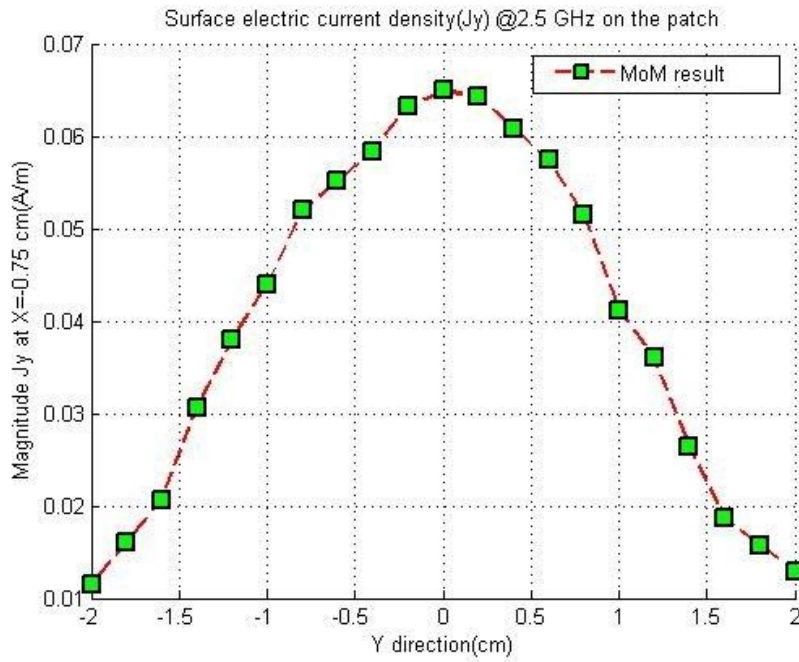


Figure 4.13 Y-directed electric current distribution along the patch y-direction at X=-0.75 cm

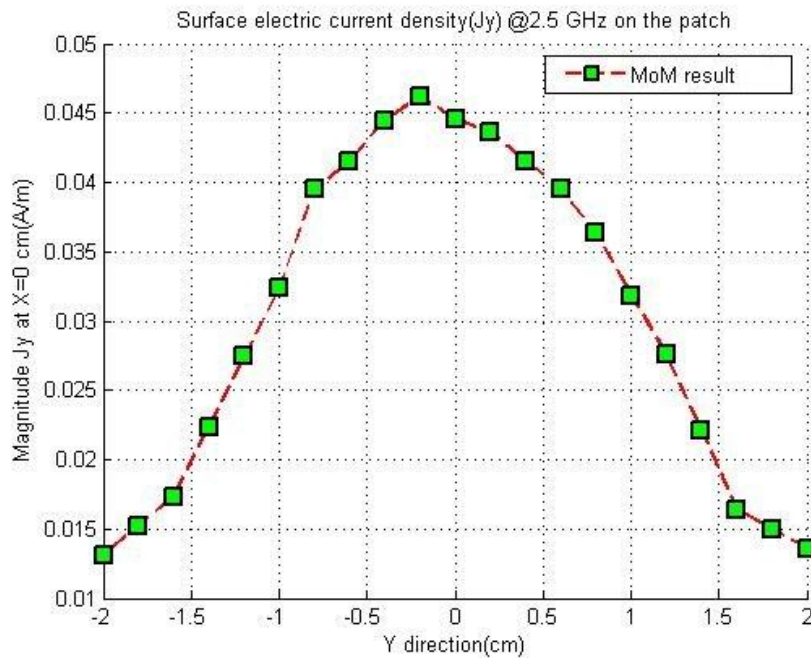


Figure 4.14 Y-directed electric current distribution along the patch y-direction at X=0 cm

By examining the current distribution results, it can be said that our approach yields very reasonable outputs. Comparisons between HFFS<sup>®</sup>, Pozar's studies and our work verifies each other. However, all results deviate from each other in some manner. This is because all approaches use different approximations and medium characteristics. MoM analysis using closed form Green's functions assumes the substrate layers extend to infinity in transverse directions. Also, in this study surface waves are assumed to be ignorable. On the other hand, Pozar uses a different model in the solutions of this kind of antenna geometries. Similarly, HFFS<sup>®</sup> outputs may be somehow different, because it solves the bounded geometry. Boundary definitions of the software and sizes can change the solution.

## CHAPTER 5

### PARAMETRIC ANALYSIS OF THE MICROSTRIP FED-SLOT COUPLED PATCH ANTENNA

Having completed the analysis of a generic well-defined microstrip fed-slot coupled patch antenna, our work of MoM analysis approach is considered to be verified. Then, this study continues with the parametric analysis of the structure with different parameters such as stub length, slot length, slot width, and slot location etc. In designing this kind of a patch antenna, there are two degrees of freedom for tuning [1]. These are the aperture length ( $L_{ap}$ ) and the stub length ( $L_s$ ) shown in Figure 5.1. Besides, slot width and the slot location affect the antenna performance by increasing or decreasing the coupled field from feedline to patch. In this work parametric analysis is done by changing slot location, stub length and slot length, while slot width is held fixed. For all above mentioned parametric analysis will be carried out with our MoM code and will be compared with HFSS® and also with [5].

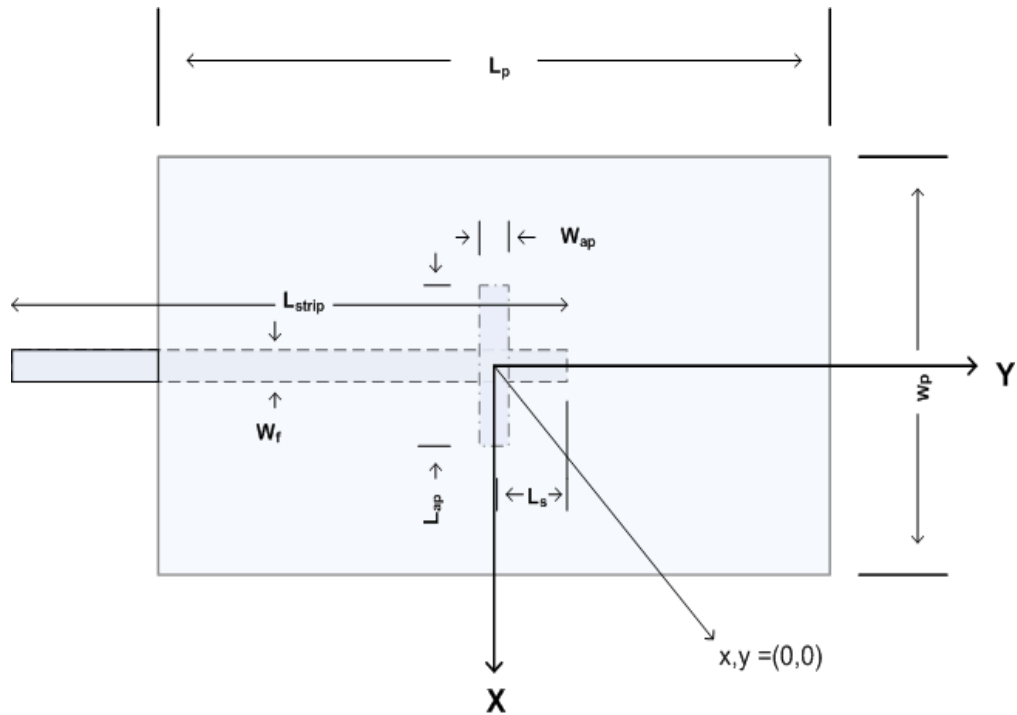


Figure 5.1 Parametric geometry of a microstrip fed-slot coupled patch antenna

### 5.1 Analysis of a Base Structure

First of all, before continuing with the parametric analysis, it will be a good verification method to built a base structure and compare it with a study from the literature. The parameters of our base structure are as below:

#### Model 1:

This model is structured and analyzed with the parameters:

$$f = 2.17 \text{ GHz}$$

$$\varepsilon_a = 2.55$$

$$\varepsilon_b = 2.55$$

$$L_p = 4 \text{ cm}$$

$$w_p = 3 \text{ cm}$$

$$L_{strip} = 7 \text{ cm}$$

$$W_f = 0.495 \text{ cm}$$

$$W_{ap} = 0.11 \text{ cm}$$

$$L_{ap} = 1.4 \text{ cm}$$

$$L_s = 2 \text{ cm}$$

$$d_a = 0.16 \text{ cm}$$

$$d_b = 0.16 \text{ cm}$$

where,  $\epsilon_a$  is relative permittivity constant below the aperture,  $\epsilon_b$  is relative permittivity constant above the aperture,  $d_a$  is the thickness of the substrate below the aperture and  $d_b$  is the thickness of the substrate above the aperture.

With these parameters, moment method yields the current distribution at different frequencies which are shown in Figure 5.2, Figure 5.3 and Figure 5.4.

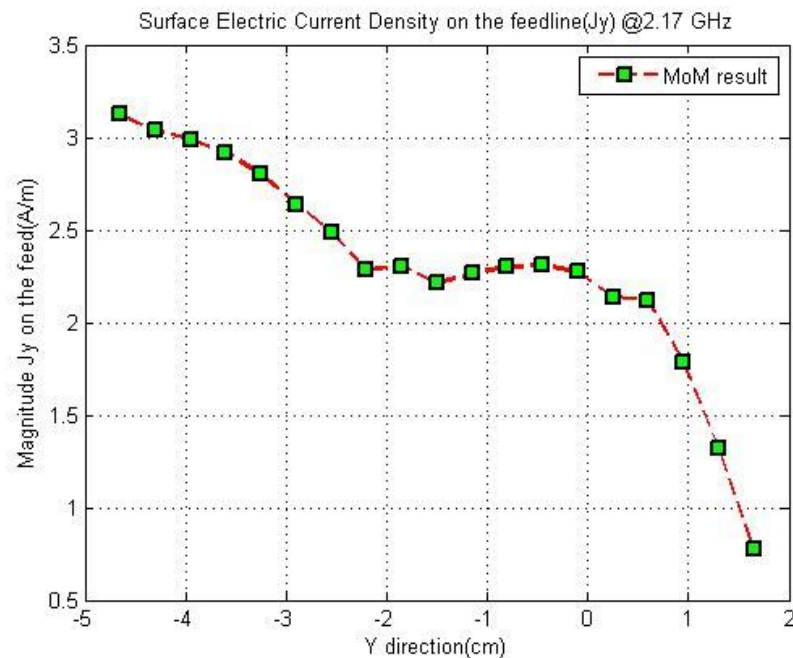


**Figure 5.2** Surface electric current distribution on the microstrip feedline at 2.17 GHz.

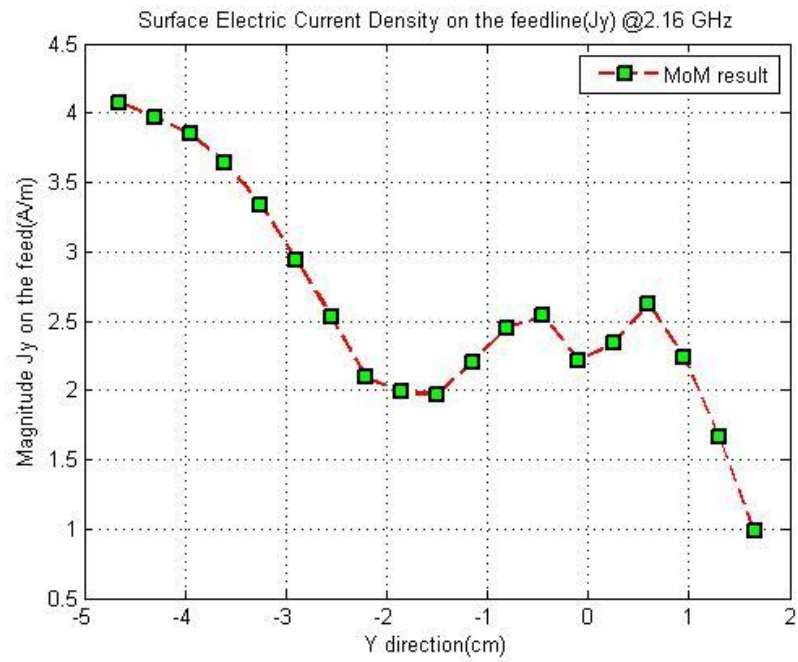


Figure 5.3 Surface electric current distribution on the microstrip feedline at 2.16 GHz.

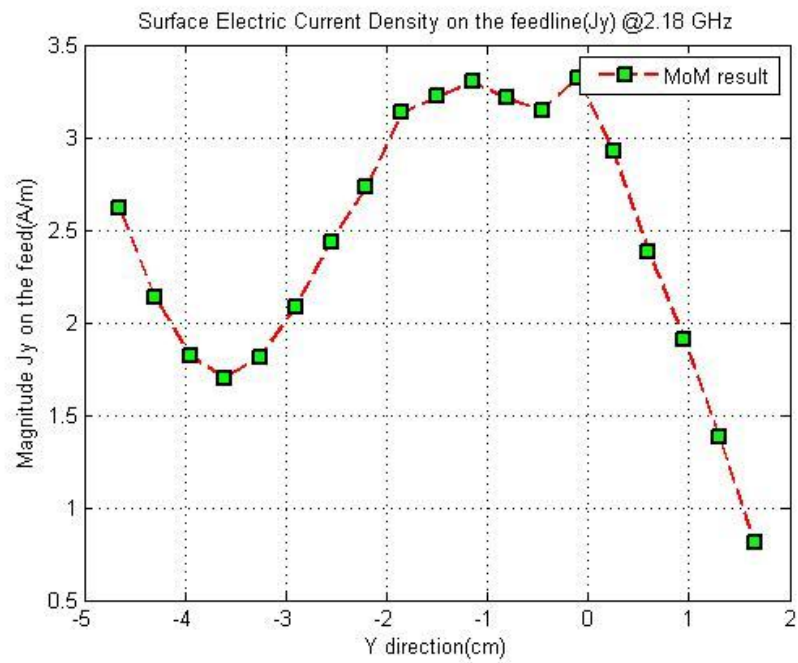


Figure 5.4 Surface electric current distribution on the microstrip feedline at 2.18 GHz.

According to the current distribution result at the resonance frequency of 2.17 GHz, it can be said that reflection coefficient of the analysis come out to be very small. Using Prony's method for resulting current distribution of the MoM analysis, reflection coefficient value of the antenna at different frequencies is found. The related parameters given in (4-50) at 2.17 GHz are calculated to be;

$$c_1 = 2.2011 - 1.5165j$$

$$c_2 = 0.2813 - 0.3110i$$

$$\beta_1 = -3.2587 - 60.6704i$$

$$\beta_2 = -17.0243 + 65.8384i$$

That result is given comparatively with the Schaubert's study [5] in Figure 5.5. According to that comparison, our result yields smaller reflection coefficient than Schaubert's study. This may be due to difference of approximation schemes. On the other hand, both results give minimum reflection coefficient at 2.17 GHz.

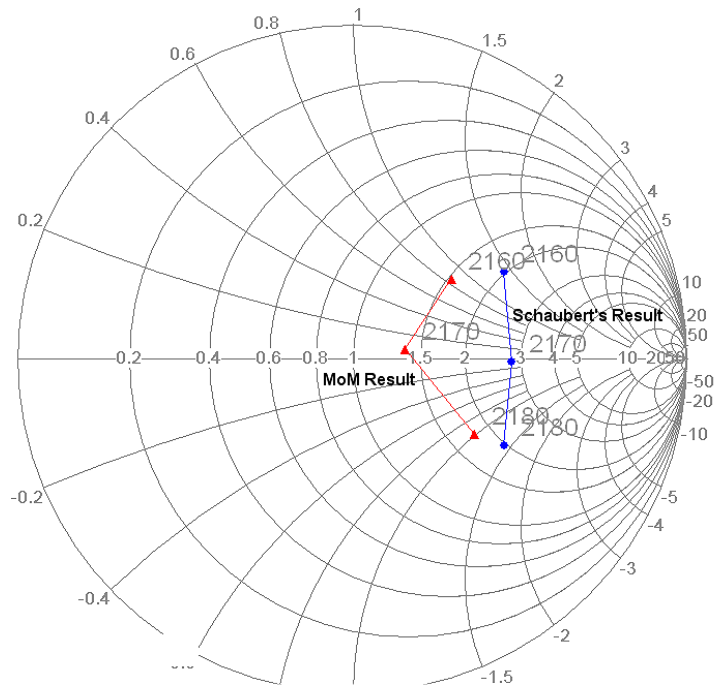


**Figure 5.5 Comparative demonstration of input impedance of MoM and Schaubert's results [5]**

After that, *y*-directed electric current distributions on the patch are demonstrated for several *x*-coordinates comparatively.

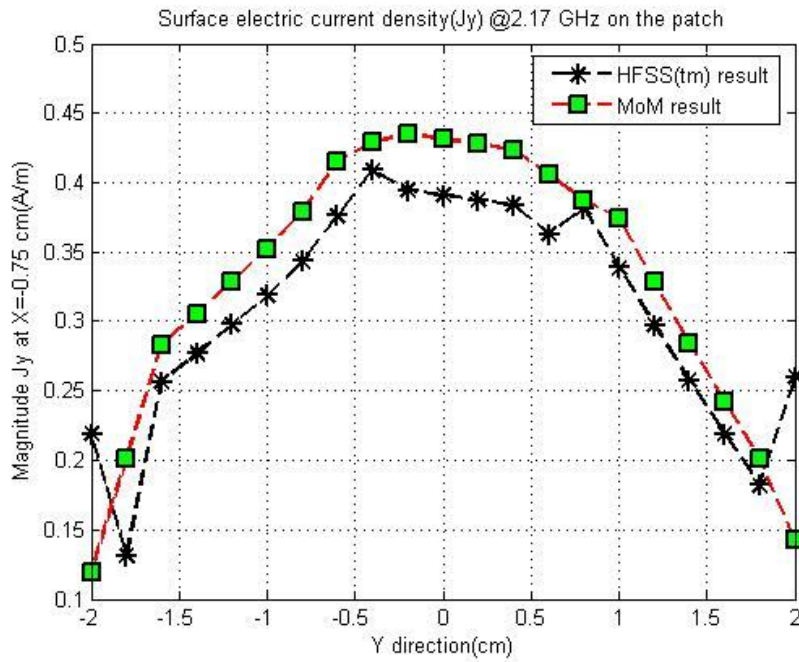


Figure 5.6 Surface electric current distribution on the microstrip patch at 2.2 GHz at  $x=-0.75$  cm

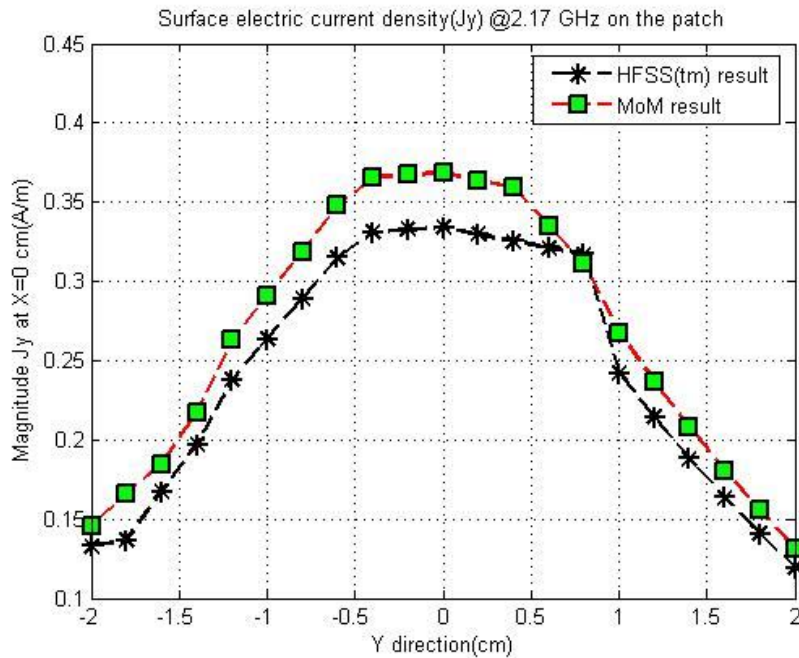


Figure 5.7 Surface electric current distribution on the microstrip patch at 2.2 GHz at  $x=0$  cm

By looking at these results, it can be said that our approach gives similar results to Schaubert's study [5]. On the other hand comparative analysis of current distributions on the strip and on the patch demonstrates the difference of the two approaches. By looking at the phase of the reflection coefficients they are very close as seen in Figure 5.5 . However, magnitudes of the two results make the difference between solutions seen on the Smith Chart. As it is seen in Figure 5.4 and in Figure 5.5 there is a magnitude difference between different approaches. This may be due to Schaubert's [5] use of different approach, whereas we are using MoM in conjunction with closed form Green's functions.

## **5.2 Analysis of Slot Length Effects to the Antenna**

### **Performance**

In this section, antenna performance with respect to the slot length changes is questioned. In order to do that, 3-different models are created, current distributions and reflection coefficient values are demonstrated comparatively with different sources.

#### **5.2.1 Slot Length is 1.2 cm**

##### **Model 2:**

This model is structured and analyzed with the parameters:

$$f = 2.21 \text{ GHz}$$

$$\varepsilon_a = 2.55$$

$$\varepsilon_b = 2.55$$

$$L_p = 4 \text{ cm}$$

$$w_p = 3 \text{ cm}$$

$$L_{strip} = 7 \text{ cm}$$

$$W_f = 0.495 \text{ cm}$$

$$W_{ap} = 0.11 \text{ cm}$$

$$L_{ap} = 1.2 \text{ cm}$$

$$L_s = 2 \text{ cm}$$

$$d_a = 0.16 \text{ cm}$$

$$d_b = 0.16 \text{ cm}$$

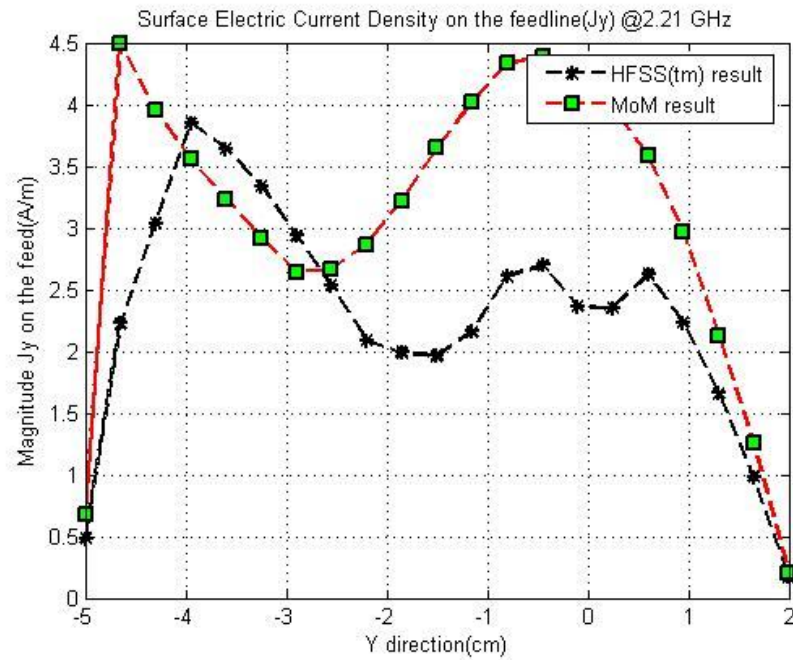


**Figure 5.8** Surface electric current distribution on the microstrip feedline at 2.21 GHz.

According to the current distribution result, it can be said that reflection coefficients of the two analyses resemble in magnitudes. However, their phases have some differences. In Figure 5.9 and Figure 5.10 current distribution results of the frequencies 2.2 GHz and 2.22 GHz are shown respectively.

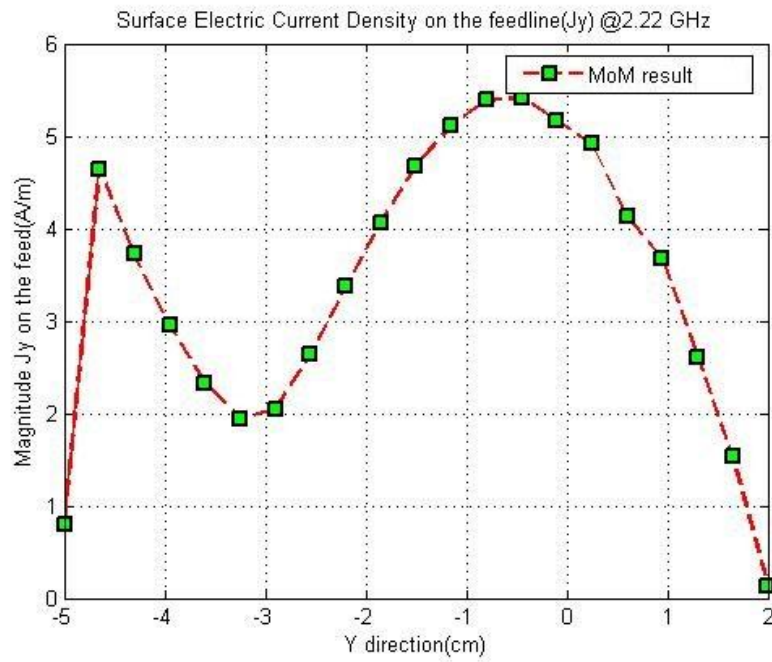


Figure 5.9 Surface electric current distribution on the microstrip feedline at 2.2 GHz.

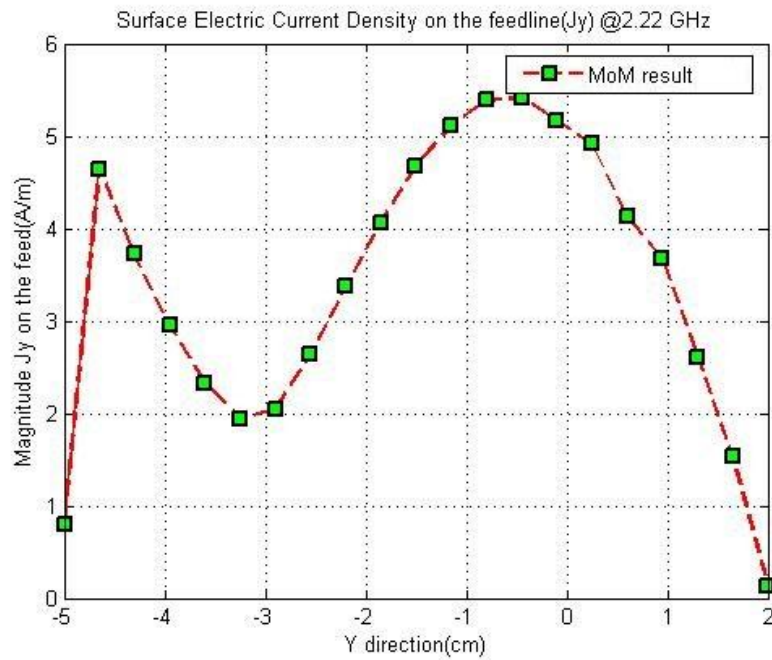


Figure 5.10 Surface electric current distribution on the microstrip feedline at 2.22 GHz.

By using Prony's method for resulting current distribution of the MoM analysis, reflection coefficient value of the antenna is calculated. The related parameters at 2.21 GHz are found to be;

$$c_1 = 3.1753 - 1.3151i$$

$$c_2 = 0.5524 + 0.7159i$$

$$\beta_1 = -1.6475 - 60.7624i$$

$$\beta_2 = 0.6294 + 59.9048i$$

That result is given comparatively with the Schaubert's study [5] in Figure 5.11.

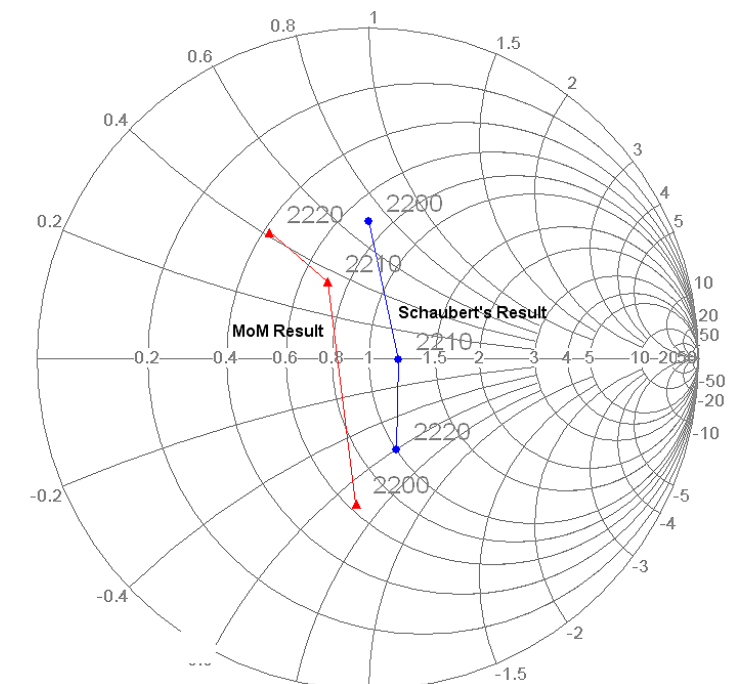


**Figure 5.11 Comparative demonstration of input impedance of MoM and Schaubert's results [5]**

According to the above results, it can be said that, changing slot length from 1.4 to 1.2 cm positively affects antenna performance. On the other hand resonance frequency of the antenna changes slightly. Besides, patch current distribution is

calculated and compared with the HFSS® output at the center of the patch in Figure 5.12.

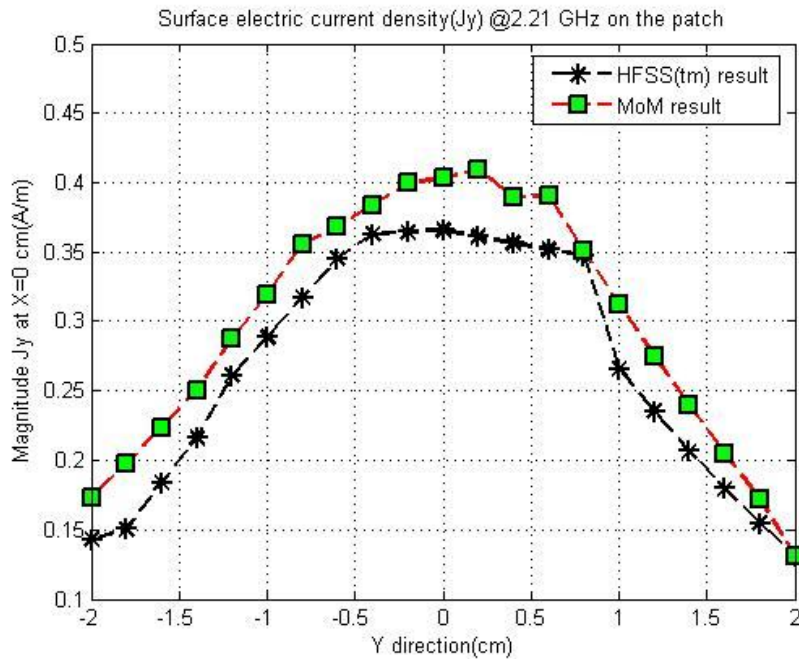


Figure 5.12 Surface electric current distribution on the microstrip patch at 2.21 GHz at  $x=0$  cm

By looking at these results, it is observed that our approach gives similar results to Schaubert's study [5]. On the other hand comparative analysis of current distributions on the microstrip and on the patch demonstrates the difference of the two approaches. By looking at the absolute reflection coefficient they are close. However, phase of the two results are differs solutions on the Smith Chart. This phase difference is very clear in Figure 5.8.

## 5.2.2 Slot Length is 1 cm

### Model 3:

This model is structured and analyzed with the parameters:

$$f = 2.25 \text{ GHz}$$

$$\epsilon_a = 2.55$$

$$\epsilon_b = 2.55$$

$$L_p = 4 \text{ cm}$$

$$w_p = 3 \text{ cm}$$

$$L_{strip} = 7 \text{ cm}$$

$$W_f = 0.495 \text{ cm}$$

$$W_{ap} = 0.11 \text{ cm}$$

$$L_{ap} = 1 \text{ cm}$$

$$L_s = 2 \text{ cm}$$

$$d_a = 0.16 \text{ cm}$$

$$d_b = 0.16 \text{ cm}$$

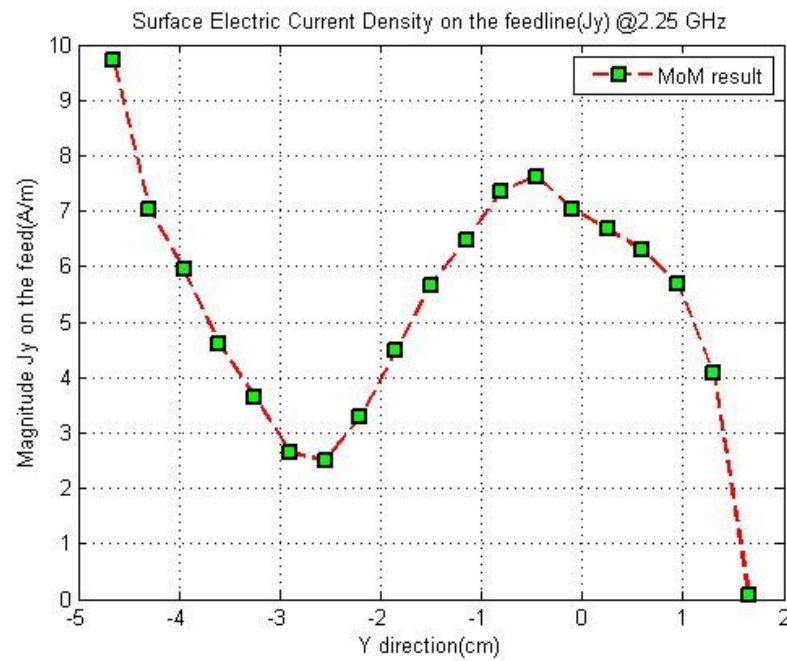


Figure 5.13 Surface electric current distribution on the microstrip feedline at 2.25 GHz.

For this structure, there is very little coupling from feedline to the patch for this geometry. This coupling difference becomes much more apparent in our analysis. In Figure 5.14 and Figure 5.15 current distribution results of the frequencies 2.2 GHz and 2.3 GHz shown respectively.

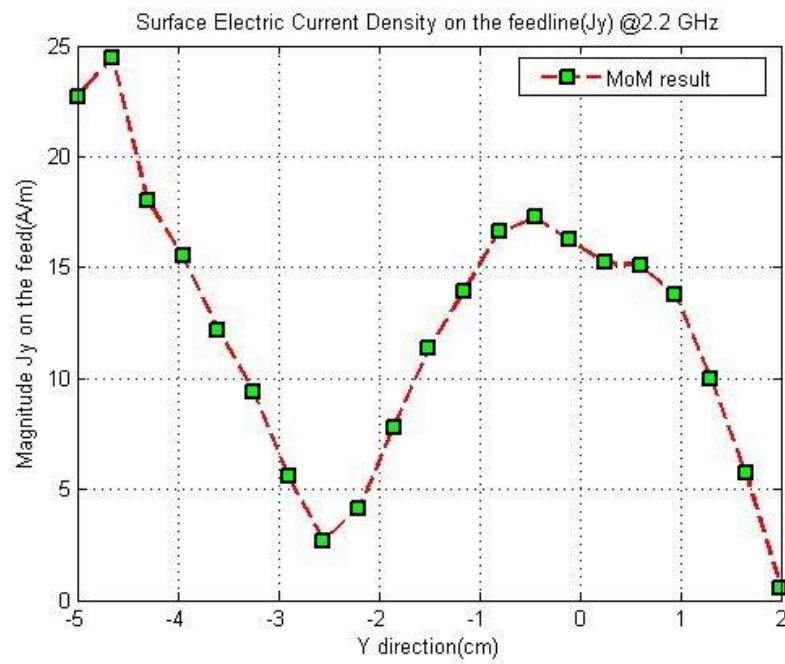
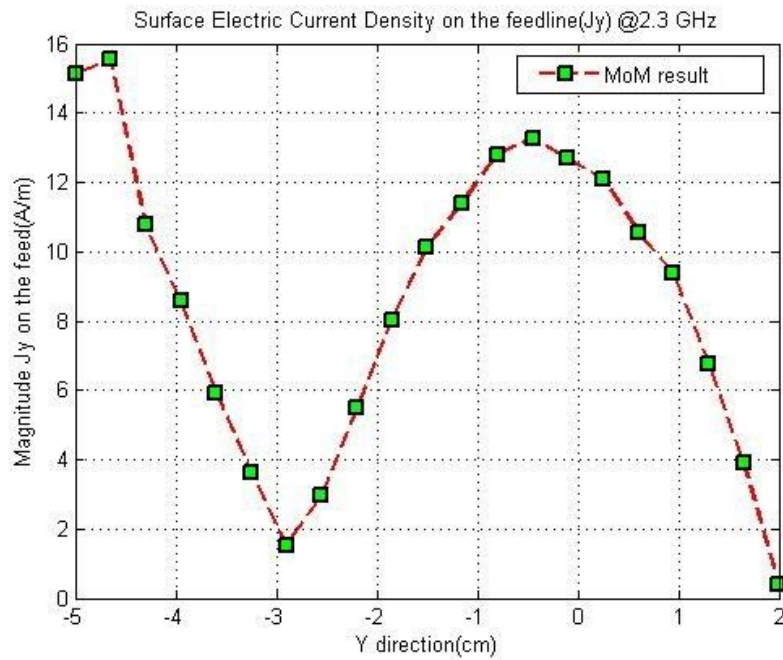


Figure 5.14 Surface electric current distribution on the microstrip feedline at 2.2 GHz.



**Figure 5.15 Surface electric current distribution on the microstrip feedline at 2.3 GHz.**

By using Prony's method for resulting current distribution of the MoM analysis, reflection coefficient value of the antenna can be calculated. The related parameters at 2.2 GHz are evaluated to be;

$$c_1 = 4.9083 - 1.0923i$$

$$c_2 = 1.8734 + 2.3129i$$

$$\beta_1 = -1.5317 - 65.5376i$$

$$\beta_2 = -9.1227 + 68.3853i$$

That result is given comparatively with the Schaubert's study [5] in Figure 5.10.

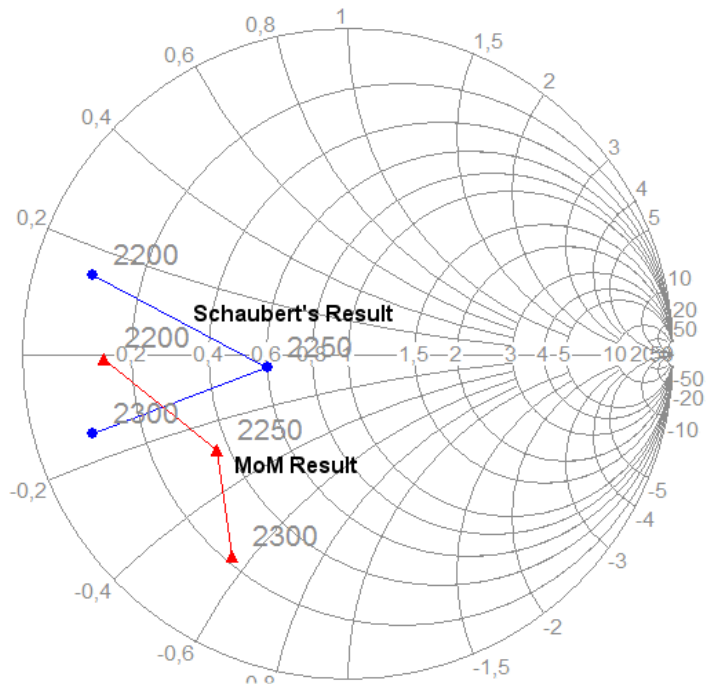


**Figure 5.16 Comparative demonstration of input impedance from MoM and Schaubert's results[5]**

According to the above results, it can be said that, changing slot length from 1.2 to 1 cm negatively affects antenna performance. There is almost 10 dB decrease in S11 value for all analysis approaches. On the other hand, resonance frequency changes slightly as it is expected. This time it moves to 2.25 GHz. For both S11 value and the resonance frequency, there occurs a bigger change than previous case. Patch current distributions for this structure are also demonstrated.

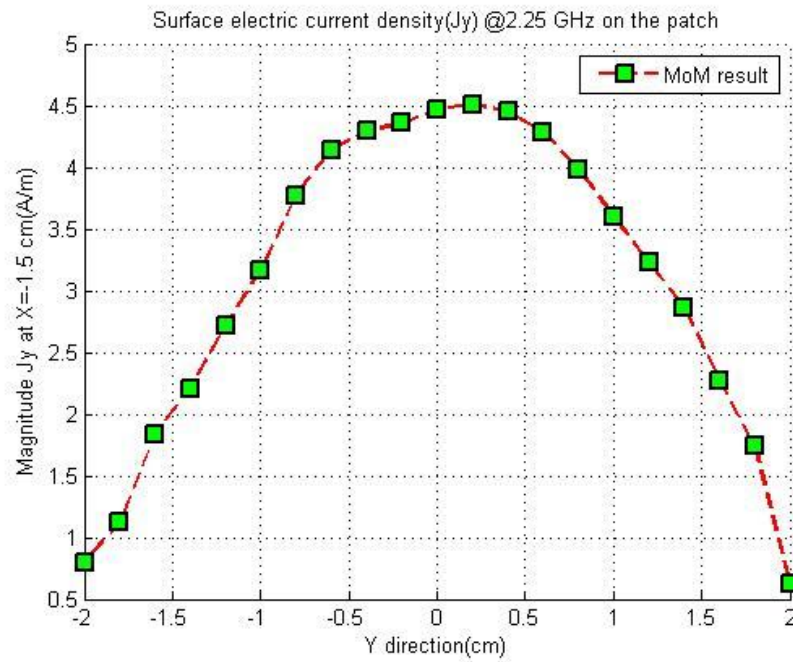


Figure 5.17 Surface electric current distribution on the microstrip patch at 2.25 GHz,  $x=-1.5$  cm

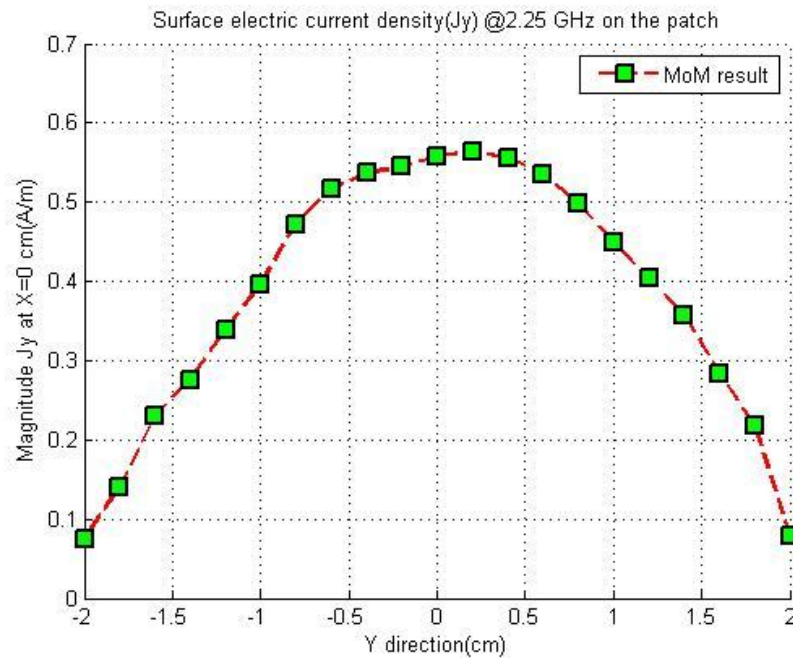


Figure 5.18 Surface electric current distribution on the microstrip patch at 2.25 GHz,  $x=0$  cm

As the slot length decreases, coupling from microstrip to patch is also decreasing. In this case the two results become much more different than the previous case. However, by looking at the Smith Chart demonstration, the two approaches performs similar characteristic in the sense of phase difference in the band.

### **5.3 Analysis of Stub Length Effects to the Antenna**

In this analysis feedline stub length ( $L_s$ ) is a variable. By changing the stub length, slot coupled patch structure's performance is changed. Being similar to the slot position analysis, changing the stub length also changes the coupling from the feedline to the patch. This is because, as the stub length is decreased from 2 cm, maximum current location does not coincide with the slot location. In another meaning, stub length cannot continue to be  $\lambda/4$  long.

#### **5.3.1 Stub Length is 2 cm**

##### **Model 4:**

This model is structured and analyzed with the parameters:

$$f = 2.2 \text{ GHz}$$

$$\varepsilon_a = 2.55$$

$$\varepsilon_b = 2.55$$

$$L_p = 4 \text{ cm}$$

$$w_p = 3 \text{ cm}$$

$$L_{strip} = 7 \text{ cm}$$

$$W_f = 0.442 \text{ cm}$$

$$W_{ap} = 0.155 \text{ cm}$$

$$L_{ap} = 1.12 \text{ cm}$$

$$L_s = 2 \text{ cm}$$

$$d_a = 0.16 \text{ cm}$$

$$d_b = 0.16 \text{ cm}$$

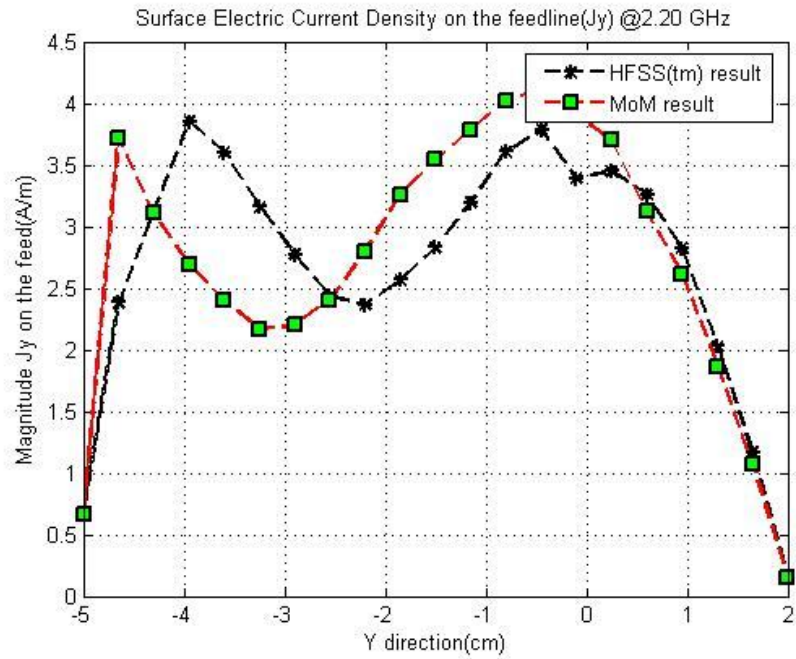


Figure 5.19 Surface electric current distribution on the microstrip feedline at 2.2 GHz.

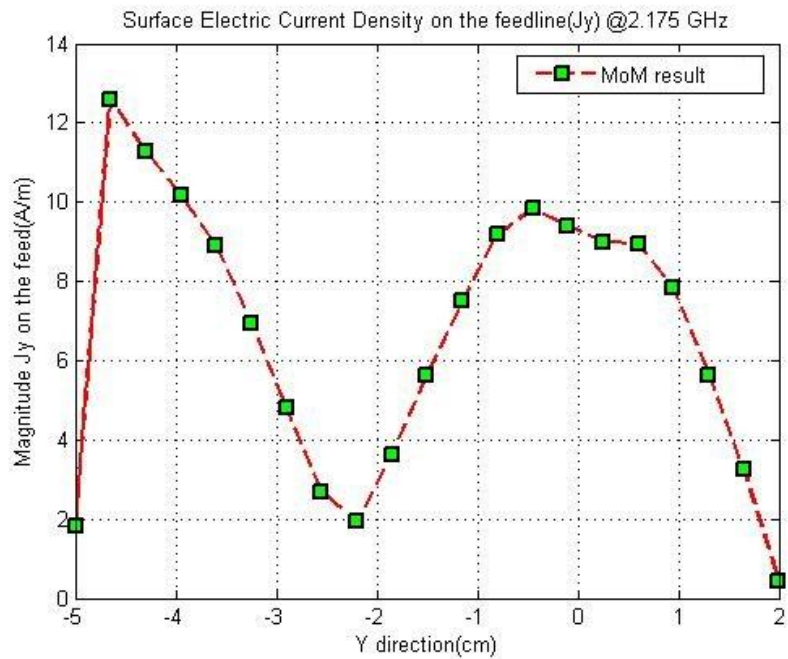
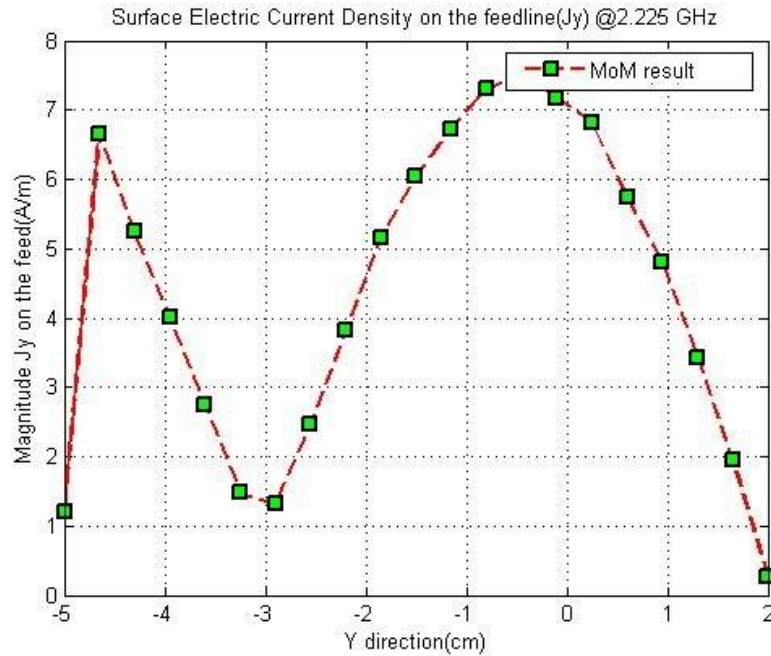


Figure 5.20 Surface electric current distribution on the microstrip feedline at 2.175 GHz.



**Figure 5.21 Surface electric current distribution on the microstrip feedline at 2.225 GHz.**

By using Prony's method with current distribution of the MoM analysis, reflection coefficient value of the antenna can be calculated. The related parameters at 2.2 GHz are calculated to be;

$$c_1 = 2.8154 - 1.8012i$$

$$c_2 = 0.9105 - 0.1031i$$

$$\beta_1 = -2.3790 - 63.1494i$$

$$\beta_2 = -5.9114 + 65.1079i$$

The resulting current distribution at this frequency is given comparatively with the HFSS® output in Figure 5.19.

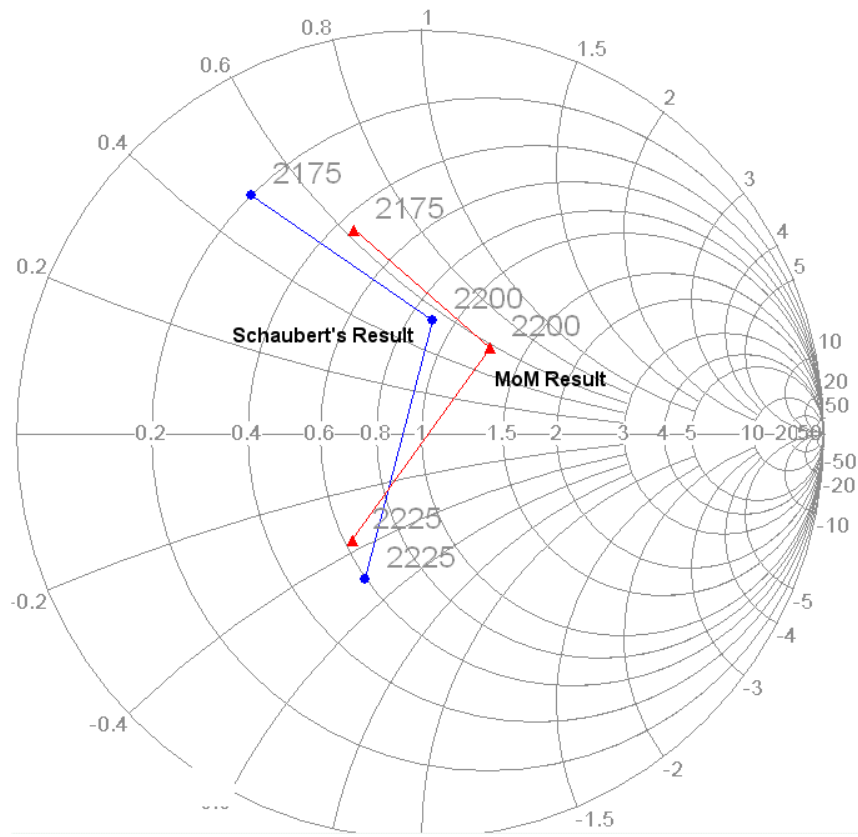


**Figure 5.22 Comparative demonstration of input impedance of MoM and Schaubert's results[5]**

Patch current distributions for this structure are calculated and compared with the HFSS® outputs as depicted in below figures.

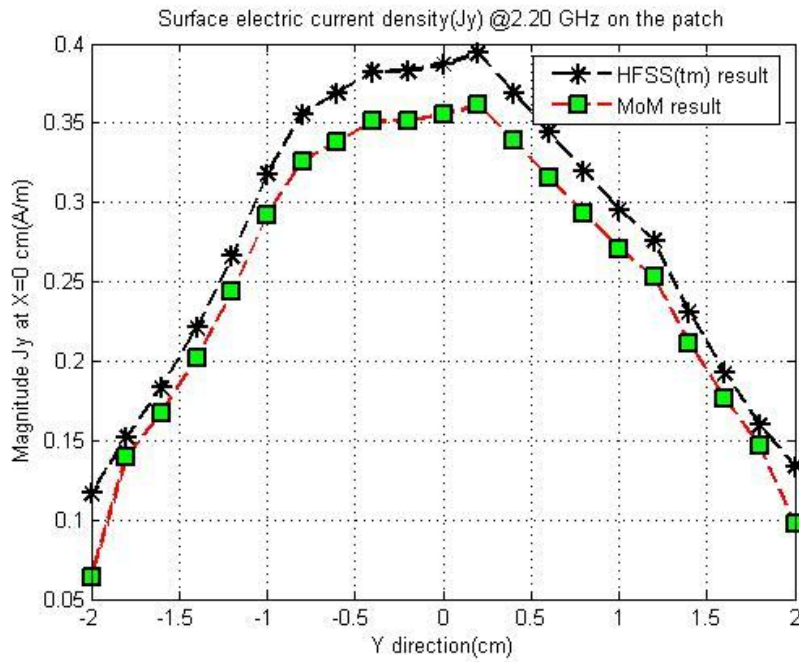


Figure 5.23 Surface electric current distribution on the microstrip patch at 2.2 GHz,  $x=0$  cm

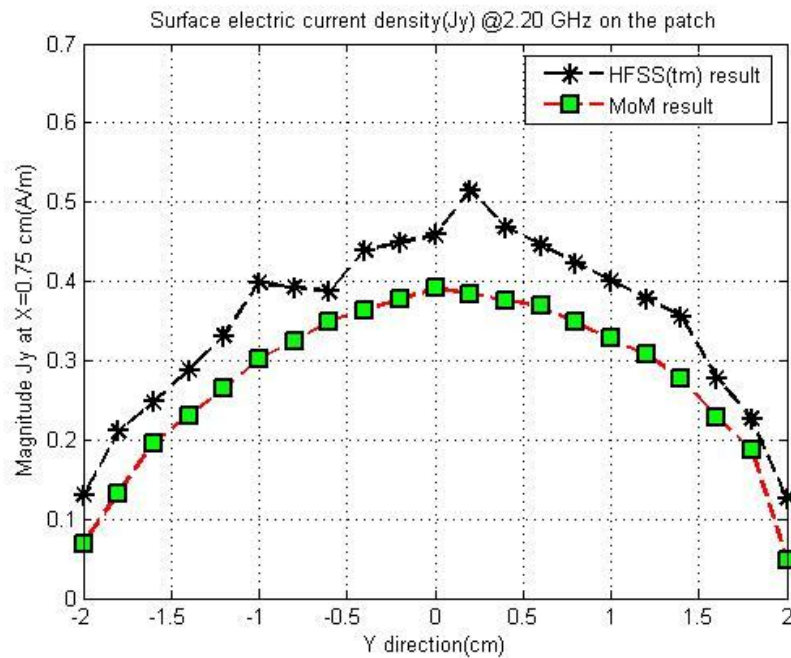


Figure 5.24 Surface electric current distribution on the microstrip patch at 2.2 GHz,  $x=0.75$  cm

By looking at these results, it can be said that our approach gives very similar results to Schaubert's study [5]. By looking at the absolute reflection coefficient at true resonant frequency, they are very close. However, phase of the two results are differs solutions on the Smith Chart. This behavior is quite clear in Figure 5.19.

### 5.3.2 Stub Length is 1.6 cm

#### Model 5:

This model is structured and analyzed with the parameters:

$$f = 2.2 \text{ GHz}$$

$$\varepsilon_a = 2.55$$

$$\varepsilon_b = 2.55$$

$$L_p = 4 \text{ cm}$$

$$w_p = 3 \text{ cm}$$

$$L_{strip} = 7 \text{ cm}$$

$$W_f = 0.442 \text{ cm}$$

$$W_{ap} = 0.155 \text{ cm}$$

$$L_{ap} = 1.12 \text{ cm}$$

$$L_s = 1.6 \text{ cm}$$

$$d_a = 0.16 \text{ cm}$$

$$d_b = 0.16 \text{ cm}$$

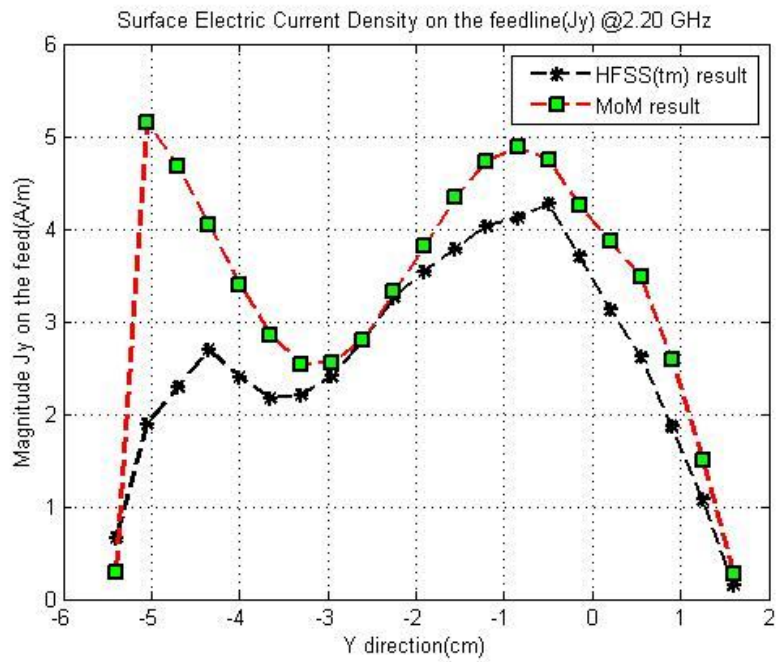


Figure 5.25 Surface electric current distribution on the microstrip feedline at 2.2 GHz.

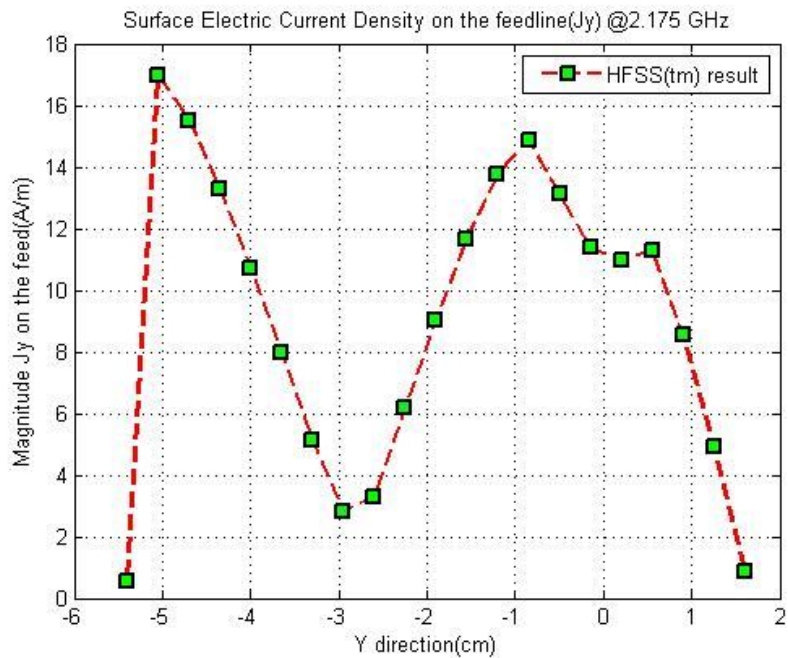
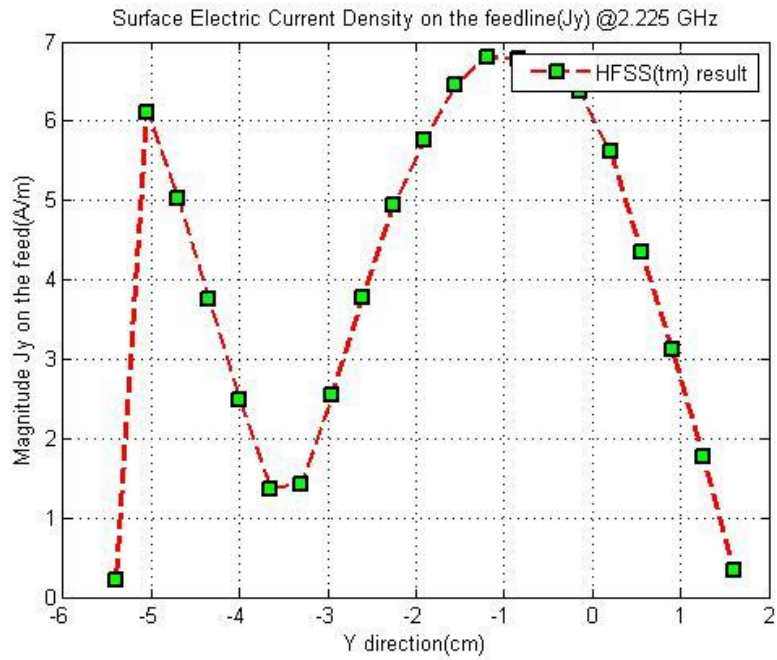


Figure 5.26 Surface electric current distribution on the microstrip feedline at 2.175 GHz.



**Figure 5.27 Surface electric current distribution on the microstrip feedline at 2.225 GHz.**

By using Prony’s method with current distribution of the MoM analysis, reflection coefficient value of the antenna is calculated. It is obviously seen that, decreasing stub length from 2 cm to 1.6 cm decreased coupling, as well. This is because; maximum current location of the microstrip feedline is no more below the slot line. The related parameters at 2.2 GHz are calculated to be;

$$c_1 = 3.4218 - 1.2564i$$

$$c_2 = 1.3434 + 0.8445i$$

$$\beta_1 = 1.0232 - 62.8313i$$

$$\beta_2 = -14.5857 + 62.7486i$$

That result is given comparatively with the Schaubert’s study [5] in Figure 5.28

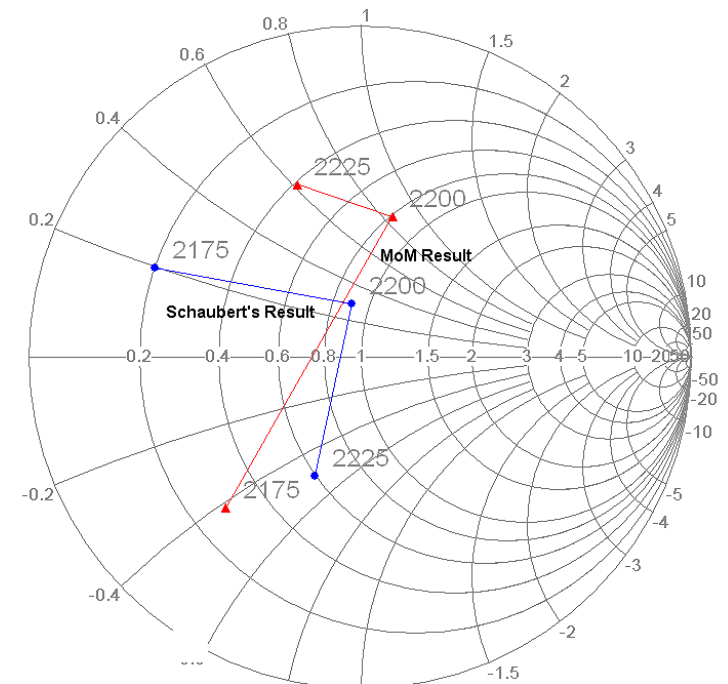


**Figure 5.28 Comparative demonstration of input impedance of MoM and Schaubert's results[5]**

Patch current distribution at the center of the patch for this structure are calculated and compared with the HFSS® outputs as depicted in Figure 5.29.

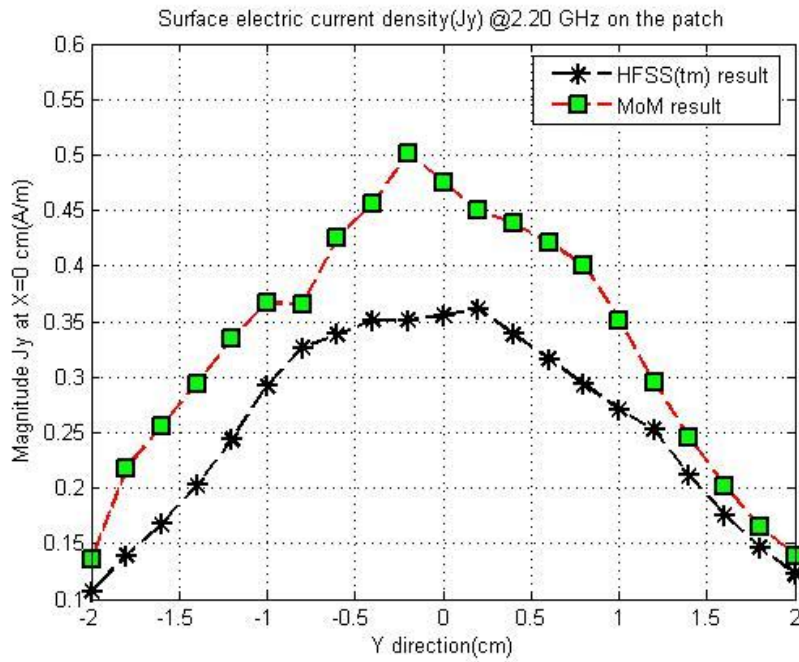


**Figure 5.29** Surface electric current distribution on the microstrip patch at 2.2 GHz, x=0 cm

By looking at the absolute reflection coefficients, it can be said that two studies yields similar results. However, phase of the two results creates the difference between the solutions on the Smith Chart. This behavior is quite clear in Figure 5.25.

### 5.3.3 Stub Length is 0.6 cm

#### Model 6:

This model is structured and analyzed with the parameters:

$$f = 2.2 \text{ GHz}$$

$$\epsilon_a = 2.55$$

$$\epsilon_b = 2.55$$

$$L_p = 4 \text{ cm}$$

$$w_p = 3 \text{ cm}$$

$$L_{strip} = 7 \text{ cm}$$

$$W_f = 0.442 \text{ cm}$$

$$W_{ap} = 0.155 \text{ cm}$$

$$L_{ap} = 1.12 \text{ cm}$$

$$L_s = 0.6 \text{ cm}$$

$$d_a = 0.16 \text{ cm}$$

$$d_b = 0.16 \text{ cm}$$

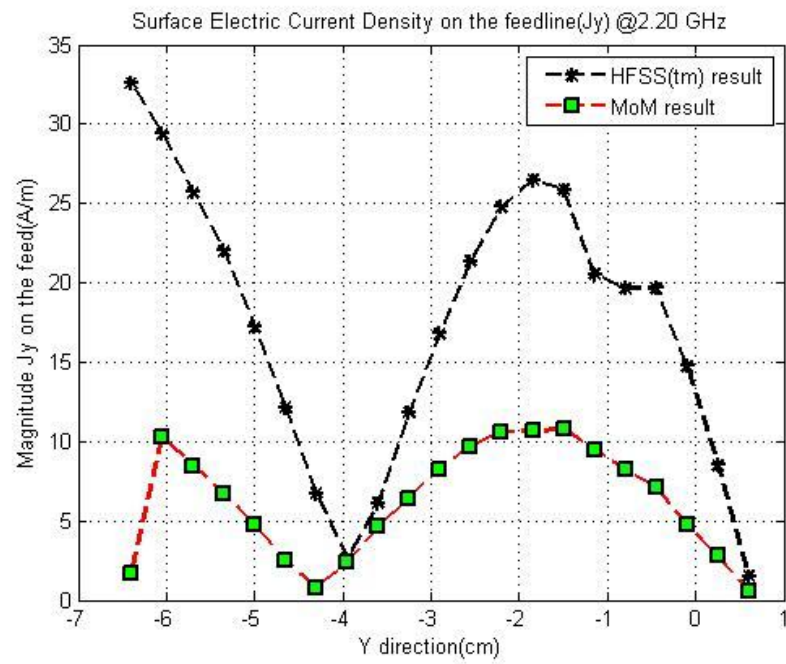


Figure 5.30 Surface electric current distribution on the microstrip feedline at 2.2 GHz.

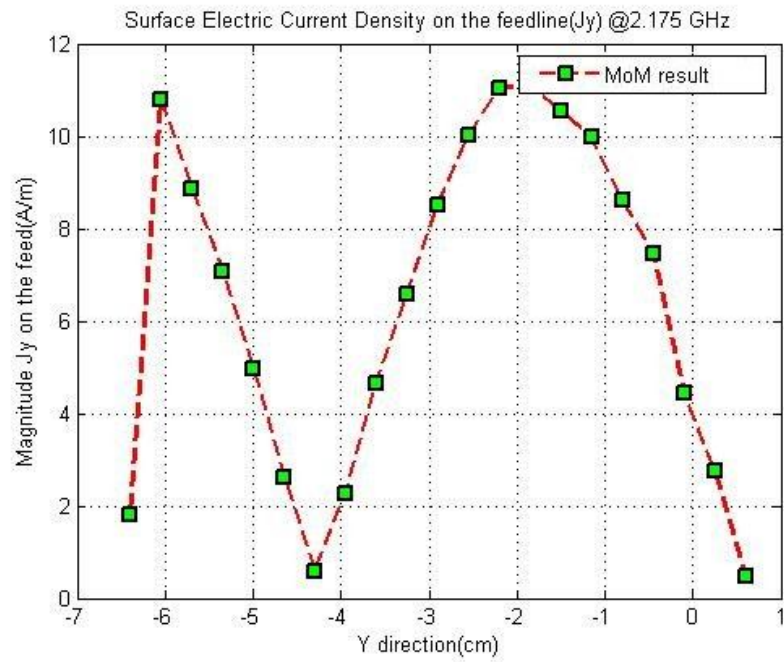


Figure 5.31 Surface electric current distribution on the microstrip feedline at 2.175 GHz.

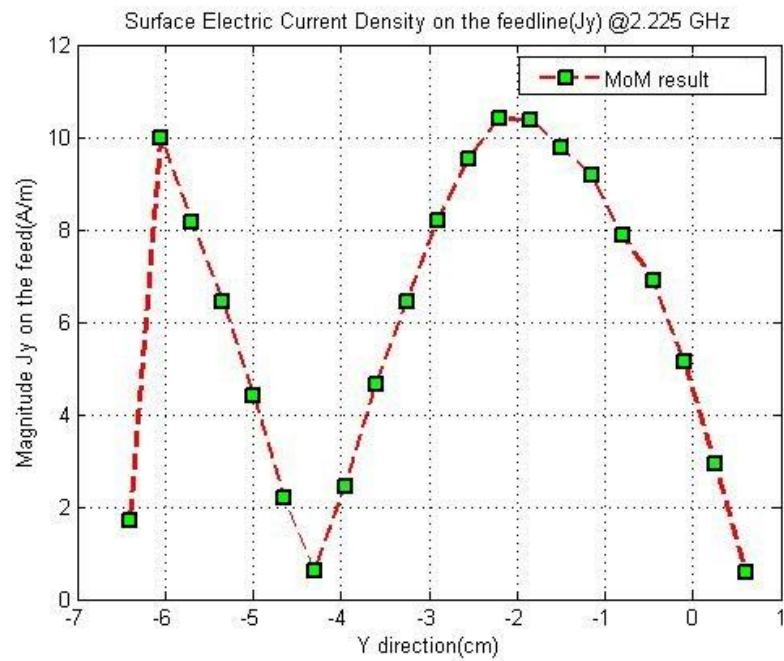


Figure 5.32 Surface electric current distribution on the microstrip feedline at 2.225 GHz.

By using Prony's method with current distribution of the MoM analysis, reflection coefficient value of the antenna is calculated. It is observed that, decreasing stub length from 1.6 cm to 0.6 cm decreased coupling from feedline to patch very much. The related parameters at 2.2 GHz are calculated to be;

$$c_1 = -4.4906 - 4.0487i$$

$$c_2 = -2.1915 + 4.8458i$$

$$\beta_1 = -0.3054 - 59.6217i$$

$$\beta_2 = -0.4873 + 59.3803i$$

That result is given comparatively with the Schaubert's study [5] in Figure 5.33.

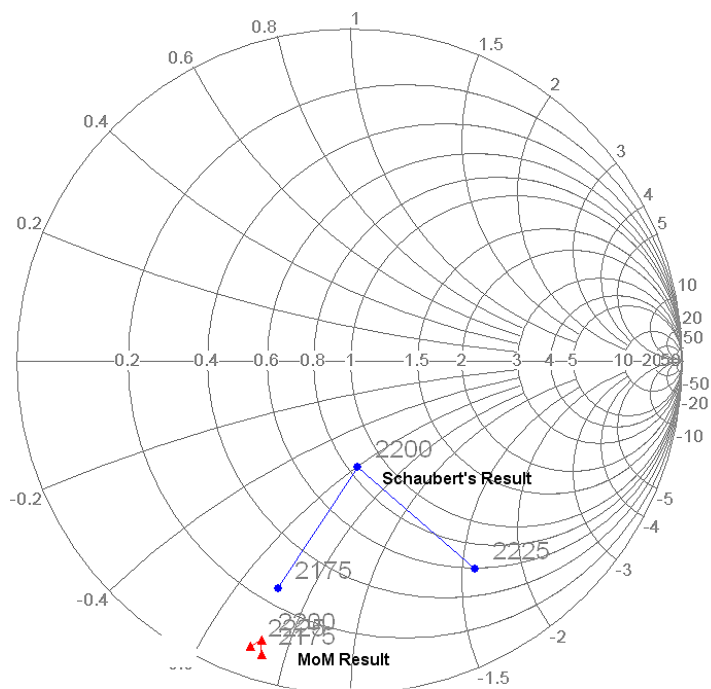


**Figure 5.33 Comparative demonstration of input impedance of MoM and Schaubert's results[5]**

Patch current distributions for this structure are calculated and compared with the HFSS® outputs as depicted in Figure 5.34 and Figure 5.35.

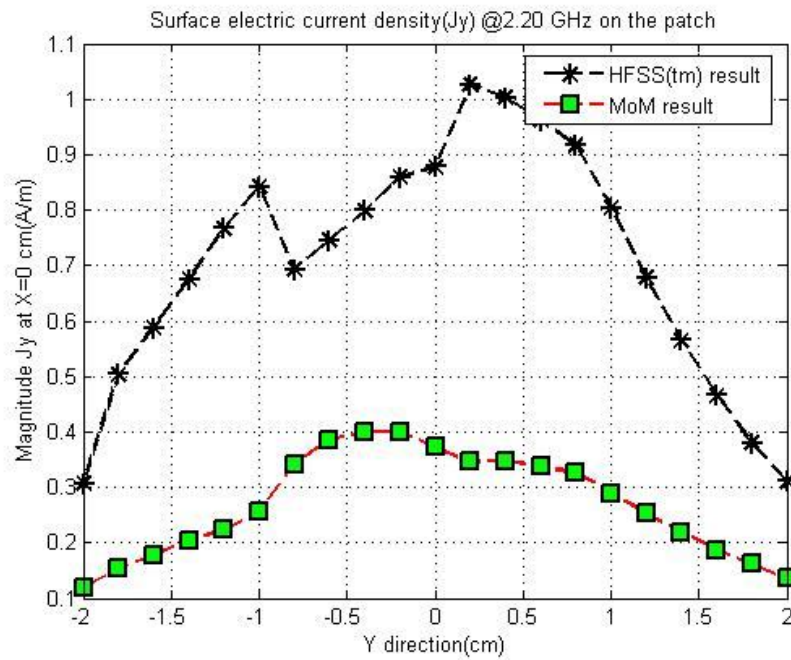


Figure 5.34 Surface electric current distribution on the microstrip patch at 2.2 GHz, x=0 cm

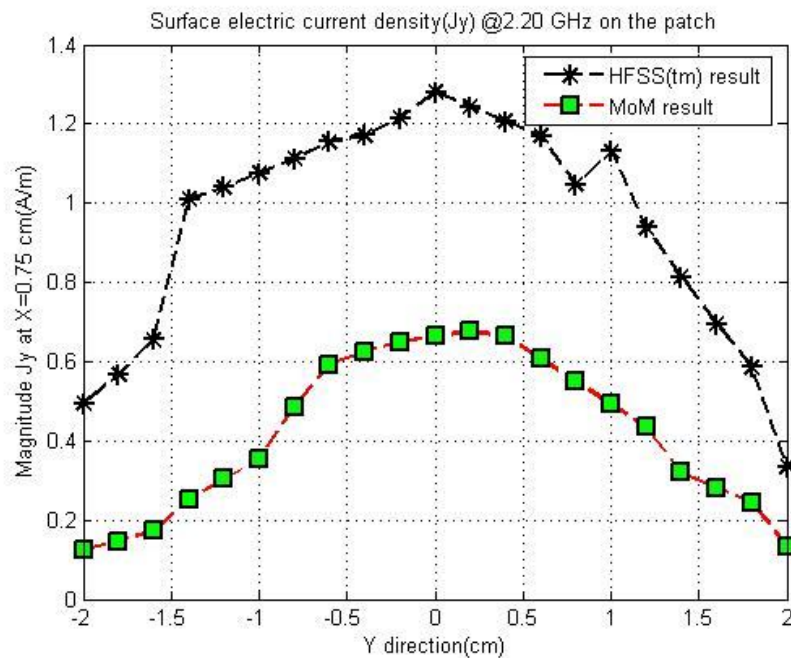


Figure 5.35 Surface electric current distribution on the microstrip patch at 2.2 GHz, x=0.75 cm

By observing these results, it is clear that our approach and Schaubert's study yields similar frequency responses. However, the magnitude difference of the feedline current distribution creates the difference between the solutions on the Smith Chart. This behavior is quite clear in Figure 5.33.

### 5.3.4 Stub Length is 0.4 cm

#### Model 7:

This model is structured and analyzed with the parameters:

$$f = 2.2 \text{ GHz}$$

$$\varepsilon_a = 2.55$$

$$\varepsilon_b = 2.55$$

$$L_p = 4 \text{ cm}$$

$$w_p = 3 \text{ cm}$$

$$L_{strip} = 7 \text{ cm}$$

$$W_f = 0.442 \text{ cm}$$

$$W_{ap} = 0.155 \text{ cm}$$

$$L_{ap} = 1.12 \text{ cm}$$

$$L_s = 0.4 \text{ cm}$$

$$d_a = 0.16 \text{ cm}$$

$$d_b = 0.16 \text{ cm}$$

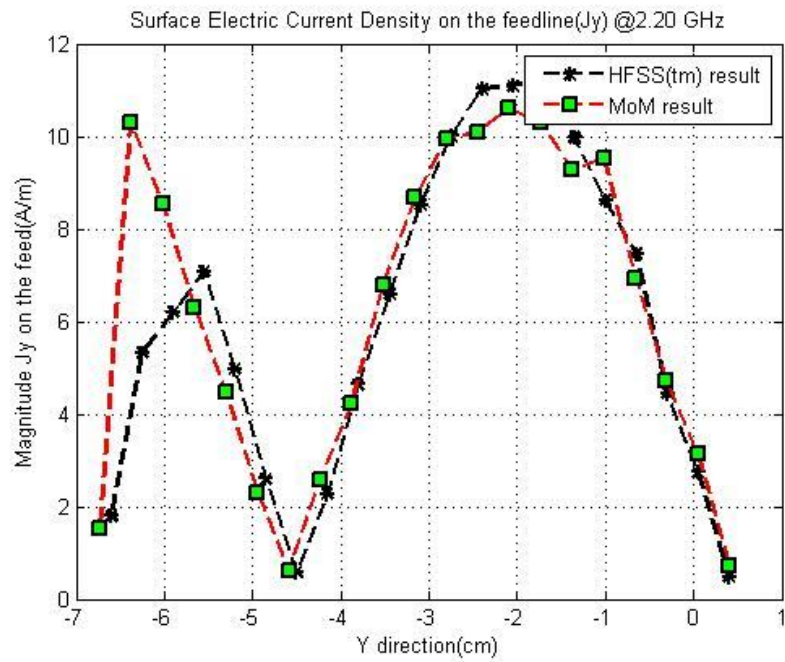


Figure 5.36 Surface electric current distribution on the microstrip feedline at 2.2 GHz.

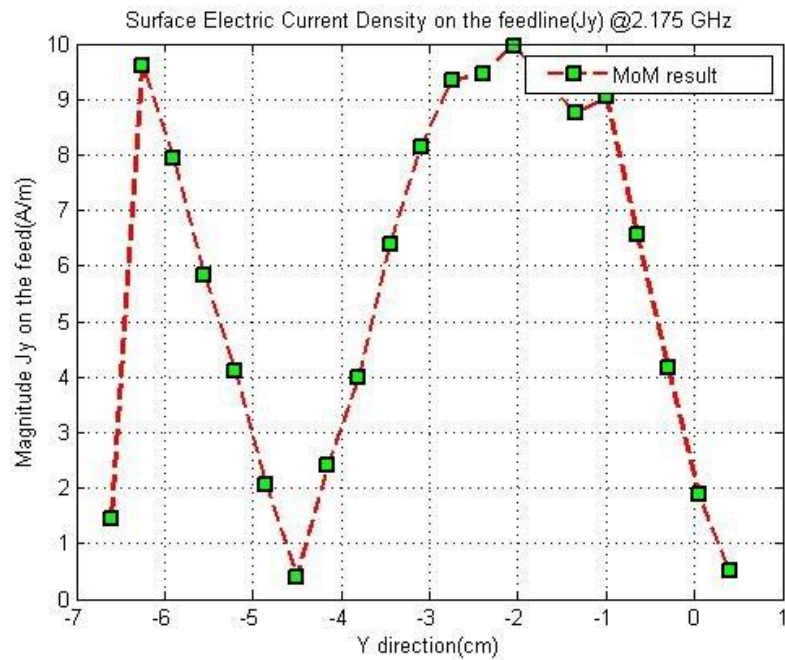
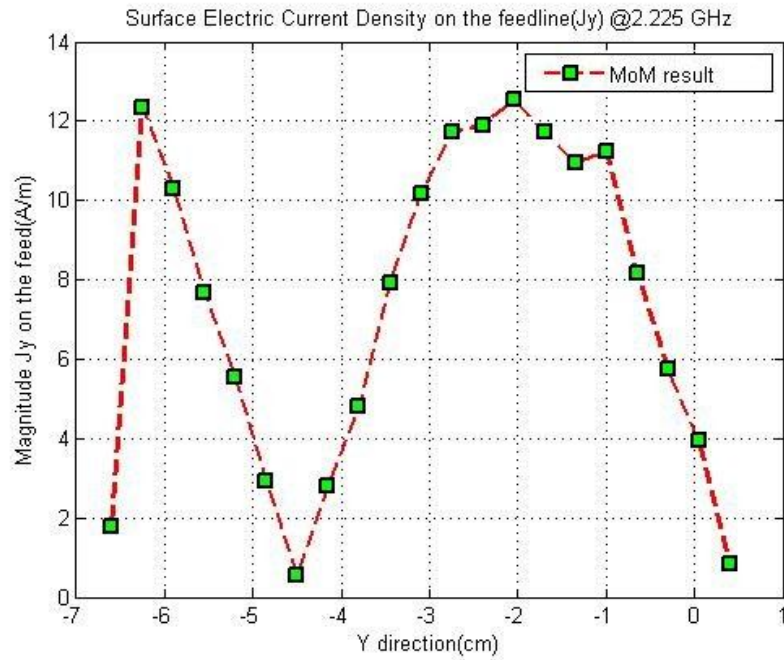


Figure 5.37 Surface electric current distribution on the microstrip feedline at 2.175 GHz.



**Figure 5.38 Surface electric current distribution on the microstrip feedline at 2.225 GHz.**

By using Prony's method with current distribution of the MoM analysis, reflection coefficient value of the antenna is calculated. As it is expected, decreasing stub length from 0.6 cm to 0.4 cm decreased coupling from feedline to patch. This time, coupling and S11 get very close to 0. This is because; slot is in very close neighborhood of the minimum current location of the feedline. The related parameters at 2.2 GHz are calculated to be;

$$c_1 = -7.4989 + 0.3966i$$

$$c_2 = -4.1071 + 5.8716i$$

$$\beta_1 = -9.1420 - 56.9133i$$

$$\beta_2 = -11.4942 + 57.1238i$$

That result is given comparatively with the Schaubert's study [5] in Figure 5.39.

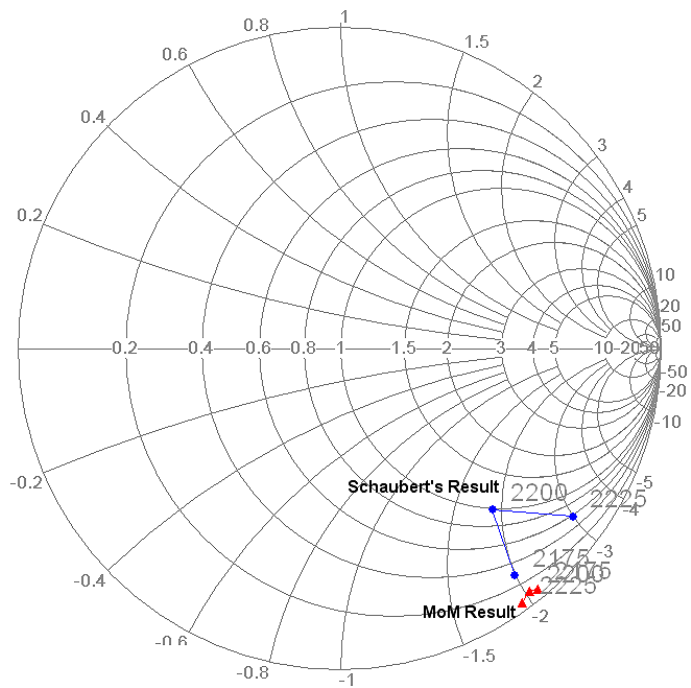


**Figure 5.39 Comparative demonstration of input impedance of MoM and Schaubert's results[5]**

Patch current distributions for this structure are calculated and compared with the HFSS® outputs as depicted in Figure 5.40.

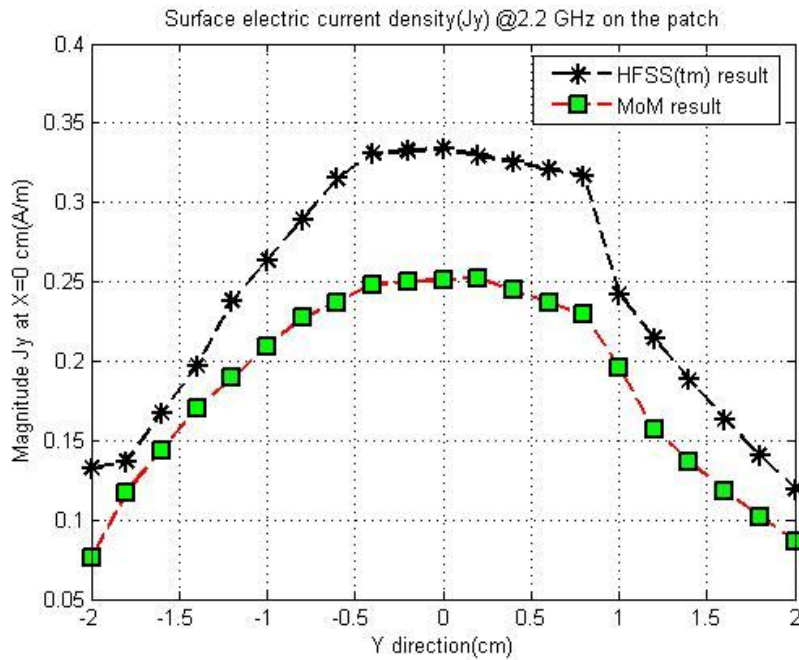


**Figure 5.40 Surface electric current distribution on the microstrip patch at 2.2 GHz, x=0 cm**

According to the parametric analysis on the slot coupled patch antenna, some important deductions can be extracted. First important deduction is about the position of the slot. By looking at the electric current distribution along the microstrip line, optimum stub length can be decided as  $\lambda/4$ . In order to test that, other slot positions geometry modifications are done and simulations are carried out both by MoM and HFSS®. All results verified the optimum slot position as the center of the patch. This is because; electric current distribution hits the maximum, just exactly at this point for our frequency and feedline combination.

On the other hand, stub length is also another important parameter for catching the maximum coupling from feedline to the patch. Since, slot position must coincide with the maximum current location; stub length also can change that. For that parameter, our program and results from the literature give the same deductions.

Third important parameter for slot coupled patch antenna is slot length. It can be changed in order to fine tune the antenna. By changing slot position and the stub

length, antenna coarse tuning is succeeded. Then fine tuning can be done by changing the slot length in order to find optimum value.

In this parametric analysis, our results and other ones reasonably coincide. However, for some cases they diverge little bit. As antenna performance converges to the best, all results are very similar. At some extreme cases such as, too few coupling from feedline to patch, they begin to diverge. Also, at the center of the patch electric current distributions are very similar. However, at the sides of the patch, they resemble less. This is because; our Green's coefficients assume an infinite ground plane. At the sides it may not yield suitably good approximations.

Results of this study are also compared with the results from the previous approaches [1,5] from the literature. Generally results of this study, hold with the others. On the other hand, phase and magnitude of the reflection coefficients does not always coincide. This is because; our MoM approach needs very high resolution discretization for perfect solution. Besides, length of the sub-domains becomes more important in high frequency solutions. Since strip coupled patch structure is a narrow band antenna, it needs very high resolution for sweeping frequencies. Because of that, missing the true resonant frequencies for non-perfect solutions are possible. At some frequencies, missing the true resonance frequency may yield different S11 parameters for different approaches.

## CHAPTER 6

### CONCLUSION

#### **6.1 Summary**

In this study, analysis of microstrip fed-slot coupled patch antenna structure using closed form Green's functions is achieved. Closed form Green's functions are utilized in conjunction with MoM. First of all, brief historical background of printed structures and slot coupled patch antennas are put in the picture. Main features and the advantages of the antenna which are the reasons of such a great deal of attention are mentioned. In historical manner, new improvements, perspectives, modifications are explained. In this course, developed and modified analysis methods are explained and compared. Besides, other related works and structures briefly mentioned.

Moments method and its application fields are detailed. Importance of choice of basis and testing functions explained and different approaches compared in order to clarify advantages of using Galerkin's method. Next, analysis of the printed structures using MoM is described including the Green's function formulation. Spatial domain and spectral domain MoM formulation is done and computational difficulties are discussed. As a remedy to these difficulties closed form Green's functions suggested with formulations.

Then, the proposed geometry of aperture coupled patch antenna [1] structure is formed and the problem is established with the unknown current functions on the boundaries. Then by applying MoM formulation, using boundary conditions on the feedline, slot and the patch and carrying out necessary derivations integral equations are obtained. These integral equations are used to derive MoM matrix, which is used to find current distributions on the boundaries with excitation vector. Resulting

current distribution is used to find S11 parameter of the antenna by applying Prony's method [42]. Same calculation procedure is repeated to learn antenna's characteristics in different frequencies.

Slot coupled patch antennas have some important parameters such as slot length, slot position, stub length etc. These parameters can be changed in order to coarse or fine tune the antenna, or to change the coupling from feedline to the patch. Finally, antenna performance and characteristic changes are investigated by carrying out a parametric analysis. In this parametric analysis, antenna is modeled; current distributions are obtained and demonstrated comparatively with the HFSS<sup>®</sup> outputs. Then S11 parameters are calculated and given in comparison tables including HFSS<sup>®</sup> outputs and solutions reported in the literature. As a result of the parametric analysis, antenna performance changes based on the geometrical modifications are demonstrated. The result of the parametric analysis yielded very similar behaviours over the frequency band of the antennas. However, there was some amplitude or phase mismatches between our results and the available in the literature. This was because, this study applied a different method from other studies analysing the same structure.

In order to carry out calculations of this study, MoM is preferred over FEM which is a solution method of HFSS<sup>®</sup>. This is because, this study utilizes closed form Green's functions as build stone of the problem. Using MoM with the Galerkin's method results symmetric MoM matrices. This simplifies the computations and decreases the order of unknowns. Each final equation is an inner product term which is a 4-dimensional integral. Two of the integrals are from the definition of the inner product and two of them are from the closed-form Green's functions. Choosing the basis functions as rooftops, the two of the integrals which are called as convolution integral over testing and basis functions can be carried out analytically. Then the final equation becomes a 2-dimensional integral equation.

However, FEM is a more generic solution technique. Its systematic generality of the method makes it possible to construct general purpose programs for solving wide range of problems. For a specific planar geometry problem it would require a great deal of work and computations. In this method meshing and discretization is much harder tasks. Preparing the data and generating grids for FEM are very time consuming phases. Additionally, by applying MoM, problem of multi-planar 3-dimensional geometry is reduced to a problem of coupled 2-dimensional geometries. Hence, meshing is done only for 2-dimensional geometries. On the other hand, FEM would require the solution for all media. HFSS<sup>®</sup> is industrial software which is intended to solve all type of EM problems. It's a generic problem solution tool and, uses FEM which is a more generic solution technique.

In conclusion, slot coupled patch antenna is analyzed using closed form Green's functions in conjunction with MoM. Different structures from the literature are solved and analyzed in comparison with our results and HFSS<sup>®</sup>. As a result of these analyses, very close results are obtained to previously accomplished studies, which verify our method and MoM code. These results and reflection coefficient parameters are demonstrated for feedline and for different locations of the patch in the plots.

## **6.2 Future Work**

As a continuum of this study, geometry could be changed in order to allow dual polarized radiation from the antenna. To do that, two orthogonal slots are required between feedline and the patch. The x and y-directed narrow slots induces y- and x-directed currents respectively on the patch and these currents create dual-polarized radiation. Similarly, study of multiple slotted and circular slot shaped antennas could be carried out for the sake of comparison. This study ends with the calculation of surface currents and scattering parameters for the structure. Radiation pattern calculations are reserved for the future work.

## REFERENCES

- [1] Pozar, D. M., "Microstrip Antenna Aperture-Coupled to a Microstripline," *Electron. Lett.*, Vol. 21, No. 2, 49–50, January 1985.
- [2] Pozar, D. M., "A Review of Aperture Coupled Microstrip Antennas: History, Operation, Development, and Applications," University of Massachusetts at Amherst, May 1996.
- [3] Y. Yoshimura, "A Microstripline Slot Antenna", *IEEE Trans. Microwave Theory and Techniques*, vol. MTT-20, pp. 760-762, November 1972.
- [4] Chinglung Chen and N.G. Alexopoulos, "Modeling Microstrip Line Fed Slot Antennas with Arbitrary Shape," *Electromagnetics*, Vol. 15, No. 5, pp. 567-586, Sep.-Oct, 1995.
- [5] Sullivan, P. L., and D. H. Schaubert, "Analysis of an Aperture Coupled Microstrip Antenna," *IEEE Trans. Antennas Propagation*, Vol. 34, 977–984, August 1986
- [6] Pozar, D. M., "A Reciprocity Method of Analysis for Printed Slot and Slot-Coupled Microstrip Antennas," *IEEE Trans. Antennas Propagation*, Vol. 34, 1439–1446, December 1986.
- [7] Chow, Y. L., J. J. Yang, and G. E. Howard, "Closed-form Spatial Green's Function for the Thick Substrate," *IEEE Trans. Microwave Theory Tech.*, Vol. 39, 588–592, March 1991.
- [8] D. Yau and N. V. Shuley, "Numerical Analysis of an Aperture Coupled Microstrip Patch Antenna Using Mixed Potential Integral Equations and Complex Images," *Progress in Electromagnetics Research*, PIER 18, 229–244, 1998
- [9] Fang, D. G., J. J. Yang, and G. Y. Delisle, "Discrete Image Theory for Horizontal Electric Dipoles in a Multilayered Medium," *IEE Proc.*, Vol. 135H, 297–303, 1988.
- [10] Aksun, M. I., and R. Mittra, "Derivation of Closed-Form Green's Function For a General Microstrip Geometry," *IEEE Trans. Antennas Propagation.*, Vol. 40, 2055–2061, November 1992.
- [11] Jui-Ching-Cheng, "Analysis of a Slot Coupled and Stripline Fed Patch Antenna," May 1993

- [12] Shi-Chang Gao, Le-Wei Li, Mook-Seng Leong, and Tat-Soon Yeo, "Dual-Polarized Slot-Coupled Planar Antenna With Wide Bandwidth," *IEEE Trans. Antennas Propagation*, Vol. 51, No. 3, March 2003
- [13] Chinglung Chen and N.G. Alexopoulos, "Modeling Microstrip Line Fed Slot Antennas with Arbitrary Shape," *Electromagnetics*, Vol. 15, No. 5, pp. 567-586, Sep.-Oct., 1995.
- [14] A. Bhattacharyya, O. Fordham and Y.Liu, "Analysis of Stripline-Fed Slot-Coupled Patch Antennas with Vias for Parallel-Plate Mode Suppression," *IEEE Trans. Antennas Propagation*, Vol. 46, No. 4, April 1998.
- [15] A. Bhattacharyya, "Full Wave Analysis of an Aperture-Coupled Patch Antenna," *Electronics Letters*, Vol. 27, No. 2, pp. 153-155, January 1991
- [16] Richard C. Hall, Juan R. Mosig, "The Analysis of Arbitrarily Shaped Aperture-Coupled Patch Antennas via a Mixed-Potential Integral Equation," *IEEE Trans. Antennas Propagation*, Vol. 44, No. 5, May 1996.
- [17] J. R. Mosig, R. C. Hall, and F. E. Gardiol, "Numerical Analysis of Microstrip Patch Antennas," *The Handbook of Microstrip Antennas*, J. R. James and P. S. Hall, Eds. UK: Peregrinus Press, 1989, ch. 8.
- [18] R. F. Harrington, "Matrix methods for Field Problems," *Proc. IEEE*, vol. 55, pp. 136-49, Feb. 1967.
- [19] L.V Kantorovich, and V.I Krylov, "Approximate Methods of Higher Analysis," (translated from Russian, by C.D Benster). New York: John Wiley Pres, New York, 1965.
- [20] Y.U Vorobev, "Method of Moments in Applied Mathematics," (translated from Russian by Seckler). Gordon&Breach Press, New York, 1965
- [21] B.J.Strait "Applications of the Method of Moments to Electromagnetics," St Cloud, FL SCEEE Press, 1980.
- [22] R.F Harrington, "Origin and Development of the Moment Methods for Field Computation," In E.K Miller et.al., *Computational Electromagnetics*. New York: IEEE Press, 1992, pp.43-47.
- [23] J.H Richmond, "Digital Computer Solutions of Rigorous Equations for Scattering Problems," *Proc. IEEE*, vol.53, Aug. 1965, pp.796-804
- [24] R.F Harrington, "Matrix methods for field problems", *Proc. IEEE*, vol. 55, no.2, Feb, 1967, pp.136-149.

- [25] M.M. Ney, "Method of Moments as Applied to Electromagnetic Problems," *IEEE Trans. Micro. Theo.*, vol. MTT-33, no.10, Oct. 1985, pp.972-980.
- [26] R. F. Harrington, "Field Computation by Moment Methods," New York: MacMillan; Toronto, Ontario; Collier-MacMillan Publishing, 1968.
- [27] N. K. Saydam, "Analysis of Microstrip Lines Using Closed-form Green's Functions," M. Sc. Thesis, Middle East Technical University, Ankara, Turkey, 1996.
- [28] W. C. Chew, *Waves and Fields in Inhomogeneous Media*, New York: IEEE Press, 1995.
- [29] F. Arslan, "Analysis of Slot Geometries Using Closed-form Green's Functions," M. Sc. Thesis, Middle East Technical University, Ankara, Turkey, 1997.
- [30] L. A. Hayırlıođlu, "Use of Computationally Efficient MoM in the Analysis and Design of Printed Structures," Ph.D. Thesis, Middle East Technical University, Ankara, Turkey, 1997.
- [31] S. L. Sobolev, *Partial Differential Equations of Mathematical Physics*, New York: Pergamon Press, 1964.
- [32] M. I. Aksun and R. Mittra, "Choices of Expansion and Testing Functions for The Method of Moments Applied to A Class of Electromagnetic Problems," *IEEE Trans. Microwave Theory Tech.*, vol. MTT-41, pp. 503-509, March, 1993.
- [33] T. Utoh. "Spectral Domain Immitance Approach for Dispersion Characteristics of Generalized Printed Transmission Lines," *IEEE Trans. Microwave Theory Tech.*, vol. MTT-28, pp. 733-736, July 1980.
- [34] M. I. Aksun and R. Mittra, "Derivation of Closed-form Green's Functions for a General Microstrip Geometry," *IEEE Trans. Microwave Theory Tech.*, vol. 40, pp. 2055-2062, Nov. 1992.
- [35] Y. L. Chow, J. J. Yang, and D. F. Fang, and G. E. Howard, "Closed-Form Spatial Green's Function for the Thick Substrate," *IEEE Trans. Microwave Theory Tech.*, vol. 39, pp. 588-592, Mar. 1991.
- [36] M. I. Aksun and R. Mittra, "Derivation of Closed-form Green's Functions for A General Microstrip Geometry," *IEEE Trans. Microwave Theory Tech.*, vol. 40, pp. 2055-2062, Nov. 1992.
- [37] G. Dural and M. I. Aksun, "Closed-form Green's Functions for General Sources and Stratified Media," *IEEE Trans. Microwave Theory Tech.*, vol. 43, no. 7, pp. 1545-1552, Jul. 1995.

- [38] Y. Hua and T. K. Sarkar, "Generalized Pencil-of-Function Method for Extracting Poles of An EM System from Its Transient Response," *IEEE Trans. Antennas Propag.*, vol. AP-37, no. 2, pp. 229–234, Feb. 1989.
- [39] A. Sommerfeld, "Partial Differential Equations in Physics," Academic Press., New York, 1949.
- [40] M. I. Aksun, "A Robust Approach for the Derivation of Closed-form Green's Functions," *IEEE Trans. Microwave Theory Tech.*, vol. 44, no. 5, pp. 651–658, May. 1996.
- [41] M. I. Aksun and G. Dural, "Clarification of Issues on the Closed-form Green's Functions in Stratified Media," *IEEE Trans. Antennas Propagation*, Vol. AP-53, 3644–3653, Nov. 2005.
- [42] S. L. Marple, Jr., "Digital Spectral Analysis with Applications," Prentice Hall, New Jersey, 1987.
- [43] M. I. Aksun and R. Mittra, "Spurious Radiation from Microstrip Interconnects," *IEEE Trans. Electromagnetic Compatibility*, vol. 35, pp. 148-158, May, 1993.
- [44] L. Alatan, M. I. Aksun, K. Mahadevan, M.T. Birand, "Analytical Evaluation of the MoM Matrix Elements," *IEEE Trans. On Microwave Theory and Tech.*, Vol.44, No. 4, Apr. 1996.
- [45] H.Y. Yang, N.G. Alexopoulos, "A Dynamic Model for Microstrip-Slotline Transition and Related Structures," *IEEE Trans. On Microwave Theory and Tech.*, Vol.36, No. 2, Feb. 1988.
- [46] Ş.Ö. Piroğlu, "Analysis of Coupled Lines in Microwave Printed Circuit Elements," MSc. Thesis, Middle East Technical University, Ankara, Turkey, 2006.
- [47] J. Mason, "Chebyshev Polynomials: Theory and Applications," Kluwer Academic Press, 1996

## APPENDIX A

### CALCULATION OF THE CONVOLUTION INTEGRAL OVER BASIS AND TESTING FUNCTIONS

In utilizing MoM, the choice of basis and testing functions are very important. Since Galerkin's method of moment is employed in this study, in which the basis and testing functions are the same, the resulting matrix is symmetric.

If closed-form Green's functions in the spatial domain are used, then each inner product term yields a four dimensional. In order to overcome this computational burden, change of variable method is used. In this way, it can be shown that the convolution over the Green's function and the basis function can be transferred to the convolution over testing and basis function. Hence, choice of basis function must be done in way such that their convolution integral can be carried out analytically. Then each inner product term becomes only a two dimensional integral.

As a result, the mathematical definitions of shifted testing function and its derivative, basis function and its derivative, source function and its derivative are used during the calculations. Because rooftop basis and testing functions are used in this study, definitions are written down mentioned above.

Basis function:

$$J_{xn}(x, y) = \left\{ \begin{array}{ll} \frac{1}{wh_x} [(1-n)h_x + x] & (n-1)h_x \leq x \leq nh_x, \quad |y| \leq \frac{w}{2} \\ \frac{1}{wh_x} [(1+n)h_x - x] & nh_x \leq x \leq (n+1)h_x, \quad |y| \leq \frac{w}{2} \\ 0 & \text{elsewhere} \end{array} \right\} \quad \mathbf{A.1}$$

Derivative of the basis function:

$$\frac{d}{dx} J_{xn}(x, y) = \left\{ \begin{array}{ll} \frac{1}{wh_x} & (n-1)h_x \leq x \leq nh_x, \quad |y| \leq \frac{w}{2} \\ -\frac{1}{wh_x} & nh_x \leq x \leq (n+1)h_x, \quad |y| \leq \frac{w}{2} \\ 0 & \text{elsewhere} \end{array} \right\} \quad \mathbf{A.2}$$

Shifted testing function:

$$J_{xm}(x-u, y-v) = \left\{ \begin{array}{ll} \frac{1}{wh_x} [(1-m)h_x + x - u] & (m-1)h_x + u \leq x \leq mh_x + u, \quad |y-v| \leq \frac{w}{2} \\ \frac{1}{wh_x} [(1+m)h_x - x + u] & mh_x + u \leq x \leq (m+1)h_x + u, \quad |y-v| \leq \frac{w}{2} \\ 0 & \text{elsewhere} \end{array} \right\} \quad \mathbf{A.3}$$

Derivative of the shifted testing function:

$$\frac{d}{dx} J_{xm}(x-u, y-v) = \left\{ \begin{array}{ll} \frac{1}{wh_x} & (m-1)h_x + u \leq x \leq mh_x + u, \quad |y-v| \leq \frac{w}{2} \\ -\frac{1}{wh_x} & mh_x + u \leq x \leq (m+1)h_x + u, \quad |y-v| \leq \frac{w}{2} \\ 0 & \text{elsewhere} \end{array} \right\} \quad \mathbf{A.4}$$

Source function:

$$J_s(x, y) = \left\{ \begin{array}{ll} \frac{-1}{wh_x}(h_x + x) & -h_x \leq x \leq 0 \quad , \quad |y| \leq \frac{w}{2} \\ \frac{1}{wh_x}(h_x - x) & 0 \leq x \leq h_x \quad , \quad |y| \leq \frac{w}{2} \\ 0 & elsewhere \end{array} \right\} \quad \text{A.5}$$

Derivative of source function:

$$\frac{d}{dx} J_s(x, y) = \left\{ \begin{array}{ll} \frac{-1}{wh_x} & -h_x \leq x \leq 0 \quad , \quad |y| \leq \frac{w}{2} \\ \frac{1}{wh_x} & 0 \leq x \leq h_x \quad , \quad |y| \leq \frac{w}{2} \\ 0 & elsewhere \end{array} \right\} \quad \text{A.6}$$

For the feed microstripline, formulation results in an equation with four inner product terms. This inner product terms consist of the convolution integrals of:

- i. basis function with testing function,
- ii. derivative of basis function with derivative of testing function,
- iii. basis function with source function,
- iv. derivative of the basis function with derivative of the source function.

Since functions mentioned above are piecewise continuous, convolution integrals can be calculated in suitable regions. Defining the following notations will simplify the calculations:

$$\begin{array}{lll} BU = (n+1)hx & , & BC = nhx & , & BL = (n-1)hx \\ TU = u + (m+1)hx & , & TC = u + mhx & , & TL = u + (m-1)hx \\ SU = hx & , & SC = 0 & , & SL = -hx \end{array}$$

where TP: Test Positive (left part of the testing function),

TP: Test Negative (right part of the testing function),

BP: Basis Positive (left part of the basis function),  
 BN: Basis Negative (right part of the basis function),  
 SL: Source Left (left part of the source function) and  
 SR: Source Right (right part of the source function).

**i. Convolution of basis function with the testing function**

$$\langle J_{mx}, G_{xx}^A * J_{nx} \rangle = \iint dudv G_{xx}^A(u, v) \iint dx dy J_{mx}(x-u, y-v) J_{nx}(x, y) \quad \text{A.7}$$

**a. Region 1:  $BL \leq TU \leq BC$**

In this region the shaded area in Figure 1,  $I_1$ , is calculated.

$$I_1 = \int_{BL}^{TU} dx TNBP \quad \text{A.8}$$

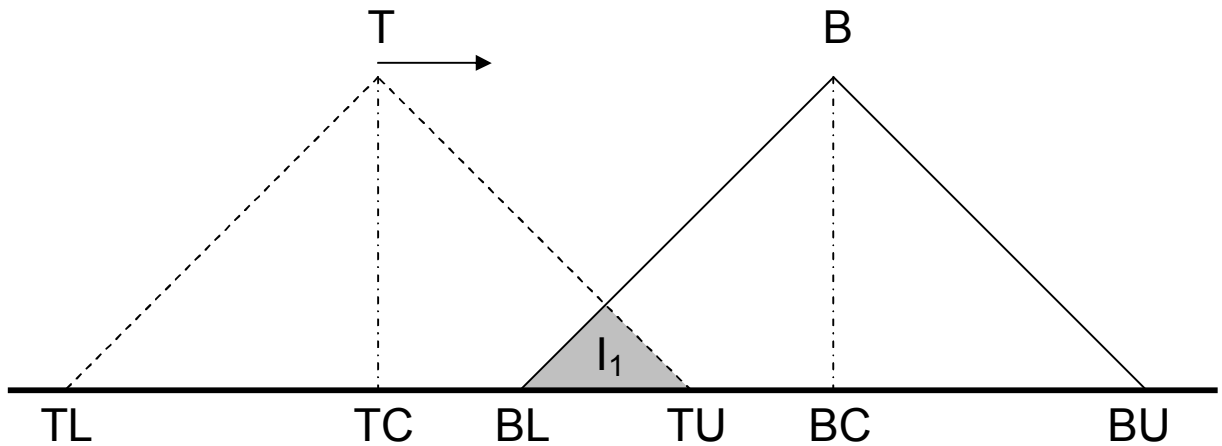


Figure A.1 Region 1 of the convolution over testing and basis functions.

**b. Region 2:  $BC \leq TU \leq BU$**

In this region the shaded area in Figure 2,  $I_1$ , can be calculated by summing integrals  $I_2$ ,  $I_3$  and  $I_4$ .

$$I = I_2 + I_3 + I_4, \quad \text{A.9}$$

$$I_2 = \int_{BL}^{TC} dx TPBP \quad \text{A.10}$$

$$I_3 = \int_{TC}^{BC} dx TNBP \quad \text{A.11}$$

$$I_4 = \int_{BC}^{TU} dx TNBN \quad \text{A.12}$$

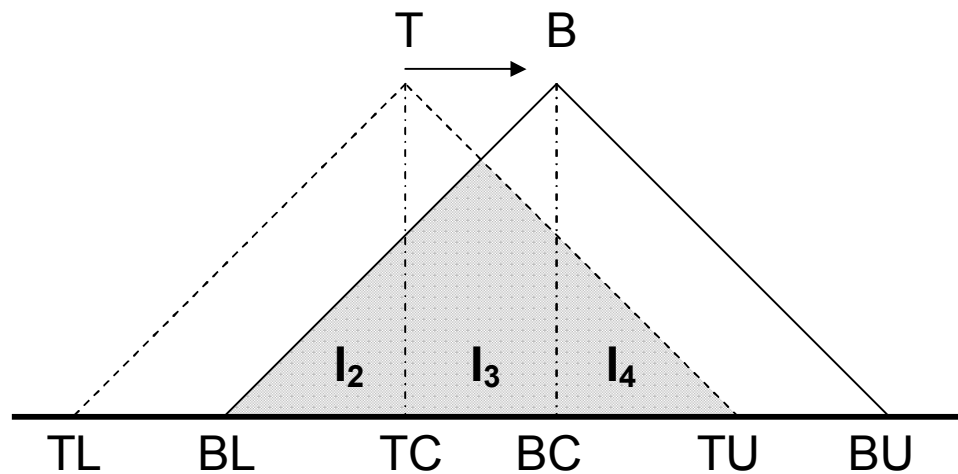


Figure A.2 Region 2 of the convolution over testing and basis functions.

**c. Region 3:  $BC \leq TC \leq BU$**

In this region the shaded area in Figure 3,  $I$ , can be calculated by summing integrals  $I_5$ ,  $I_6$  and  $I_7$ .

$$I = I_5 + I_6 + I_7 \quad \text{A.13}$$

$$I_5 = \int_{TL}^{BC} dx TPBP \quad \text{A.14}$$

$$I_6 = \int_{BC}^{TC} dx TPBN \quad \text{A.15}$$

$$I_7 = \int_{TC}^{BU} dx TNBN \quad \text{A.16}$$

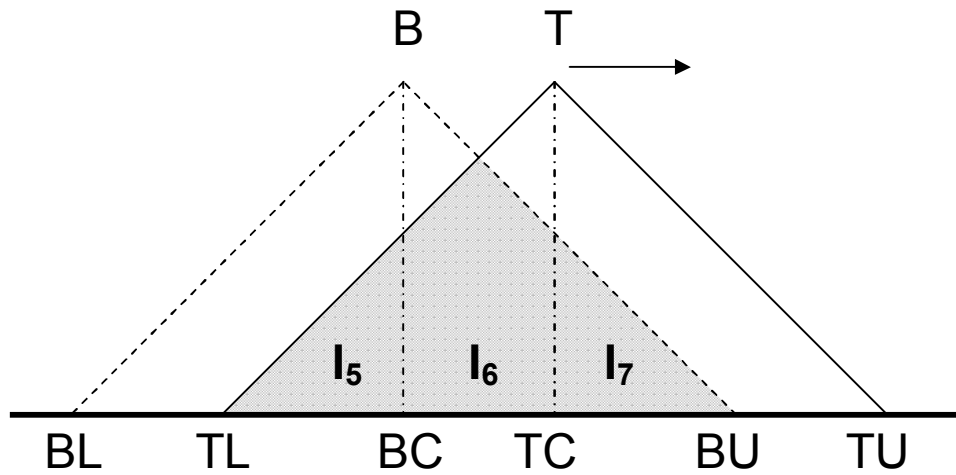


Figure A.3 Region 3 of the convolution over testing and basis functions.

**d. Region 4:  $TC \leq BU$**

In this region the shaded area in Figure 4,  $I_8$ , as:

$$I_8 = \int_{TL}^{BU} dx TPBN \quad \text{A.17}$$

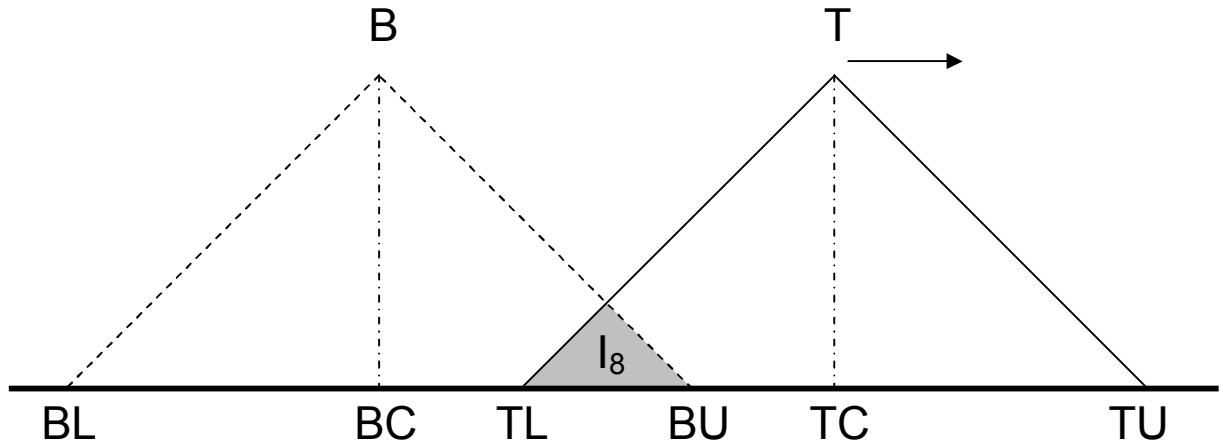


Figure A.4 Region 4 of the convolution over testing and basis functions.

In these all 4 regions, there are 4 kinds of integrals with changing boundaries. These 4 kinds of integrals can be written down for parametric boundaries as below:

$$\int_{x_1}^{x_2} dxTNBP = \frac{1}{(wh_x)^2} \left\{ -\frac{x_2^3 - x_1^3}{3} + [(m+n)h_x + u] \frac{x_2^2 - x_1^2}{2} \right. \\ \left. + [(1+m)h_x + u](1-n)h_x(x_2 - x_1) \right\} \quad \text{A.18}$$

$$\int_{x_1}^{x_2} dxTPBP = \frac{1}{(wh_x)^2} \left\{ \frac{x_2^3 - x_1^3}{3} + [(2-m-n)h_x - u] \frac{x_2^2 - x_1^2}{2} \right. \\ \left. + [(1-m)h_x - u](1-n)h_x(x_2 - x_1) \right\} \quad \text{A.19}$$

$$\int_{x_1}^{x_2} dxTNBN = \frac{1}{(wh_x)^2} \left\{ \frac{x_2^3 - x_1^3}{3} - [(2+m+n)h_x + u] \frac{x_2^2 - x_1^2}{2} \right. \\ \left. + [(1+m)h_x + u](1+n)h_x(x_2 - x_1) \right\} \quad \text{A.20}$$

$$\int_{x_1}^{x_2} dx TPBN = \frac{1}{(wh_x)^2} \left\{ -\frac{x_2^3 - x_1^3}{3} + [(m+n)h_x + u] \frac{x_2^2 - x_1^2}{2} + [(1-m)h_x - u](1+n)h_x(x_2 - x_1) \right\} \quad \text{A.21}$$

ii. **Convolution of derivative of the basis function with derivative of the testing function**

$$\left\langle \frac{d}{dx} J_{mx}, G_q * \frac{d}{dx} J_{nx} \right\rangle = \iint dudv G_q(u, v) \iint dx dy \frac{d}{dx} J_{mx}(x-u, y-v) \frac{d}{dx} J_{nx}(x, y) \quad \text{A.22}$$

a. **Region 1:  $BL \leq TU \leq BC$**

In this region, the shaded area in Figure 5,  $I_1$ , is calculated as:

$$I_1 = \int_{BL}^{TU} dx TNBP \quad \text{A.23}$$

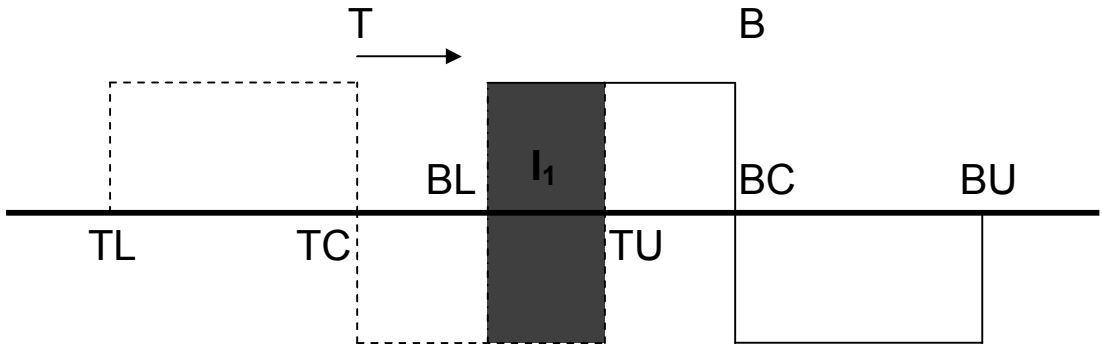


Figure A.5 Region 1 of the convolution over derivative of testing and basis functions.

b. **Region 2:  $BC \leq TU \leq BU$**

In this region, the shaded area in Figure 6,  $I$  is calculated as the sum of,  $I_2$ ,  $I_3$  and  $I_4$ .

$$I = I_2 + I_3 + I_4 \quad \text{A.24}$$

$$I_2 = \int_{BL}^{TC} dx TPBP \quad \text{A.25}$$

$$I_3 = \int_{TC}^{BC} dx TNBP \quad \text{A.26}$$

$$I_4 = \int_{BC}^{TU} dx TNBN \quad \text{A.27}$$

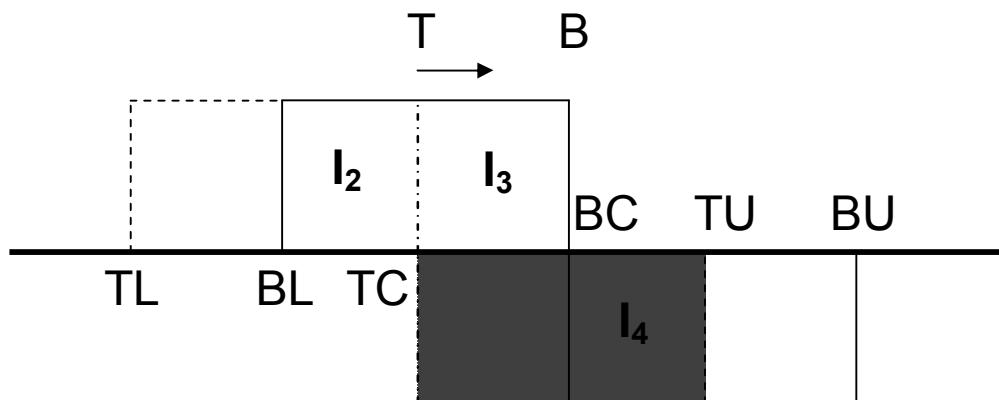


Figure A.6 Region 2 of the convolution over derivative of testing and basis functions.

**c. Region 3:  $BC \leq TC \leq BU$**

In this region, the shaded area in Figure 7,  $I$  is calculated as the sum of,  $I_5$ ,  $I_6$  and  $I_7$ .

$$I = I_5 + I_6 + I_7 \quad \text{A.28}$$

$$I_5 = \int_{TL}^{BC} dxTPBP \quad \text{A.29}$$

$$I_6 = \int_{BC}^{TC} dxTPBN \quad \text{A.30}$$

$$I_7 = \int_{TC}^{BU} dxTNBN \quad \text{A.31}$$

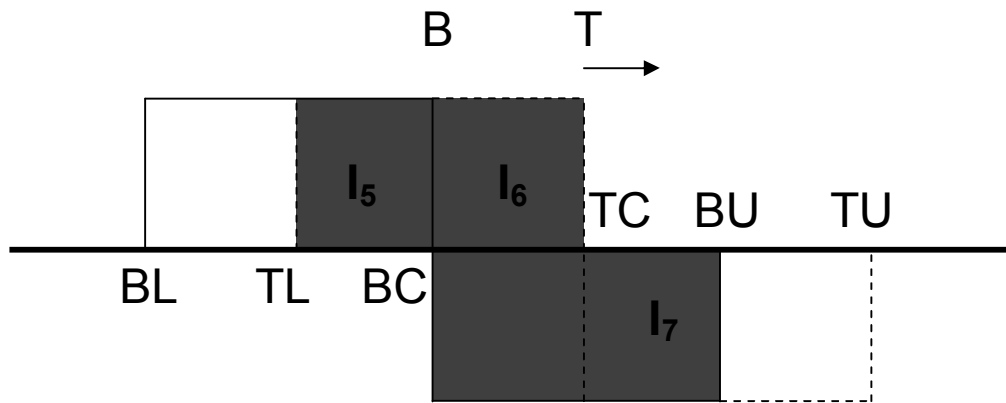


Figure A.7 Region 3 of the convolution over derivative of testing and basis functions.

**d. Region 4:  $TC \leq BU$**

In this region, the shaded area in Figure 8,  $I_8$ , is calculated as:

$$I_8 = \int_{TL}^{BU} dxTPBN \quad \text{A.32}$$

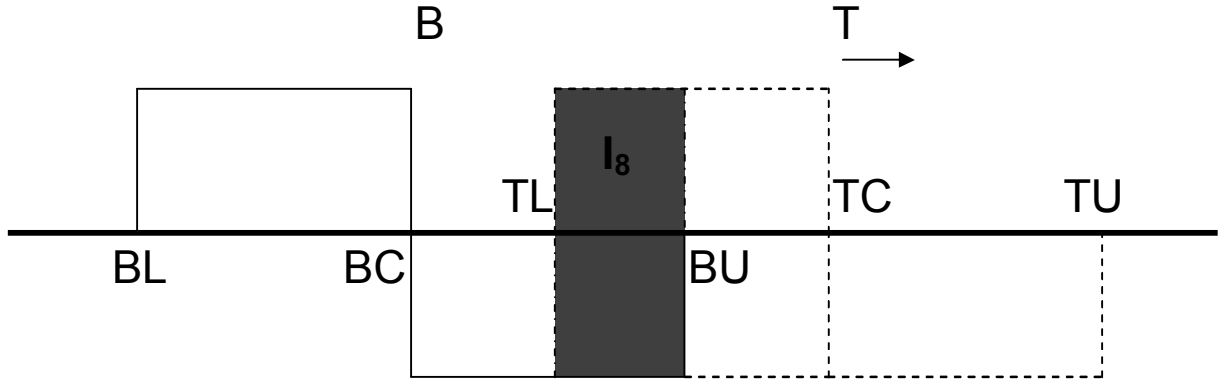


Figure A.8 Region 4 of the convolution over derivative of testing and basis functions.

In these all 4 regions, there are 4 kinds of integrals with changing boundaries. These 4 kinds of integrals can be written down for parametric boundaries as below:

$$\int_{x_1}^{x_2} dx TNBP = -\frac{1}{(wh_x)^2} (x_2 - x_1) \quad \text{A.33}$$

$$\int_{x_1}^{x_2} dx TPBP = \frac{1}{(wh_x)^2} (x_2 - x_1) \quad \text{A.34}$$

$$\int_{x_1}^{x_2} dx TNBN = \frac{1}{(wh_x)^2} (x_2 - x_1) \quad \text{A.35}$$

$$\int_{x_1}^{x_2} dx TPBN = -\frac{1}{(wh_x)^2} (x_2 - x_1) \quad \text{A.36}$$

iii. Convolution of basis function with source function

$$\langle J_{mx}, G_{xx}^A * J_s \rangle = \iint dudv G_{xx}^A(u, v) \iint dx dy J_{mx}(x-u, y-v) J_s(x, y) \quad \text{A.37}$$

**a. Region 1:  $SL \leq TU \leq SC$**

In this region, the shaded area in Figure 9,  $I_1$ , is calculated as:

$$I_1 = \int_{SL}^{TU} dx TNSL \quad \text{A.38}$$

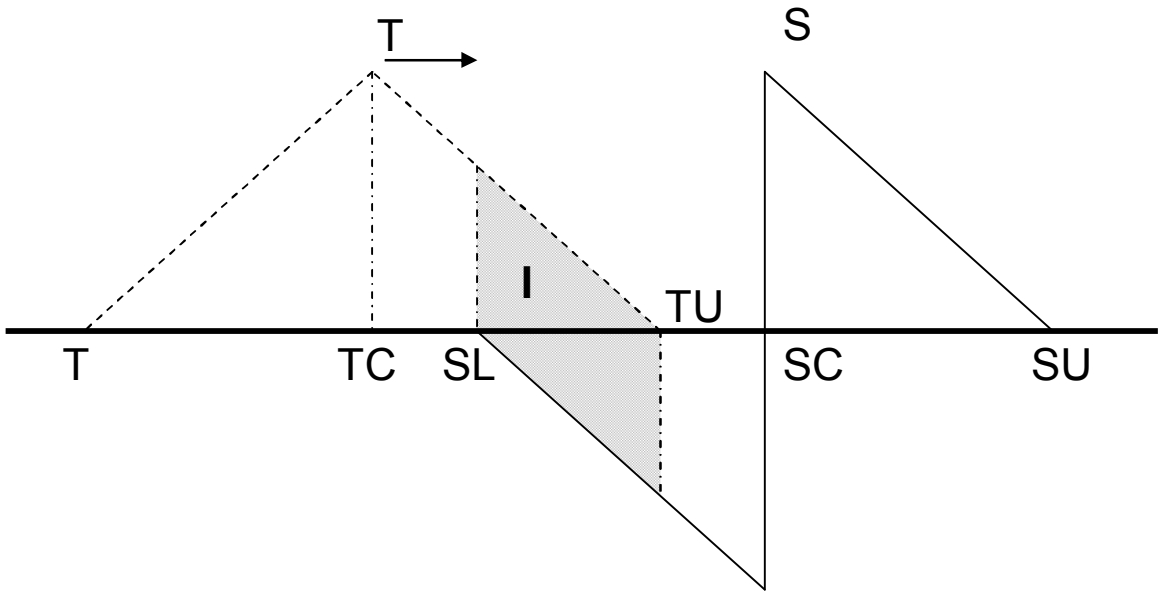


Figure A.5 Region 1 of the convolution over derivative of testing and basis functions.

**b. Region 2:  $SC \leq TU \leq SU$**

In this region, the shaded area in Figure 10,  $I$  is calculated as the sum of,  $I_2$ ,  $I_3$  and  $I_4$ .

$$I = I_2 + I_3 + I_4 \quad \text{A.39}$$

$$I_2 = \int_{SL}^{TC} dx TPSL \quad \text{A.40}$$

$$I_3 = \int_{TC}^{SC} dx TNSL \quad \text{A.41}$$

$$I_4 = \int_{SC}^{TU} dx TNSR \quad \text{A.42}$$

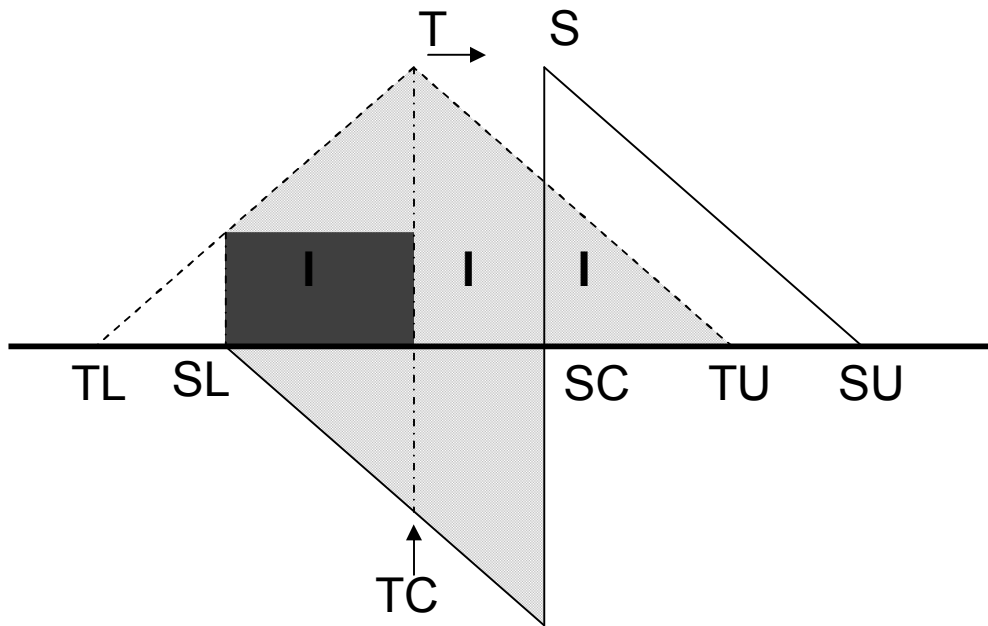


Figure A.6 Region 2 of the convolution over derivative of testing and basis functions.

**c. Region 3:  $SC \leq TC \leq SU$**

In this region, the shaded area in Figure 7,  $I$  is calculated as the sum of,  $I_5$ ,  $I_6$  and  $I_7$ .

$$I = I_5 + I_6 + I_7 \quad \text{A.43}$$

$$I_5 = \int_{TL}^{SC} dx TPSL \quad \text{A.44}$$

$$I_6 = \int_{SC}^{TC} dxTPSR \quad \text{A.45}$$

$$I_7 = \int_{TC}^{SU} dxTNSR \quad \text{A.46}$$

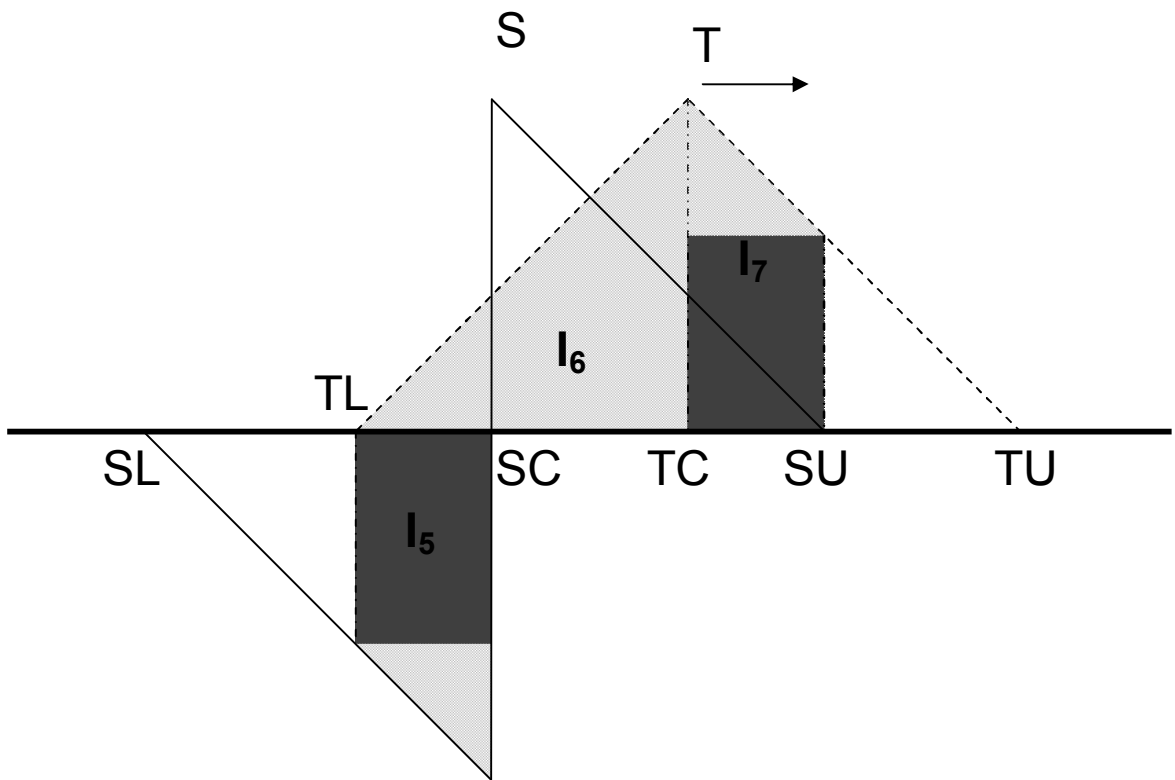
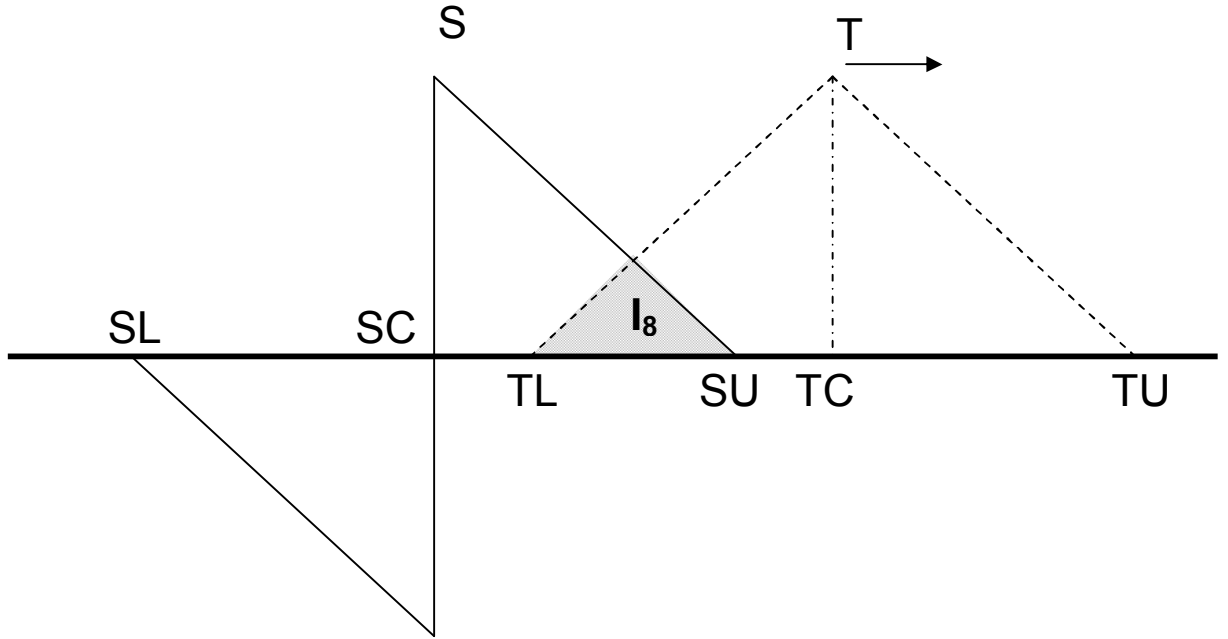


Figure A.6 Region 2 of the convolution over derivative of testing and basis functions.

**d. Region 4:  $TC \leq SU$**

In this region, the shaded area in Figure 8,  $I_8$ , is calculated as:

$$I_8 = \int_{TL}^{SU} dxTPSR \quad \text{A.47}$$



**Figure A.8 Region 4 of the convolution over derivative of testing and basis functions.**

In these all 4 regions, there are 4 kinds of integrals with changing boundaries. These 4 kinds of integrals can be written down for parametric boundaries as below:

$$\int_{x_1}^{x_2} dxTNSL = -\frac{1}{(wh_x)^2} \left\{ -\frac{x_2^3 - x_1^3}{3} + [mh_x + u] \frac{x_2^2 - x_1^2}{2} + [(1+m)h_x + u] h_x (x_2 - x_1) \right\} \quad \text{A.48}$$

$$\int_{x_1}^{x_2} dxTPSL = -\frac{1}{(wh_x)^2} \left\{ \frac{x_2^3 - x_1^3}{3} + [(2-m)h_x - u] \frac{x_2^2 - x_1^2}{2} + [(1-m)h_x - u] h_x (x_2 - x_1) \right\} \quad \text{A.49}$$

$$\int_{x_1}^{x_2} dxTNSR = \frac{1}{(wh_x)^2} \left\{ \frac{x_2^3 - x_1^3}{3} - [(2+m)h_x + u] \frac{x_2^2 - x_1^2}{2} + [(1+m)h_x + u] h_x (x_2 - x_1) \right\} \quad \text{A.50}$$

$$\int_{x_1}^{x_2} dxTPSR = \frac{1}{(wh_x)^2} \left\{ -\frac{x_2^3 - x_1^3}{3} + [mh_x + u] \frac{x_2^2 - x_1^2}{2} + [(1-m)h_x - u] h_x (x_2 - x_1) \right\} \quad \text{A.51}$$

iv. **Convolution of derivative of the basis function with derivative of the source function**

$$\left\langle \frac{d}{dx} J_{mx}, G_q * \frac{d}{dx} J_s \right\rangle = \iint du dv G_q(u, v) \iint dx dy \frac{d}{dx} J_{mx}(x-u, y-v) \frac{d}{dx} J_s(x, y) \quad \text{A.52}$$

a. **Region 1:  $SL \leq TU \leq SC$**

In this region, the shaded area in Figure 9,  $I_1$ , is calculated as:

$$I_1 = \int_{SL}^{TU} dxTNSL \quad \text{A.53}$$

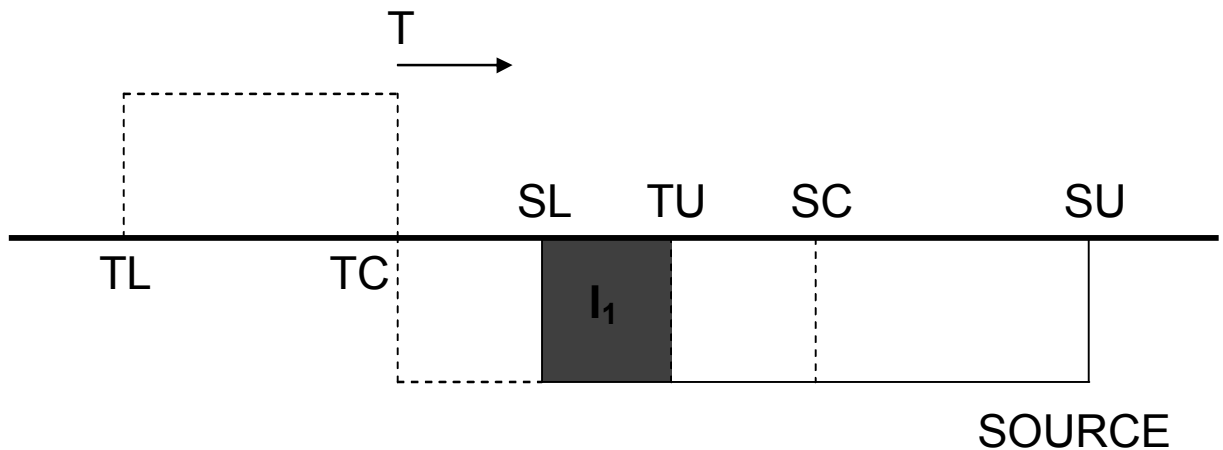


Figure A.5 Region 1 of the convolution over derivative of testing and basis functions.

b. **Region 2:  $SC \leq TU \leq SU$**

In this region, the shaded area in Figure 10,  $I$  is calculated as the sum of,  $I_2$ ,  $I_3$  and  $I_4$ .

$$I = I_2 + I_3 + I_4 \quad \text{A.54}$$

$$I_2 = \int_{SL}^{TC} dxTPSL \quad \text{A.55}$$

$$I_3 = \int_{TC}^{SC} dxTNSL \quad \text{A.56}$$

$$I_4 = \int_{SC}^{TU} dxTNSR \quad \text{A.57}$$

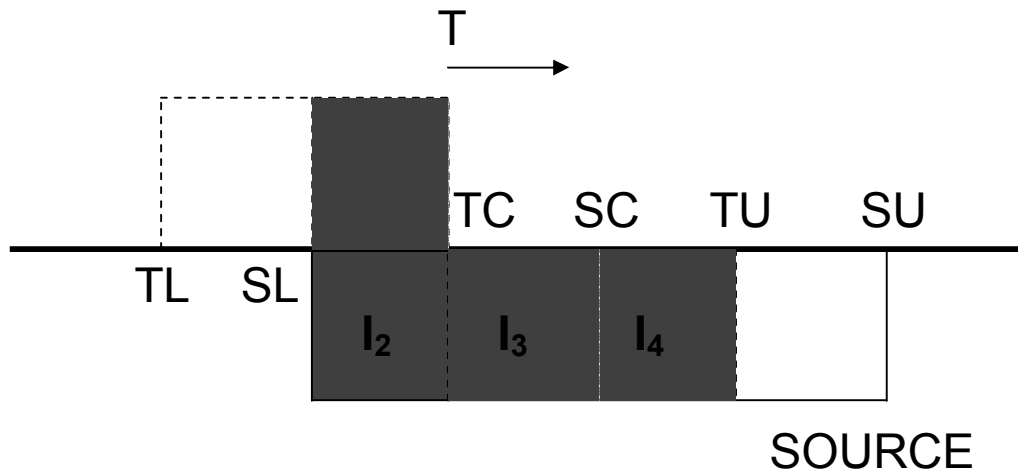


Figure A.14 Region 2 of the convolution over derivative of testing and derivative of source basis functions.

**c. Region 3:  $SC \leq TC \leq SU$**

In this region, the shaded area in Figure 7,  $I$  is calculated as the sum of,  $I_5$ ,  $I_6$  and  $I_7$ .

$$I = I_5 + I_6 + I_7 \quad \text{A.58}$$

$$I_5 = \int_{TL}^{SC} dxTPSL \quad \text{A.59}$$

$$I_6 = \int_{SC}^{TC} dxTPSR \quad \text{A.60}$$

$$I_7 = \int_{TC}^{SU} dxTNSR \quad \text{A.61}$$

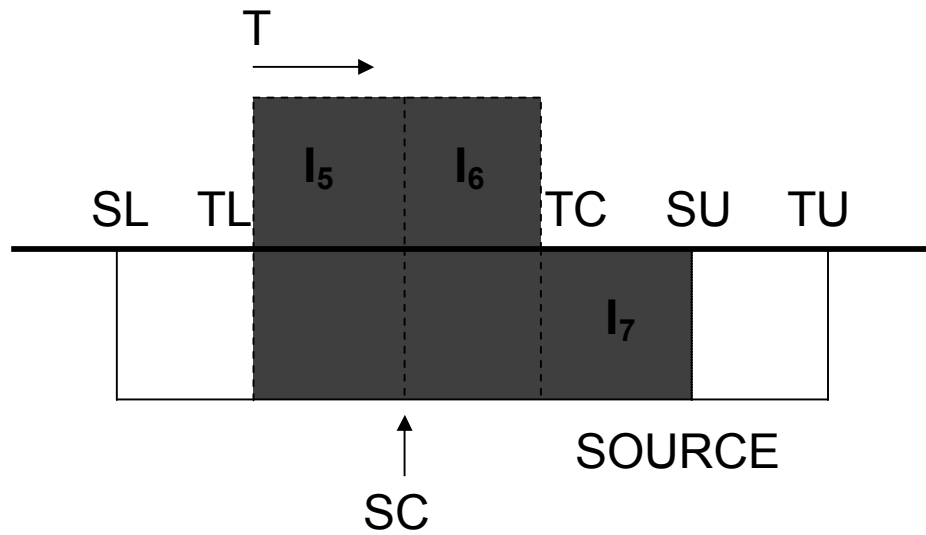
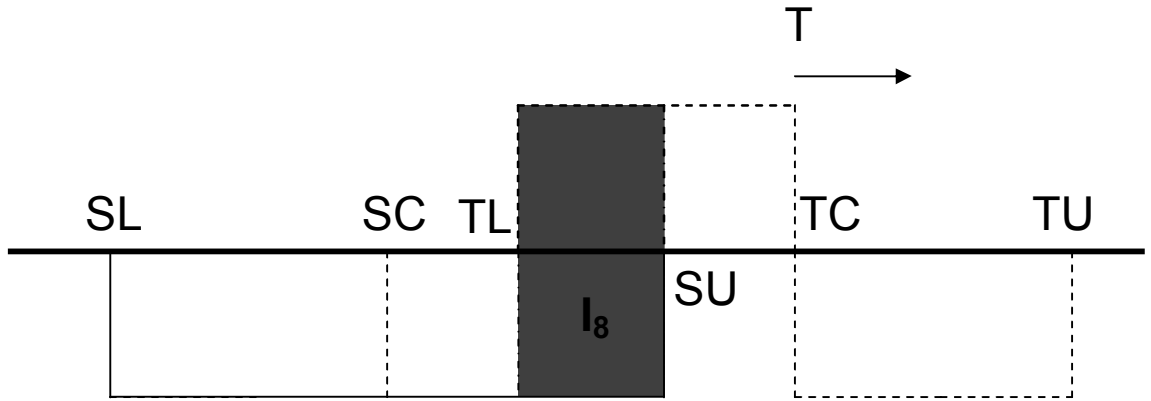


Figure A.14 Region 2 of the convolution over derivative of testing and derivative of source basis functions.

**d. Region 4:  $TC \leq SU$**

In this region, the shaded area in Figure 8,  $I_8$ , is calculated as:

$$I_8 = \int_{TL}^{SU} dxTPSR \quad \text{A.62}$$



## SOURCE

**Figure A.14 Region 2 of the convolution over derivative of testing and derivative of source basis functions.**

In these all 4 regions, there are 4 kinds of integrals with changing boundaries. These 4 kinds of integrals can be written down for parametric boundaries as below:

$$\int_{x_1}^{x_2} dxTNSL = \frac{1}{(wh_x)^2} (x_2 - x_1) \quad \text{A.63}$$

$$\int_{x_1}^{x_2} dxTPSL = -\frac{1}{(wh_x)^2} (x_2 - x_1) \quad \text{A.64}$$

$$\int_{x_1}^{x_2} dxTNSR = \frac{1}{(wh_x)^2} (x_2 - x_1) \quad \text{A.65}$$

$$\int_{x_1}^{x_2} dxTPSR = -\frac{1}{(wh_x)^2} (x_2 - x_1) \quad \text{A.66}$$

## APPENDIX B

### PRONY'S METHOD

Prony analysis has been shown to be a viable technique to model a linear sum of complex exponentials to signals that are uniformly sampled [42]. The Prony method was developed by Gaspard Riche, Baron de Prony in 1795 in order to explain the expansion of various gases [42]. In his original work, Prony suggested fitting a sum of exponentials to equally spaced data points and extended the model to interpolate at intermediate points. This method is not only used for a signal analysis but also for the system identification method, which is widely used in the areas of power system electromechanical oscillation, biomedical monitoring, radioactive decay, radar, sonar, geophysical sensing and speech processing. Different from oscillatory signal analysis techniques such as Fourier analysis, Prony analysis has the advantage of estimating damping coefficients apart from frequency, phase and amplitude. On the other hand, it best fits a reduced-order model to a high-order system both in time and frequency domains [42].

In this study, using the current distributions over the lines as sampled data, the reflected wave coefficients and incident wave coefficients can be found and the sampled data can be formulated as given below:

$$I(x) \cong c_1 e^{\beta_1 x} + c_2 e^{\beta_2 x} \quad \text{B.2}$$

Firstly, a p-exponent discrete function should be defined as:

$$I[x] \cong \sum_{k=1}^p c_k e^{\beta_k x} \quad \text{B.2}$$

Where  $c_k$  and  $\beta_k$  are the unknown complex parameters which will be found out after analysis. It is important to note that the sampled data is gathered from equally spaced points over the line as:

$$x = \frac{\text{length of line}}{N+1} n \quad \text{where } 0 \leq n \leq N+1 \text{ (N: number of basis)} \quad \text{B.3}$$

and

$$z_k = e^{\beta_k \frac{\text{length of line}}{N+1}} \quad \text{B.4}$$

By substituting (B.3) and (B.4) into (B.2), below equation is obtained:

$$I[n] \cong \sum_{k=1}^p c_k z_k^n \quad \text{B.5}$$

Matrix equivalent of (B.5) is depicted in (B.6).

$$\begin{bmatrix} z_1^0 & z_2^0 & \cdot & \cdot & z_{p-1}^0 & z_p^0 \\ z_1^1 & z_2^1 & \cdot & \cdot & z_{p-1}^1 & z_p^1 \\ \cdot & \cdot & \cdot & \cdot & \cdot & \cdot \\ z_1^{N+1} & z_2^{N+1} & \cdot & \cdot & z_{p-1}^{N+1} & z_p^{N+1} \end{bmatrix} \begin{bmatrix} c_1 \\ c_2 \\ \cdot \\ c_p \end{bmatrix} = \begin{bmatrix} I[0] \\ I[1] \\ \cdot \\ I[N] \\ I[N+1] \end{bmatrix} \quad \text{B.6}$$

Hence (B.5) can be approached as the solution of some homogeneous linear constant coefficient difference equation. Polynomial  $\phi(z)$  can be defined in order to find form of this difference equation.

$$\phi(z) = \prod_{k=1}^p (z - z_k) \quad \text{B.7}$$

Where,  $z_k$ 's are the roots of the polynomial. Same polynomial can also be defined below:

$$\phi(z) = \sum_{m=0}^p a[m]z^{p-m} \quad \text{B.8}$$

Where  $\mathbf{a[m]}$  's are complex coefficients to be found and  $\mathbf{a[0]=1}$ . In order to find these coefficients, (p+1) equations are multiplied by  $a[p]$ ,  $a[p-1]$ , ...,  $a[1]$  and 1 respectively. Then results are added. This process should be repeated (N+1-p) times and the following (N-p+2) equations are obtained.

$$\begin{bmatrix} I[0] & I[1] & \dots & I[p-2] & I[p-1] \\ I[1] & I[2] & \dots & I[p-1] & I[p] \\ \vdots & \vdots & \ddots & \vdots & \vdots \\ I[N+1-p] & I[N+2-p] & \dots & I[N-1] & I[N] \end{bmatrix} \begin{bmatrix} a[p] \\ a[p-1] \\ \vdots \\ a[1] \end{bmatrix} = \begin{bmatrix} -I[p] \\ -I[p+1] \\ \vdots \\ -I[N] \\ -I[N+1] \end{bmatrix} \quad \mathbf{B.9}$$

In general  $N > 2p$ , hence, using the pseudo-inverse of the  $I$  matrix,  $\mathbf{a}[\mathbf{m}]$ 's are found. Then the roots of (B.8) can be gathered by substituting  $\mathbf{a}[\mathbf{m}]$ 's in that equation. If  $z_k$ 's are known,  $\beta_k$  's can be obtained as described in (B.4). Using the equation (B.6),  $c_k$  's can also be found.

## APPENDIX C

### SINGULARITY EXTRACTION

As  $r \rightarrow 0$ , due to the direct term of the Green's functions shown in (C.1), a singularity occurs.

$$G \cong \sum_{n=1}^N a_n \frac{e^{-jkr_n}}{r_n} \quad \text{C.1}$$

In order to remove the singularity, first double integration in (4-20) is performed by extracting the direct term from the total equation. Then, the direct term is expanded using Taylor series expansion.  $e^{-jkr}$  about  $r=0$  can be expressed as in (C.2):

$$e^{-jkr} = 1 + (-jkr) + \frac{(-jkr)^2}{2!} + \frac{(-jkr)^3}{3!} \quad \text{C.2}$$

By dividing (C.2) to  $r$ , a direct term can be obtained in the right hand side of (C.3)

$$\frac{e^{-jkr}}{r} = \frac{1}{r} + (-jk) + r \frac{(-jk)^2}{2!} + r^2 \frac{(-jk)^3}{3!} \quad \text{C.3}$$

Then, the right hand side of (C.3) can be added to the double integration except from first term. When the source and observation points are at  $z=0$ , first term of the right hand side of (C.3) can be represented as in (C.4) in two dimensions.

$$\frac{1}{r} = \frac{1}{\sqrt{x^2 + y^2}} \quad \text{C.4}$$

Then, this representation is used in the double integration as [27]:

$$\int_{y_1}^{y_2} \int_{x_1}^{x_2} \frac{1}{\sqrt{x^2 + y^2}} dx dy = y_2 \log \left[ \frac{-x_1 + \sqrt{x_1^2 + y_2^2}}{-x_2 + \sqrt{x_2^2 + y_2^2}} \right] + y_1 \log \left[ \frac{-x_2 + \sqrt{x_2^2 + y_1^2}}{-x_1 + \sqrt{x_1^2 + y_1^2}} \right] \\ + x_2 \log \left[ \frac{-y_1 + \sqrt{x_2^2 + y_1^2}}{-y_2 + \sqrt{x_2^2 + y_2^2}} \right] + x_1 \log \left[ \frac{-y_2 + \sqrt{x_1^2 + y_2^2}}{-y_1 + \sqrt{x_1^2 + y_1^2}} \right] \quad \text{C.5}$$

(C.5) completes the singularity extraction problem, and it can be used in double integration in order to include the direct term.